NAZARBAYEV UNIVERSITY

AGGREGATION INDUCED EMISSION ORGANIC CATION INCORPORATED QUASI-2D PEROVSKITES FOR PHOTONIC AND OPTOELECTRONIC APPLICATION

by

Almaz Beisenbayev

Submitted in partial fulfillment of the requirement of Nazarbayev University
for the degree of
Doctor of Philosophy in Chemical Engineering

School of Engineering and Digital Sciences
Nazarbayev University

Supervised by
Dr. Chang-Keun Lim
Dr. Askhat Jumabekov
Dr. Jong H. Kim

February 2025

Declaration

I declare that the research contained in this thesis, unless otherwise formally indicated within the text, is the author's original work. The thesis has not been previously submitted to this or any other university for a degree and does not incorporate any material already submitted for a degree.

Almaz Beisenbayev

Date: April 9, 2026

ABSTRACT

Two-dimensional perovskites make up a remarkable candidate material for optoelectronic applications owing to their tunability, powerful excitonic interactions, stability and solution processability. However, conventional organic spacer cations have limitations such as weak optical absorption, insulating character, and a lack of electronic interaction with the inorganic framework, which restrict efficient energy transfer and charge transport across the organic–inorganic interface. This thesis addresses this challenge by designing, synthesis and incorporating of aggregation-induced enhanced emission (AIEE) organic cations into layered perovskite systems and investigating their impact on band alignment, energy transfer, and photophysical behavior.

Two AIEE cations, BPCSA and FPCSA, with distinct electronic properties, were used to fabricate n = 1 and n = 2 quasi-2D perovskites with iodide- and bromide-based compositions. Their electronic interactions with the inorganic framework were analyzed using ultraviolet photoelectron spectroscopy, absorption and photoluminescence spectroscopy measurements. FPCSA, due to its fluorinated structure, exhibits deeper energy levels compared to BPCSA. It shows reduced coupling in iodide systems, while type-I alignment is restored in bromide-based perovskites due to their deeper valence band and wider bandgap. Increasing the perovskite thickness from n = 1 to n = 2 reduces quantum confinement and introduces mixed-phase distributions, leading to energy funneling and more complex exciton dynamics. In these systems, AIEE cations act not only as structural components but also as active participants in exciton recombination processes.

Overall, this work demonstrates that the optoelectronic properties of quasi-2D perovskites can be effectively tuned through combined AIE molecular engineering and halide composition control. These findings provide valuable insights into interfacial energetics and offer design guidelines for advanced optoelectronic materials.

ACKNOWLEDGMENTS

First and foremost, I would like to express my sincere gratitude to my supervisor, Prof. Chang-Keun Lim, for his continuous support—both financial and emotional—along with his kindness and encouragement throughout my entire PhD journey.

I am also deeply grateful to my co-supervisor, Prof. Askhat Jumabekov, for introducing me to the interesting world of research at Nazarbayev University.

I would like to extend my heartfelt thanks to my colleagues from PMBP, as well as members of Prof. Jumabekov's and Prof. Annie Ng's research groups, who became more than just colleagues to me.

Last but not least, I am especially thankful to my wife for her patience and unwavering support, and to my daughter—without whom I would have graduated two years earlier.

TABLE OF CONTENT

LIST OF TABLES

LIST OF FIGURES

LIST OF ABBREVIATIONS

2D	Two-dimensional
3D	Three-dimensional
LP	Luminophore
PL	Photoluminescence
AIEE	Aggregation-induced enhanced emission
HOMO	Highest occupied molecular orbital
LUMO	Lowest unoccupied molecular orbital
NIR	Near infrared
PSC	Perovskite solar cell
LED	Light emitting diode
PD	Photodetector
QWS	Quantum well structure
MHP	Metal halide perovskite
PVSK	Perovskite
EL	Electroluminescence
EQE	External quantum efficiency
PCE	Power conversion efficiency
VBM	Valence band maximum
CBM	Conduction band minimum
PLQY	Photoluminescence quantum yield
RP	Ruddlesden-Popper
DJ	Dion-Jacobson
DOS	Density of states
COCiP	Conjugated organic cation incorporated perovskite
ISC	Inter system crossing
UPS	Ultraviolet photoelectron spectroscopy
XRD	X-ray diffraction
UV	Ultraviolet

CHAPTER 1: INTRODUCTION

1.1. Motivation

Perovskite (PVSK) materials were first discovered in the 1800s, but only in recent decades has the halide PVSK family attracted substantial research interest, initially as transistor materials and subsequently as light absorbers. Currently, these materials are recognized as leading semiconductors for next-generation photovoltaic technologies. Despite this promise, environmental stability issues—including sensitivity to heat, light, electrical bias, and moisture—continue to impede the advancement of PVSK-based devices. Reducing the dimensionality of PVSKs by isolating inorganic sheets, chains, or individual octahedra with organic molecules has been proposed as a strategy to enhance environmental stability. Among low-dimensional PVSKs, two-dimensional (2D) PVSKs have attracted particular attention because they retain many essential characteristics of three-dimensional (3D) PVSKs, while offering tunable optoelectronic properties, chemical diversity, facile integration into heterostructures, and improved stability.

The potential applications of 2D PVSKs extend beyond photovoltaics to include light emission, lasing media, and photodetection. The absorption and emission wavelengths, defined by the energy gap (E_g) between the valence and conduction bands, of 3D PVSKs can be tuned through substitution of halide anions, metal cations, and organic or inorganic cations. In the case of quasi-2D PVSKs (2D PVSK films with bulky organic cations, such as long chain alkylammonium), smaller 2D layers generate a corresponding increment in Eg. This compositional and structural diversity allows full-color photoluminescence in the visible and near-infrared phases. Long aliphatic and small aromatic organic cations, which include butylammonium, octylammonium, dodecylammonium, phenylethylammonium, among others, are often included in quasi-2D PVSKs for the insulation to immobilize photogenerated excitons in the two-dimensional dimension (2D PVSK) quantum well. In addition, organic cations containing π-conjugated luminophores such as naphthalene, oligothiophene, carbazole, pyrene and polydiacetylene have been used in the investigation of enhanced optical and electrical properties of PVSKs. Since their absorption coefficient per mass is high and organic luminophores (LPs) can be used for sensitisation, improving the optical and optoelectronic characteristics of PVSKs is suggested. Nevertheless, their tendency to dampen photoluminescence by Dexter or Förster energy transfer between homologous

molecules creates a major obstacle to achieving effective sensitization of 2D PVSKs. This study is intended to deal with the main challenges in 3D and 2D PVSKs.

1.2. Problem statement

2D PVSKs have a quantum-well structure consisting of organic barriers and inorganic wells. The substantial HOMO–LUMO gap resulting from the insulating properties of non-conjugated short-chain organic ligands occurs in this approach. The incorporation of organic ligands with extended conjugation can lead to tuning of the 2D quantum-well structure, such as from type I to type II or reversed-type I band alignment within the organic–inorganic hybrid system. Because of their higher absorption coefficient per unit mass, organic ligands have great potential as sensitizers for improving the optical and optoelectronic properties of PVSKs. However, the photoluminescence (PL) quenching mechanism caused by regressive Dexter and/or Förster energy transfer between homologous species complicates the implementation for successful sensitization in 2D PVSKs.

1.3. Goals of the study

Building on the information mentioned above, our objectives are to:

1. Design and synthesize aggregation-induced emission (AIE) dyes.
2. Fabricate aggregation-induced emission organic cation-incorporated 2D PVSKs.
3. Conduct a detailed study of the structural and optical properties of the synthesized hybrid material.

Achieving these goals will allow us to establish a scientific foundation for programmable hybrid organic-inorganic PVSKs, enabling advanced manipulation and transformation of light. To accomplish this, we developed an AIE cation-incorporated two-dimensional PVSK crystalline hybrid system that exhibits versatile optical and optoelectronic properties across various energy level alignments of the two semiconductors.

1.4. Hypothesis

Electronic coupling between PVSK layers and the organic p-electron system is hypothesized to produce hybridized states, resulting in a rich density of states that may enhance absorption.

Aggregation-induced emission (AIE) ligands represent a new class of luminophores with superior photoluminescence properties, especially at higher ligand concentrations. Their resistance to concentration quenching, a limitation of conventional luminophores, enables an extended exciton lifetime in the AIE organic cation layer, thereby facilitating energy and charge transfer between the organic and PVSK layers.

1.5. Scientific significance and novelty

In the novel AIE-PVSK hybrid system, excitonic effects can result from interactions between the organic and inorganic layers, which act as coupled superlattices. The band alignment between these layers determines the nature of the coupled system formed upon photoexcitation: Type I, where electrons and holes are confined within either the organic or inorganic layers, and Type II, where holes are localized in the inorganic layer and electrons in the organic layer, or vice versa.

The organic layer aligns with Type I and forms a Frenkel-type exciton band that can promote Förster or Dexter energy transfer, and the inorganic layer generates Wannier excitons. In Type II alignment, in which the valence and conduction bands of the inorganic layer are offset relative to the highest occupied molecular orbital (HOMO) and lowest unoccupied molecular orbital (LUMO) levels, holes pass between the valence band and HOMO level, and electrons transfer between the LUMO level and conduction band. This produces charge-transfer excitons. As a result, in this hybrid system, the energy and charge transfer can be orchestrated by varying energy level alignment. Energy transfer is increased under Type I alignment; therefore, the PL of 2D PVSK layers in quasi-2D PVSKs will increase. The latter step was triggered by the better light absorption of pi-conjugated organic materials and the longer life of Frenkel excitons in AIE materials. This photosensitization is expected to enhance the linear and nonlinear PL properties of PVSK, making it efficient as a light source and energy upconverter. In Type II alignment, such charge transfer is facilitated, causing photo-induced charge separation. This generation produces an emission band which is narrower than the bandgap of either the organic or two-dimensional PVSK layers. The resulting charge transfer emission enables the PL wavelength to be tuned to the near-infrared (NIR) range, which is beyond the capability of the existing PVSKs. This feature is of great usefulness for near-IR spectroscopy in mobile sensing approaches. Moreover, the

separated charges in a Type II alignment can improve charge extraction at the interface between the PVSK layer and the carrier transport layer in optoelectronic devices, including solar cells.

1.6. How this thesis is organized

This thesis investigates the role of aggregation-induced emission (AIE) active organic cations in controlling the electronic structure, interfacial interactions, and photophysical properties of low-dimensional and quasi-two-dimensional (quasi-2D) perovskites. By integrating molecular design with perovskite dimensionality and halide composition, this work aims to establish fundamental relationships between organic spacer chemistry, band alignment, and exciton dynamics in hybrid perovskite systems.

Chapter 1 introduces the background and motivation for this study, highlighting the advantages of two-dimensional perovskites for optoelectronic applications and the limitations of conventional organic spacer cations. The concept of aggregation-induced emission is presented as a promising strategy to overcome photoluminescence quenching and enhance the optoelectronic functionality of hybrid systems. The research objectives and hypotheses are also outlined.

Chapter 2 provides a comprehensive literature review on hybrid perovskites, with a focus on low-dimensional structures, excitonic behavior, and energy transfer mechanisms. The role of organic cations in tuning structural and electronic properties is discussed, along with recent advances in AIE materials and their potential integration into perovskite systems.

Chapter 3 describes the experimental methods used in this work, including material synthesis, thin film fabrication, and characterization techniques. Structural, optical, and electronic characterization methods such as X-ray diffraction (XRD), ultraviolet–visible (UV–vis) spectroscopy, photoluminescence (PL), time-resolved PL, and ultraviolet photoelectron spectroscopy (UPS) are detailed.

Chapter 4 focuses on the design, synthesis, and photophysical characterization of AIE-active organic cations, specifically BPCSA and FPCSA. Their molecular structures, optical absorption, emission properties, and electronic energy levels are analyzed to establish their suitability as functional spacer cations in hybrid perovskites.

Chapter 5 presents the integration of AIE cations into n = 1 and n = 2 perovskite systems and examines their structural, electronic, and optical properties. The effects of AIE incorporation on band alignment, energy transfer, and exciton recombination pathways are discussed in detail.

Particular attention is given to the influence of molecular design and halide composition on interfacial coupling and emission behavior, including the emergence of free exciton (FE) and self-trapped exciton (STE) emission.

Finally, Chapter 6 summarizes the key findings of this work and discusses their implications for the design of advanced hybrid perovskite materials.

CHAPTER 2: LITERATURE REVIEW

2.1 Metal Halide PVSK

Metal halide perovskites (MHPs) have developed into an important materials system in optoelectronics in the past decade. The technologies based on MHPs (perovskite solar cells (PSCs) [1-3], light-emitting diodes (LEDs) [4-6], photodetectors (PDs) [7-9], lasers [10-12]) have rapidly advanced the field, due to their remarkable properties. The general formula ABX3 of the MHP family (A = CH_3NH^{3+} (MA), $HC(NH_2)^{2+}$ (FA), Cs^+; B = Pb^{2+}, Sn^{2+}; X = I^-, Cl^-, Br^-), however possesses the advantage of easy and cheap processing, and adjustable optical and electronic properties. Such properties provide the robust basis for the generation of high-performance, multifunctional optoelectronic devices and promote their industrial use [13,14].

The optoelectronic behaviour of MHPs has received attention from the 1950s onwards, following the occurrence of $CsPbX_3$ (X = Cl, Br) crystals containing a perovskite structure that display a frequency-dependent type of photoconductive response, exemplifying their unique electrical behaviors [15]. In the early 1990s, Mitzi et al. investigated layered tin halide perovskites that do self-assemble into quantum well structures (QWS) with a cation of alkylammonium [16]. These materials demonstrated notable excitonic features that put them towards their potential roles as LEDs and transistors (due to a wide range of tunable electronic properties). Light emission and lasing was first reported in $(C_6H_{13}NH_3)_2PbI_4$ in 1998 [17]. The very first perovskite-sensitized solar cell with a power conversion efficiency (PCE) of 3.8% was developed in 2009, accounting for a major step forward [1]. We saw early advances in PCE after this milestone, which surpassed 20% within a decade. All this was followed by the sharp attention paid to the intrinsic optoelectronic properties of MHPs, which are tunable band gaps, long carrier diffusion lengths, strong light absorption, low defect density, and the ability to proceed with solutions [1, 18,19].By the mid-2010s, MHPs demonstrated significant potential as optical sources, exhibiting high optical gain and stable amplified spontaneous emission (ASE) with a threshold of 10 ± 2 μJ cm^{-2} at room temperature [10]. The first laser in this field, operating without an external cavity, as well as the first optically pumped perovskite microcavity laser, were reported. In 2015, $CsPbX_3$ MHP nanocrystals exhibited ASE and lasing with low pump thresholds of 5 ± 2 μJ cm^{-2} [20]. Concurrently, the first room-temperature perovskite LEDs (with an external quantum efficiency

of approximately 0.76%) were reported, and Heiss and colleagues developed the first $MAPbI_3$ photodetectors (PDs) with X-ray sensitivity of 25 μC mGy_{air}^{-1} cm^{-3} [21,22]. In 2017, Park's team achieved highly sensitive X-ray PDs (up to 11 μC mGy_{air}^{-1} cm^{-2}) based on printable $MAPbI_3$ films [23]. The late 2010s witnessed renewed interest in layered perovskites and perovskite nanocrystals (NCs), which demonstrated PL and electroluminescence (EL) efficiencies comparable to those of bulk perovskites. This resurgence prompted extensive studies on the effects of dimensionality, size, geometry, composition, and colloidal synthesis methods on their optoelectronic properties. Green, red, and near-infrared LEDs achieved external quantum efficiencies (EQE) of up to 20.3%, 21.3%, and 21.6%, respectively, while $CsPbBr_3$ NCs enabled breakthroughs in X-ray detectors with a low dose rate of 13 nGy s^{-1} [8, 23-27].

During the 2020s, new and outstanding optoelectronic properties of MHPs are still achieved. Certified power conversion efficiencies (PCEs) of single-junction PSCs, all-perovskite tandem solar cells, and hybrid tandem PSCs have reached 25.7%, 28%, and 31.3%, respectively [28-30]. The application scope of these materials has expanded beyond PSCs, LEDs, and PDs, supporting the integration of diverse optoelectronic devices. Meanwhile, the problem of material instability is being progressively resolved. Novel optoelectronic characteristics of MHPs are creating new research opportunities and speeding up the progress of the field. Currently, the special properties of MHPs are being described in more detail, promoting their multidisciplinary applications and advancing their practical implementation in technology.

2.2 Origin of optoelectronic properties of metal halide PVSKs

In a typical ABX_3 perovskite, the B-site cation is located at the center of an octahedral $[BX_6]^{4-}$ cluster, resulting in a framework composed of corner-sharing BX_6 octahedra. The A-site cation is coordinated to twelve X anions in a cuboctahedral geometry and occupies the interstitial sites within the BX_6 octahedral framework, as shown in Figure 2.1. For the $[PbI_6]^{4-}$ octahedron, the valence band maximum (VBM) arises from the antibonding interactions between Pb(6s) and I(5p) atomic orbitals, whereas the conduction band minimum (CBM) is derived from antibonding Pb(6p) and I(5s) orbitals. These intrinsic electronic configurations of metal halide perovskites (MHPs) are responsible for their outstanding optoelectronic properties, including high optical absorption, elevated carrier mobility, significant defect tolerance, long carrier diffusion lengths, ambipolar charge transport, and tunability [31-36].

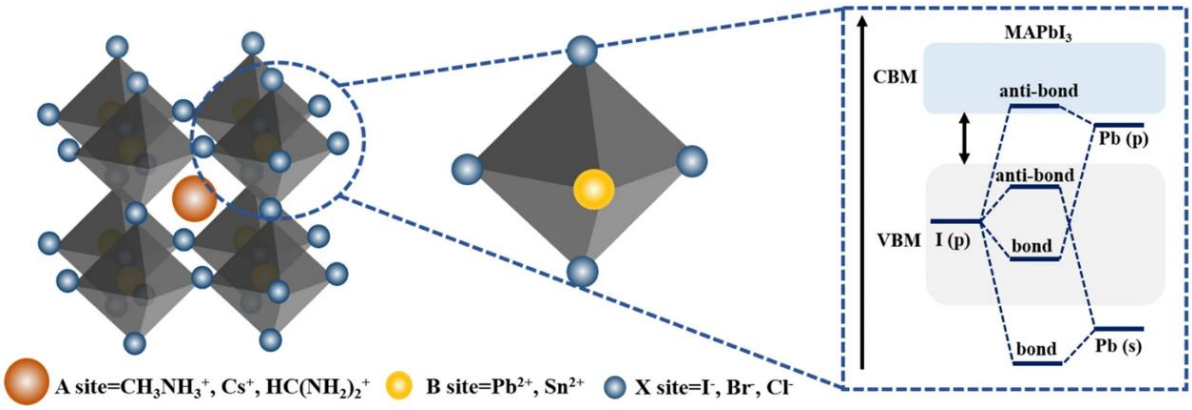

Figure 2.1. A schematic illustration of MHPs crystal structure on the left and the molecular orbitals for $MAPbI_3$ on the right. Reprinted from [31]

(i) High optical absorption: The high symmetry of the MAPbI3 crystal structure results in a direct band gap. The lone pair electrons on the Pb s-orbital facilitate p-p electronic transitions from the valence band (VB) to the conduction band (CB), leading to exceptionally high optical absorption [31].

(ii) Highly mobile carriers: the inorganic Pb-I structure mainly affects the valence and conduction band-edge states. As well, the antibonding of the VB and CB of MHPs gives rise to the relatively small effective electron mass. It has a property providing high charge carrier mobility [32].

(iii) High defect tolerance: expanding the orbitals expands VB bandwidth and raises VB edge and most defect state lies inside or close to VB edge. Additionally, such a weak coupling of Pb 6p & I 5p imparts an ionic characteristic to the CB edge, whereby there is a negligible external defect effect on energy states. These characteristics are responsible for the large defect tolerance of MHPs [33].

(iv) Long diffusion lengths: the high carrier mobility and defect tolerance of MHPs leads to long diffusion lengths. In best PVSK crystals an ideal one is characterized with a carrier diffusion length longer than 10 μm [34].

(v) Ambipolar charge transport: Electron and hole effective masses of $0.23m_0$ and $0.29m_0$, respectively allow MHPs to have ambipolar charge transport. This characteristic is crucial for photovoltaic applications [35].

(vi) Flexible tunability: the band structure of MHPs is controlled by the B and X elements, allowing to tune the valence band maximum (VBM), conduction band minimum (CBM), and band gap through elemental substitution.

The doubly bridging halide ion (B-X-B moiety), likewise, is capable of undergoing successive phase transitions where the double-substituted halide halides can be stimulated in response to changes in temperature, pressure, or the chemical environment leading to variations of the B-X-B angle from the crystal optimum [36]. The unique features of MHPs is due to the unique crystal structure and chemical composition which makes it so that individual and coordinated modulations were very fine-tuned to the optoelectronic properties. This flexibility is a basis of importance for their utilization in the various optoelectronic devices. Current tunable optoelectronic properties of MHPs are presented in the next section.

2.3 Tunability optoelectronic properties of metal halide PVSKs

2.3.1 Phase transition

The flexibility of the BX_6 framework in ABX_3 MHPs is primarily attributed to the large metal-halide-metal (B-X-B) bond angle, which enables PVSKs to undergo successive phase transitions. These transitions substantially influence the electronic structure and, consequently, the

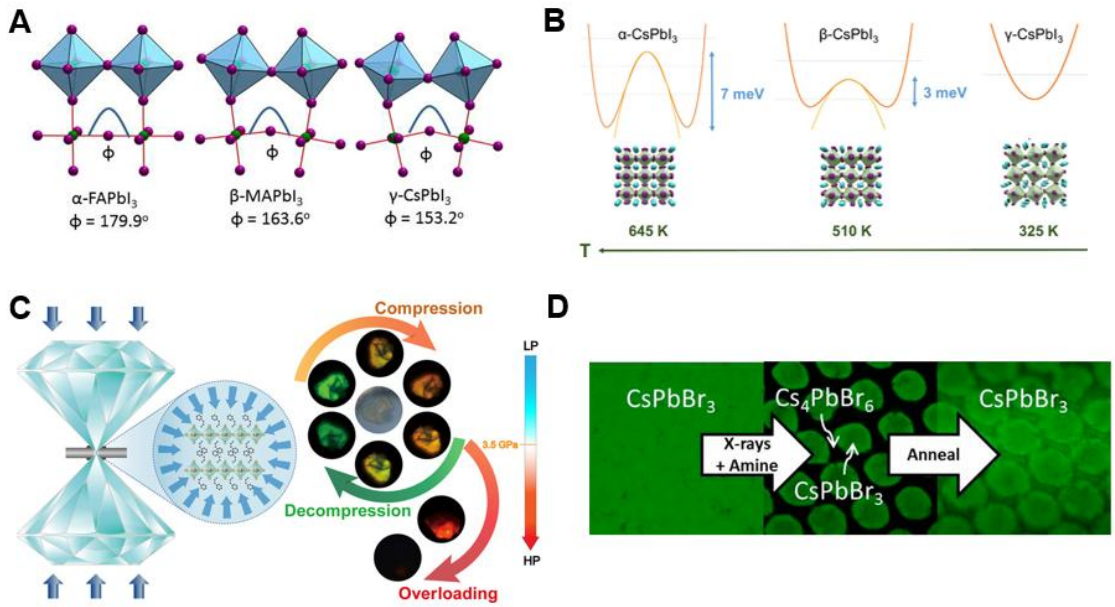

Figure 2.2. (A) B-X-B angle of the $APbI_3$ series with various cations at room temperature [33]. (B) Temperature-induced phase transition in $CsPbI_3$ crystal [39]. (C) Pressure-induced phase transition in $(C_4H_9NH_3)_2PbI_4$ single crystal [40]. (D) Chemistry-induced phase transition in $CsPbBr_3$ crystal [41].

optoelectronic properties of MHPs [37]. For example, in the prototypical $APbI_3$ material, variations in the cation series (MA^+, FA^+, and Cs^+) result in progressively greater octahedral tilting in the PVSK phase at room temperature (Φ change in Fig. 2.2), driven by decreasing cation size [38]. This increased tilting leads to a corresponding rise in the band gap, from 1.48 eV in α-$FAPbI_3$ to 1.67 eV in γ-$CsPbI_3$. PVSK phase transitions are typically controlled by temperature, pressure, or chemical composition. For instance, the structural phase transition in cesium halide PVSKs is temperature-dependent and often occurs between a non-PVSK phase at room temperature and a high-temperature PVSK phase (Fig. 2.2B).

The phases show individual optoelectronic characteristics in terms of bandgap, photoluminescence quantum efficiency, charge-carrier mobility, and carrier lifetime. High-pressure phase transitions can also be generated; it has been reported that PVSKs can modulate optical bandgap and enhance photoluminescence under several gigapascals of pressure. Remarkably, the 2D structure of PVSK crystal materials can in some cases be maintained in a metastable and alternate phase at ambient pressure after multiple cycle compression and decompression, and in some cases amorphized above 10 GPa in the 2D PVSK crystal matrix (Fig. 2.2C), leading to strong excitonic emissions within the photoluminescence spectra [39]. Additionally, at room temperature, chemical reactions that employ acid-base interactions can facilitate reversible structural and compositional transformations of CsPbX3 nanocrystals, and thus facilitate the transition between cubic and orthorhombic phases (Fig. 2.2D) [40]. Such behavior is attributed to controlled self-assembly of small CsPbX3 nanocrystals by manipulating the ligand shell environment [41]. Taken together, the findings further represent the feasibility of doped halide PVSKs in implementable switchable optoelectronic systems, for instance, smart windows or building-integrated photovoltaics.

2.3.2 Composition

As ionic materials, MHPs family provide flexibility in the chemistry through substitution at A, B and X sites. This allows optimization of optics parameters for example band gap,

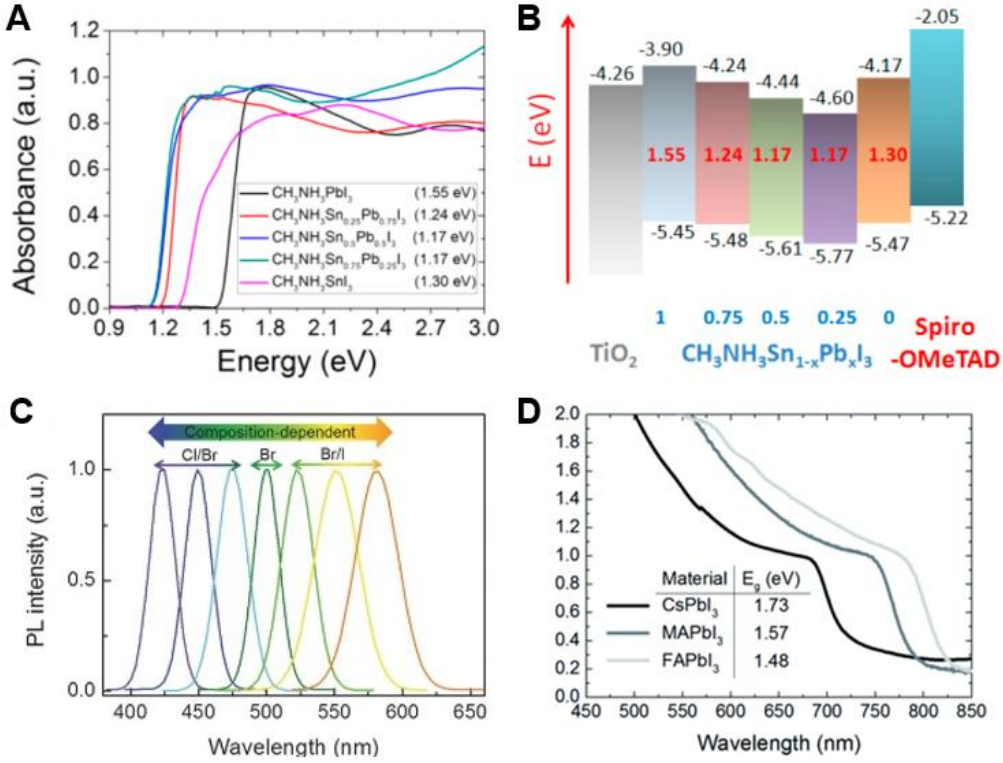

Figure 2.3 Absorption spectra and schematic energy level diagrams of $CH_3NH_3Sn_{1-x}Pb_xI_3$ solid solution perovskites (PVSKs): (A) Electronic absorption spectra and (B) schematic energy level diagram of $CH_3NH_3Sn_{1-x}Pb_xI_3$ solid solution PVSKs [42]. (C) Photoluminescence (PL) spectra of PVSK $CsPbX_3$ quantum dots with composition tunability achieved by varying halide content. (D) UV–visible spectra of $APbI_3$ PVSKs, where A represents cesium (Cs), methylammonium, or formamidinium [43].

photoluminescence diversity and carrier transport. ABI_3 is tuned in the same way with modulated band gap when the B-site cation is substituted with Sn, and the A-site cation is replaced with Cs or FA (Fig. 2.3A, B, D) [42, 43]. These compositional modifications provide an overall framework for designing MHPs with targeted band gaps and energy level positions. What is also of particular note is that the highly soluble precursor materials in MHPs readily form the basis for rapid anion exchange, which typically takes just a few seconds and does not modify the original structure or introduce any major lattice defects or surface defects.

This anion doping strategy is often employed to tune the chemical composition and optical properties of the more stable $CsPbX_3$ nanostructures. All of these advantages of compositional flexibility have made MHPs fit for applications in various fields, such as light-emitting diodes,

wavelength-tunable lasers, and photodetectors, which can act over wide spectral excursions. As shown in Fig. 2.3C, the PL emission of CsPbX3 quantum dots can be tuned from the ultraviolet to the near-infrared spectral regions using anion-based spectral tuning method. This yields quantum dot light-emitting diodes (QLEDs) with uniform and large-area blue, green and orange light emission.

2.3.3 Geometry

Choosing such a crystal geometry ensures a very fine tuning of the optoelectronic properties of MHPs. This leads to special microcavity effects with respect to MHP lasers through different crystal geometry. The optical cavity also plays a major role in producing optical feedback necessary for the oscillation of the laser, configuring the limiting lasing mode in the gain spectrum and defining the spatial properties of the output beam. MHP lasers typically use two types of optical microcavities: intrinsic and extrinsic.

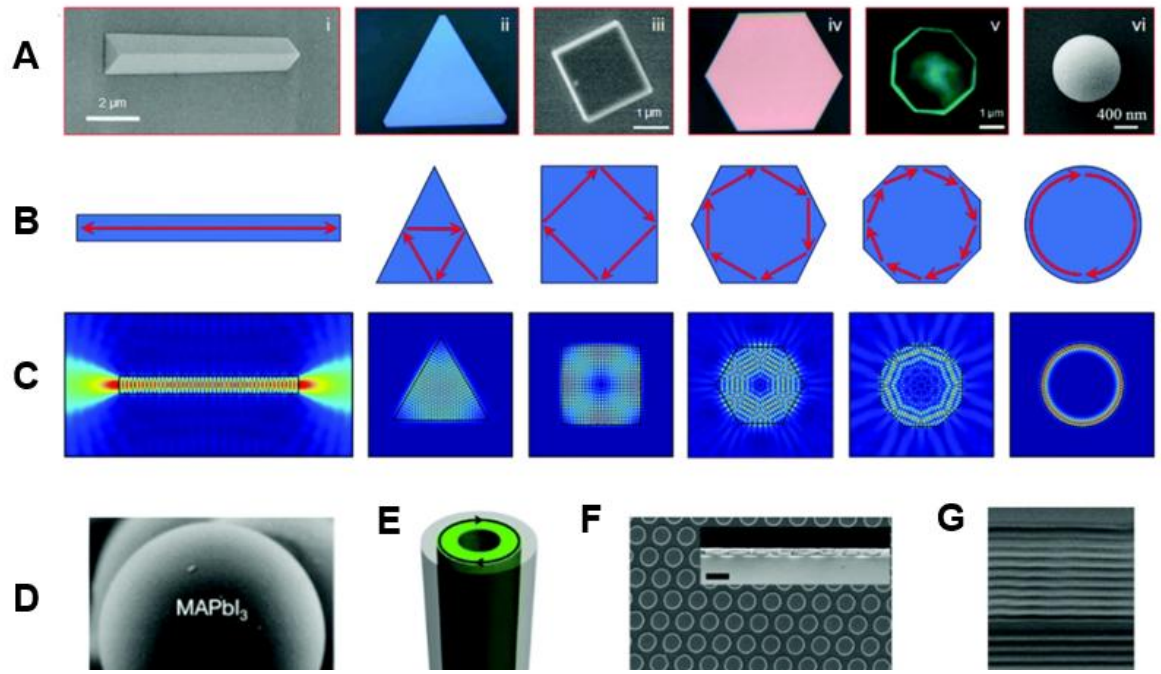

Figure 2.4 (A–C) Intrinsic cavities of metal halide perovskites (MHPs). (A) PVSK crystals exhibit a range of morphologies, including one-dimensional nanowires, two-dimensional triangular, tetragonal, hexagonal, and octagonal microdisks, as well as three-dimensional microspheres. (B) Optical trajectories for PVSK cavities with different geometries. (C) Simulated field distributions corresponding to PVSK cavities with various morphologies [44]. (D–G) Extrinsic cavities of MHPs. (D) Side-view SEM image of a microsphere cavity [45]. (E) Schematic representation of a capillary cavity supporting circular whispering gallery mode laser resonances [46]. (F) SEM image of a distributed feedback laser fabricated on a quartz substrate [47]. (G) Cross-sectional SEM image of a PVSK distributed Bragg reflector laser device [48].

The intrinsic cavity of MHP has a specific geometric structure for optical feedback in the MHP material. As shown in Figure 2.4A, which covers several groups—one-dimensional (1D) nanowires, two-dimensional (2D) triangular, tetragonal, hexagonal, and octagonal microdisks, and three-dimensional (3D) microspheres—that could be synthesized based on different methods, indicating the geometry-dependent microcavity effects. For instance, $MAPbBr_3$ 1D microwires with a rectangular cross-section exhibit Fabry-Pérot longitudinal cavity effects, whereas 2D microplates demonstrate four-edge reflected whispering-gallery-mode lasing action. In contrast, extrinsic cavities are formed by introducing additional structures that provide optical feedback to MHPs, such as microsphere and capillary cavities, distributed feedback (DFB) cavities, and distributed Bragg reflector cavities, as depicted in Figure 2.4. Integration of MHPs into these extrinsic cavities can be achieved using techniques such as spin coating, inkjet printing, and vacuum thermal evaporation. These advantages of MHPs enable the fabrication of miniaturized lasers with specific functionalities, promoting the development of hybrid flexible optical elements and advancing miniaturized photonic circuits with enhanced performance.

2.3.4 Dimensionality

Due to the diverse structures and compositions of MHPs, particularly with the choice of R cation, the dimensionality of MHPs can be precisely adjusted, ranging from 3D to lower-dimensional forms, including quasi-two-dimensional (quasi-2D), two-dimensional (2D), one-dimensional (1D), and zero-dimensional (0D) structures (Fig. 2.5A). Typically, "low-dimensional" MHPs are categorized into two types: "structure-level" and "material-level." The "structure-level" low dimension refers to the morphology of MHPs, including nanostructures like nanosheets, nanowires, and nanocrystals. In contrast, "material-level" low dimension focuses on the intrinsic crystal structure, where the $[BX_6]^{4-}$ octahedra are separated by bulky dielectric spacer molecules, forming bulk assemblies of atom-level 0D clusters, 1D quantum wires, or 2D quantum wells (QWs).

Compared to 3D MHPs, low-dimensional variants exhibit distinct band structures, as the dimensionality and size of the nanostructures directly influence the electronic band gap and joint density of states (DOS) near the band gap, which are key factors in determining their optoelectronic properties. Generally, lower-dimensional MHPs have narrower absorption ranges due to their larger bandgaps, which vary with the number of layers [49]. In a family of low-dimensional MHPs with the same metal halide octahedral framework, the lowest energy electronic transition follows a trend: E_g, 3D < Eg, 2D < Eg, 1D < HOMO-LUMO, 0D. Notably, the inclusion of dielectric and quantum confinement effects in low-dimensional MHPs can further increase the differences in optoelectronic properties between 3D and low-dimensional structures. The exciton binding energy decreases progressively as n increases, and when n ≤ 2, the PVSKs display strong excitonic behavior with high photoluminescence quantum yield (PLQY) at room temperature [50]. This enhanced oscillator strength and optical nonlinearity in low-dimensional MHPs make them ideal

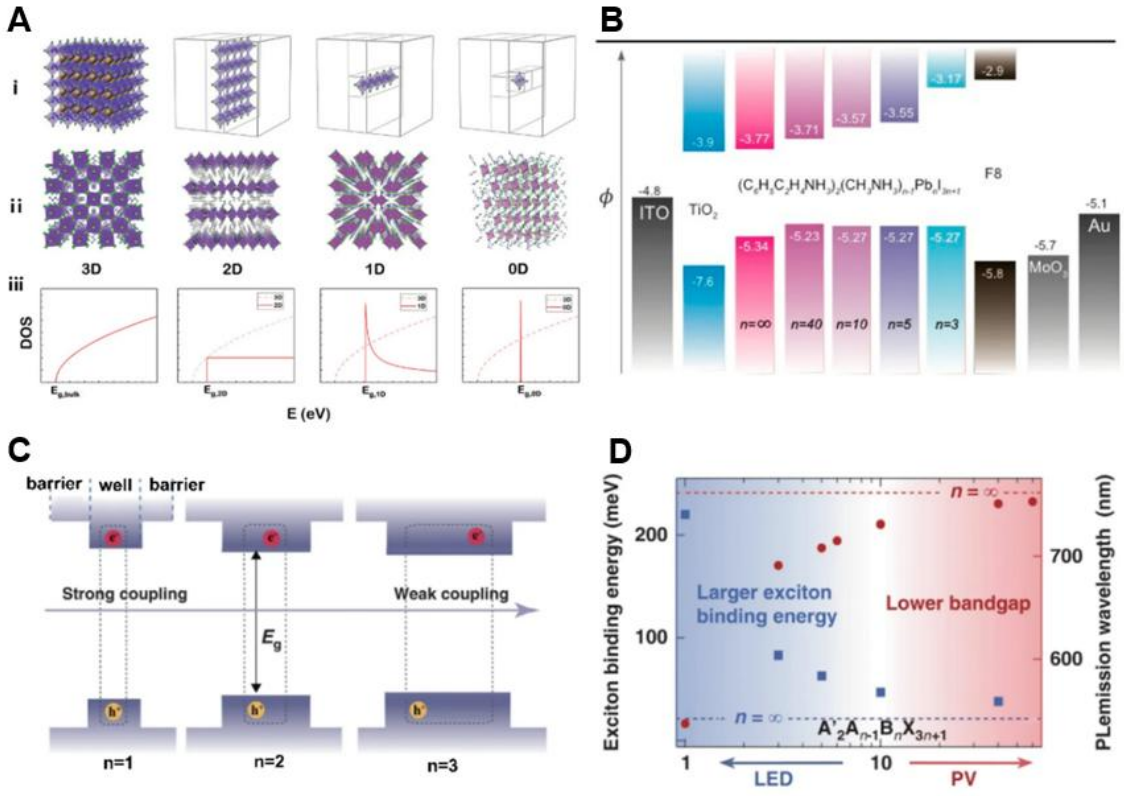

Figure 2.5 (A) Schematic depiction of (i) "structure-level" and (ii) "material-level" 3D bulk, 2D, 1D, and 0D PVSK materials, with (iii) the corresponding density of states plotted against the energy Eg [50]. (B) Electronic band structure of low-dimensional metal halide PVSKs (MHPs) with varying n values [51]. (C) Illustration of the quantum and dielectric confinement effects in low-dimensional MHPs [52]. (D) Exciton binding energy and photoluminescence (PL) emission wavelength as a function of the number of n layers in low-dimensional MHPs [53, 54].

for light-emitting applications. However, when $n \geq 3$, the PVSKs exhibit lower exciton binding energy and smaller bandgaps, extending the light absorption range into the visible spectrum, which makes them more suitable for sunlight-to-energy conversion.

2.4 2D and Quasi-2D metal halide PVSKs

2D and quasi-2D PVSKs demonstrate unique optical characteristics when contrasted with 3D and traditional 2D PVSKs. For example, quasi-2D PVSKs are composed of various phases (indicated by n) and naturally incorporate quantum well states (QWS), which contribute to dielectric effects and quantum confinement phenomena [54-57]. Upon exposure to light, photogenerated carriers transition from the lower-n phase to the higher-n phase within quasi-2D PVSKs, leading to light emission through radiative recombination at the 3D PVSK level (where $n = \infty$). Furthermore, the PL spectrum of quasi-2D PVSKs can be tailored across the ultraviolet (UV) to near-infrared (NIR) spectrum by modifying their composition and dimensional attributes. Due to their remarkable optical properties and robust resistance to moisture, heat, and light degradation, quasi-2D PVSKs have garnered considerable interest for applications in optoelectronic devices such as LEDs, solar cells, and photodetectors. This section offers a comprehensive examination of the essential features of quasi-2D PVSKs, encompassing their structural properties, dielectric and quantum confinement effects, photoluminescence quantum yields (PLQYs), and durability.

2.4.1 Synthesis strategy

In the fabrication of quasi-2D perovskite films, two primary techniques are frequently employed: spin coating and blade coating [55, 58–62]. Spin coating, illustrated in Figure 2.6A, involves applying a precursor solution onto a glass substrate and then spinning it to create a uniform thin film. This method incorporates a minimal amount of antisolvent to regulate the crystallization process effectively. Following this step, the film undergoes annealing on a heating plate. This technique is particularly advantageous for generating high-quality films over relatively small areas. The quality of the final film is significantly influenced by factors such as precursor concentration, environmental conditions, spin speed, and annealing temperature.

Conversely, Figure 2.6B depicts the blade coating method, which is typically utilized for producing large-area films. In this approach, a blade applies the precursor solution across the substrate within a glovebox filled with nitrogen to minimize exposure to moisture and oxygen. Subsequently, samples may be placed in a vacuum chamber to enhance solvent evaporation—

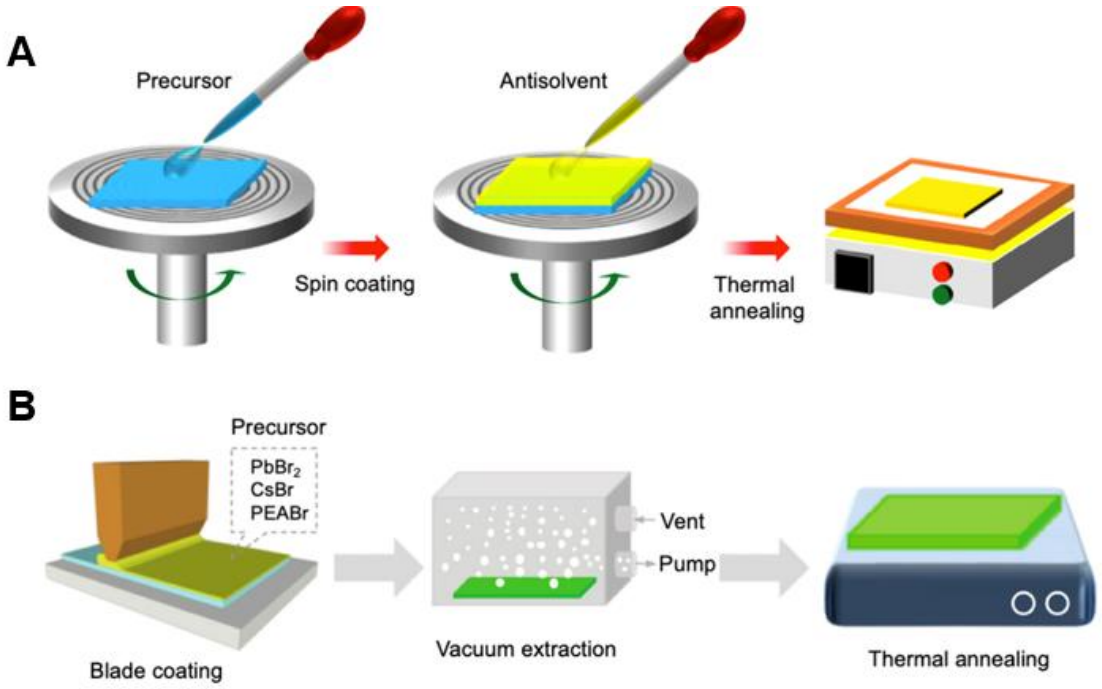

Figure 2.6. (A) Schematic diagram showing the syntheses of quasi-2D PVSK films by spin coating. (B) Schematic diagram showing the syntheses of quasi-2D PVSK films by blade coating. [63]

thereby preventing unwanted component migration or aggregation—though this step is not always necessary. The film then undergoes annealing to promote crystallization. Various factors affect the characteristics of films produced via blade coating, including precursor concentration, environmental conditions, coating speed, vacuum level (if applicable), and annealing parameters.

2.4.2 Structure properties

Perovskite solid materials can be categorized into 3D, 2D, and quasi-2D architectures based on their crystallographic arrangements, as illustrated in Figure 2.7. Traditional 3D perovskites typically consist of standard carbon-based perovskite frameworks represented by the formula ABX_3, where A denotes a small monovalent cation, B stands for a divalent metal cation, and X refers to a halide anion. In this structure, each B-site cation is surrounded by six halide ions forming a BX_6 octahedron, while the A-site cations occupy the voids within a three-dimensional network (see Figure 2.7C). These materials exhibit octahedral tilting that may lead to phase transitions between cubic ($Pm\bar{3}m$) and orthorhombic (Pbnm) forms near room temperature, potentially compromising structural stability [64,65].

In contrast, 2D perovskites are generally defined by the formula L_2BX_4, where L is a larger monovalent organic spacer cation. The inclusion of these extensive organic layers promotes quantum confinement along the thickness (refer to Figure 2.7A), resulting in significantly enhanced exciton-binding energies compared to those found in 3D devices. However, such materials may also experience heightened nonradiative recombination processes, leading to lower photoluminescence quantum yields (PLQYs) at ambient temperatures.

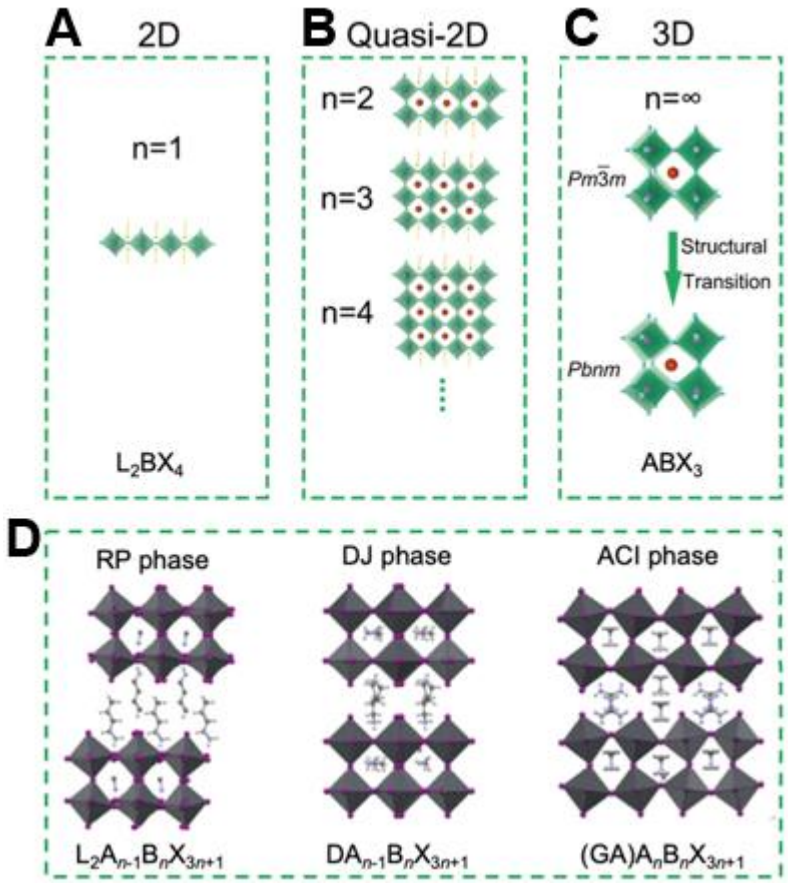

Figure 2.7. Schematic representation of perovskite structures with varying dimensionalities: (A) 2D, (B) quasi-2D, and (C) 3D. (D) Schematic diagrams of quasi-2D perovskites in the RP, DJ, and ACI phases, respectively. [66]

Quasi-2D PVSKs bridge the gap between the 2D and 3D systems by leveraging the high PLQYs and excellent charge transport properties of traditional 3D perovskites while benefiting from the improved stability and film-forming capabilities inherent in 2D structures. They feature a distinctive arrangement of linear finite slabs of 3D perovskite separated by bulky organic spacer cations; these organic layers act as insulating barriers for the inorganic frameworks comprised of corner-sharing $[BX_6]^{4-}$ octahedra.

The monovalent cations occupy the voids within the framework (Figure 2.7B). The unit cell sheets of quasi-2D PVSKs are periodic along the basal plane but are restricted in the perpendicular direction.

Quasi-2D PVSKs are further subdivided into three types according to the nature of the organic ligands: Ruddlesden–Popper (RP) phase, Dion–Jacobson (DJ) phase, and alternating cations in the interlayer space (ACI) phase, as depicted in Figure 2.7D. The RP phase PVSKs possess the general chemical formula $L_2A_{n-1}B_nX_{3n+1}$, where n indicates the number of inorganic $[BX_6]^{4-}$ octahedral units between two spacer layers. In the RP phase, adjacent octahedral layers are staggered with a shift of (1/2, 1/2) along the ab plane and are held together by van der Waals forces. The DJ phase PVSKs are described by the formula $DA_{n-1}B_nX_{3n+1}$, where D represents a divalent spacer cation. Unlike the RP phase, the octahedral layers in the DJ phase are perfectly aligned without relative shifts. The ACI phase PVSKs have the formula $(GA)A_nB_nX_{3n+1}$, where GA denotes a guanidinium spacer cation. In the ACI phase, the small A cation is present in both the inorganic framework and the interlayer, together with the GA cation. The octahedral layers in the ACI phase exhibit a staggered arrangement with a shift of (1/2, 0) along the ab plane.

2.4.3 Dielectric- and quantum confinement effect

As depicted in Figure 2.8, a quasi-2D PVSK features multiple quantum well (QW) structures, where the metal-halide octahedra ($[BX_6]^{4-}$) form the QW and the large organic spacer

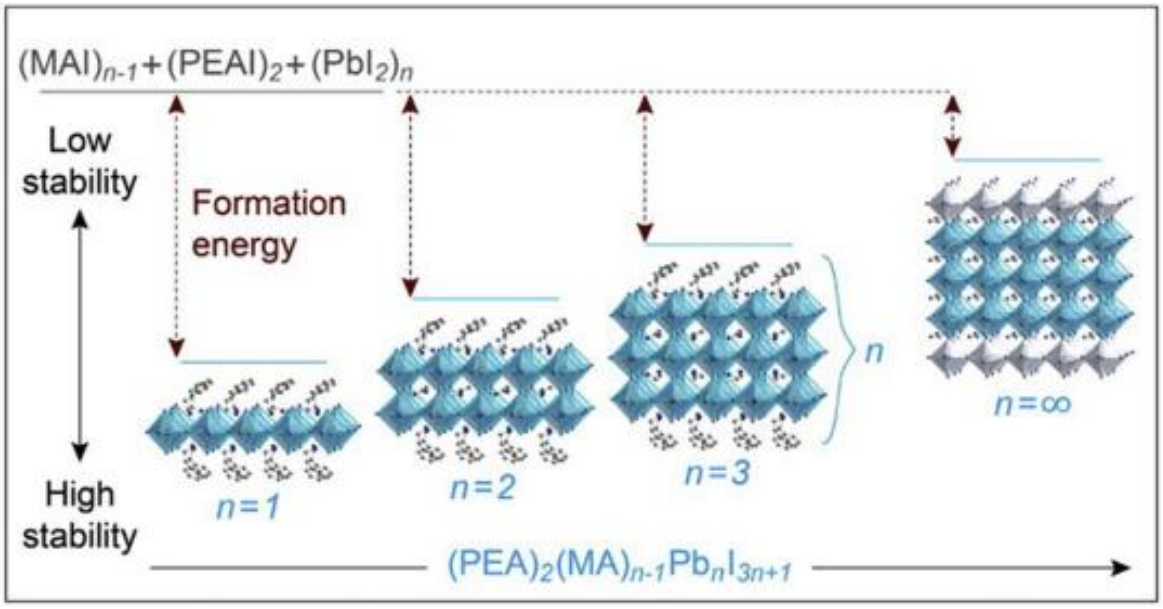

Figure 2.8. Schematic illustration of quasi-2D PVSKs with multiple QWs. [56]

cations act as quantum barriers. Quantum and dielectric confinement effects restrict excitons within the octahedral layers and compress the carrier wave function along one axis. The degree of confinement is determined by QW thickness, enabling precise tuning of the band gap (Eg), binding energy (Eb), and carrier properties .

Quasi-2D PVSKs consist of mixed phases with different n values, facilitating energy transfer between these phases. The energy funneling effect enables exciton energy to migrate from high-band-gap (low-n) phases to low-band-gap (high-n) phases, where excitons ultimately recombine [51, 55, 56, 64]. This process enhances radiative carrier recombination, resulting in high photoluminescence quantum yields (PLQYs) in quasi-2D PVSKs, even at low excitation densities. Efficient energy transfer depends on rapid migration of photogenerated carriers from low-n to high-n phases to avoid trapping, underscoring the importance of optimizing the energy-transfer pathway for the synthesis of high-quality quasi-2D PVSKs.

2.4.4 Photoluminescence quantum yield

PLQY is a critical parameter for assessing nonradiative recombination losses in quasi-2D PVSKs. It is commonly defined as the ratio of emitted photons to absorbed photons. Figure 2.9 illustrates the various recombination pathways for charge carriers in quasi-2D PVSKs, including trap-assisted recombination, excitonic recombination, bimolecular recombination, and Auger

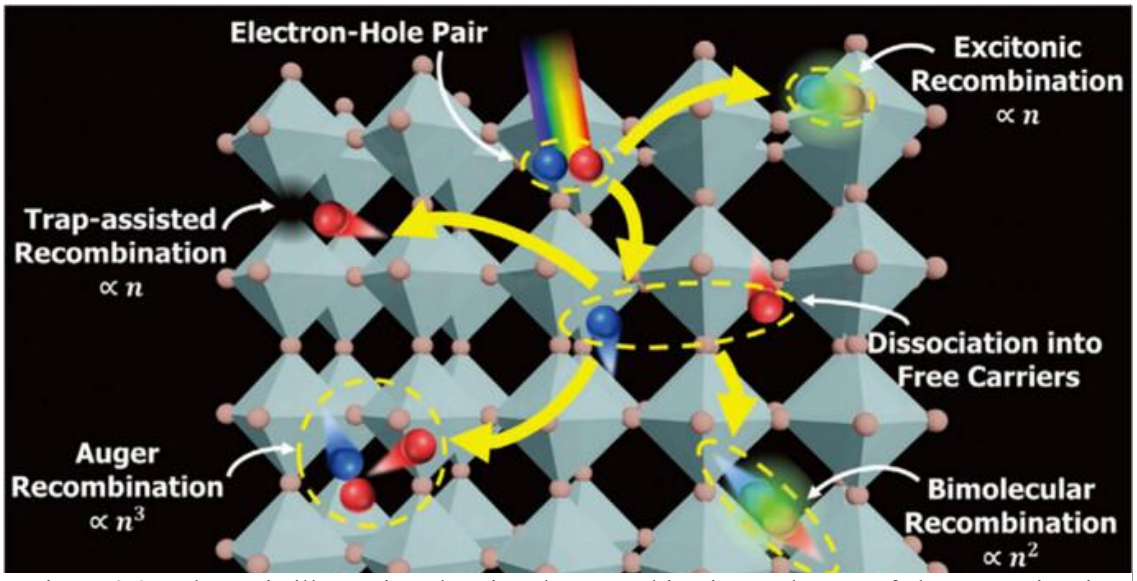

Figure 2.9. Schematic illustration showing the recombination pathways of charge carriers in quasi-2D PVSKs. [67]

recombination. Typically, the PLQY of quasi-2D PVSKs is calculated using the following equation:

$$1 \quad PLQY = \frac{k_{exciton}+k_2N}{k_{exciton}+k_{trap}+k_2N+k_3N^2}$$

In this equation, k_{exciton} represents the first-order excitonic recombination rate, k_2 is the bimolecular recombination rate, N denotes the carrier density, k_{trap} is the monomolecular trap-assisted recombination rate, and k_3 is the three-body Auger recombination rate. Based on this equation, the PLQY is highly dependent on N and reflects the competition between first-order recombination, bimolecular recombination, and Auger recombination.

Trap-mediated recombination occurs when a single electron or hole is trapped at a sub-bandgap electronic state and recombines with the opposite charge, which can be either a hole from VB or an electron from CB. This process is non-radiative and generates phonons [68]. The recombination rate is determined by both the number of trapping sites and the rate at which free carriers encounter the trapped carriers. The kinetics of this process can be described by Shockley-Read-Hall recombination, which was previously applied to inorganic semiconductors. Due to its monomolecular kinetic nature, trap-assisted recombination exhibits a linear (first-order) relationship with the density of free charge carriers [69].

Bimolecular recombination refers to the band-to-band recombination of a free electron and a free hole, resulting in the release of a photon. In PVSK materials with a direct bandgap, the intrinsic constant for bimolecular recombination is independent of material processing factors (such as surface defects or grain boundaries) but is primarily determined by the electron-hole interaction cross-sections and their group velocities. The rate of bimolecular recombination is limited by the motion of both electrons and holes, leading to a second-order relationship with the density of free charge carriers [70].

Auger recombination involves the relaxation of an excited electron, transferring its energy to excite a second electron to a higher energy state within the conduction band. The energy and momentum from this process are typically lost to intra- or interband transitions, making it a non-radiative process. Since the Auger process involves three particles, it follows a third-order relationship with the density of free carriers.

Specifically, under low excitation intensity, the PLQY is influenced by the balance between first-order excitonic recombination and trap-assisted nonradiative recombination [80]. As

N increases, radiative bimolecular recombination gradually surpasses monomolecular recombination. However, when Auger recombination becomes dominant at higher N, the PLQY experiences a sharp decline. Additionally, the PLQY depends on the recombination coefficients $k_{exciton} + k_{trap}$ (denoted as k_1), k_2, and k_3. According to the equation, the PLQY reaches its maximum value of $(1 + 2\sqrt{k_1 k_3/k_2})^{-1}$ at the carrier density of $\sqrt{k_1 k_3}$. Therefore, reducing the nonradiative recombination rates k_1 and k_3 is an effective strategy to enhance the PLQY. In general, the PLQY of quasi-2D PVSKs is primarily influenced by factors such as film quality, the value of E_b, energy-transfer efficiency, and recombination pathways at the interfaces.

2.4.5 Stability

Quasi-2D PVSKs exhibit higher stability compared with the three-dimensional type due to better resistance to environmental, thermal, and photodegradation phenomena. These have a significantly higher hydrophobicity and inhibit ion migration, resulting in better durability under ambient conditions, and contribute to their increased stability [58, 71–74]. Bulky organic spacer cations are incorporated to prevent inorganic degradation pathways by protecting the inorganic framework from oxygen and moisture. Therefore, selection and design of these spacer molecules may improve the stability under external scenarios. Fluorinated organic cations have been particularly successful in modulating film morphology, encouraging larger grain development, raising hydrophobicity and encouraging a better vertical orientation of the perovskite layers.

The thermal stability of the quasi-2D perovskite material relies not only on its intrinsic decomposition but also on the changes in phase distribution across dimensionality. Spacer cations drive this pattern. For example, Chen et al. showed that adding the hydrophobic molecule 4-(trifluoromethyl)benzylamine (4TFBZA) to $MAPbI_3$ greatly decreases trap densities and reduces ionic migration [75]. Additionally, the strong hydrogen bonding between 4TFBZA and methylammonium ions stabilizes the structure during high temperatures by restraining thermal decomposition. The photostability of quasi-2D perovskite in various forms is mostly governed by the relationship between the photodegradation and photooxidation processes, both the characteristics of the spacer cations and the thickness (n value) of the inorganic layer, which affect the photostability. For example, Rand and colleagues demonstrated that as surface capping agents, long-chain ammonium cations are effective in suppressing halide migration and phase segregation, providing improved photostability [76]. Similarly, Tarasov et al. reported that quasi-2D BA_2MA_{n-}

$_1Pb_nI_{3n+1}$ films exhibit non-linear dependence of the photodegradation rates to the layer thickness and maximum stability for $n \geq 3$ was found by photoluminescence [77]. Encapsulation and passivation are two techniques extensively used to improve the photostability effect, as well as surface and edge state passivation. Encapsulation serves as an obstructing agent against ingress of oxygen, and inhibits the escape of volatile degradation products thereby suppressing both photooxidation and photodegradation processes.

2.5 Photoluminescence modulation of 2D and Quasi-2D PVSKs

Quasi-2D PVSKs exhibit high PLQYs and exceptional stability due to efficient energy transfer, effective exciton recombination, and low defect density. The photoluminescence properties of quasi-2D PVSKs can be systematically tuned through strategies such as engineering large organic cations, modifying monovalent cations, altering halogen composition, implementing defect passivation, and adjusting dimensionality. The subsequent sections present a detailed analysis of these modulation techniques and their impact on the properties of quasi-2D PVSKs.

2.5.1 A-site cation engineering

Monovalent cation engineering has proven highly effective in modifying the ionic radius of the A-site cation of PL in quasi-2D perovskite, as it has been shown effectively to adapt PL properties of quasi-2D perovskite. Modifications of this nature result in variations of the Goldschmidt tolerance factor leading to structural distortions that modulate the band gap [78–80]. Furthermore, this approach can inhibit the redshift in light spectrum of halide segregation-related redshift, and it is extremely promising for the design of stable quasi-2D perovskite light emitter LEDs. Recent years have seen substantial research efforts looking at using the engineering of monovalent cation as a mechanism to enhance the quality of the films and optical performance. For instance, Yuan et al. using RbBr in precursor solution prepared for preparation of Rb–Cs alloyed quasi-2D perovskite films composed of $PEA_2(Rb_xCs_{1-x})_2Pb_3Br_{10}$ ($0 \leq x \leq 1$) by spin coating [81]. The resulting films showed a very smooth top surface, with roughness of only 0.82 nm, and isotropically oriented crystallites, identified by grazing-incidence wide-angle X-ray scattering (GIWAXS). For any number of n-phase species the excitonic features related to various species of the n-phase increased over time and the Rb content allowed the PL emission constant tuning from green to blue. Notably, the $PEA_2(Rb_{0.6}Cs_{0.4})_2Pb_3Br_{10}$ composition exhibited highly improved PL intensity and PLQY, as compared to their respective three-dimensional perovskite

($(Rb_{0.6}Cs_{0.4})PbBr_3$). Following the addition of RbBr, PLQY values increased substantially; it was even shown to be more than 82%. Transient absorption studies showed the formation of higher-n ($n \geq 5$) domains with the incorporation of Rb led to better energy transfer and improved radiative recombination.

Similarly, You et al. added larger monovalent cations (such as ethylammonium (EA^+)) to the prepared precursor solution for preparation of $PEA_2(Cs_{1-x}EA_xPbBr_3)_2PbBr_4$ films [82]. The EA^+ incorporation into the $CsPbBr_3$ lattice allowed for a quasi-2D $Cs_{1-x}EA_xPbBr_3$ phase to be produced. This structural alteration reduced Pb–Br orbital interaction and promoted band gap enhancement that would permit blue field-emission. The absorption edge had clear blueshift and PL emission was tuneable from green (508 nm) to blue (466 nm). The PLQY (70% or greater) was enabled by EA integration by suppressing nonradiative recombination pathways. The films showed very good operating performance in the presence of continuous UV irradiation and thermal stress.

In a further study, Xing et al. investigated the partial substitution of FA^+ with Cs^+ in $PEA_2FA_2Pb_3Br_{10}$ systems with the addition of CsBr to the precursor solution [83]. These films have yielded $PEA_2(FA_xCs_{1-x})_2Pb_3Br_{10}$ films with a morphological improvement through enhanced crystallization kinetics and smooth and densely packed structure, mainly due to accelerated crystallization kinetics due to Cs^+ incorporation. Optical absorption measurements at 530 nm were generally characteristic of band-edge values with marked excitonic features observed near 430 nm, in agreement with the dominant n = 2 phase formation. Fine adjusting the FA:Cs ratio provided the opportunity to achieve an optimal PLQY of ~20% for a ratio of 0.8. Results were ascribed to decreased trap-assisted nonradiative recombination, as evidenced by low trap densities with increasing quantity of Cs.

2.5.2 Halogen engineering

Quasi-2D PVSKs can be modified by adjusting the ratio of mixed halide anions to increase or decrease the band gap, thus providing the opportunity for halogen engineering to be a widely used method for PL characteristics tuning. For instance, Yao et al., mixed $PbBr_2$ and $PbCl_2$ in the precursor to form a quasi-2D PVSK film $PBA_2(CsPbBr_xCl_{3-x})_{n-1}PbBr_4$ through spin-coating [84]. The corresponding crystals aligned to the (020) plane parallel to the substrate, and the crystallinity improved slightly at the higher Cl content, which caused the lattice contraction. As depicted in

Figure 8a, the absorption edge of the $PBA_2(CsPbBr_xCl_{3-x})_{n-1}PbBr_4$ film moved from longer to shorter wavelengths with higher Cl fractions and several absorption peaks indicated the generation of quasi-2D PVSKs of variable phases. The change of the PL emission peak was a result of Cl content increase, since it changes from green (504 nm) to blue (470 nm) suggesting a tunable band gap due to mixed Cl– and Br– ions. The PLQY of the $PBA_2(CsPbBrxCl_{3-x})_{n-1}PbBr_4$ film was reduced with more content of Cl but the full width at half maximum (FWHM) was quite nearly unaffected around 21–23 nm.

In a further study, Sargent et al. prepared a quasi-2D PVSK film called $PEA_2Cs_{1.6}MA_{0.4}Pb_3Br_{10}$ spin-coated for further DPPOCl treatment [85]. Their results show that DPPOCl reacts with trace amounts of water in the precursor solution, and the resultant solution of DPPOOH and Cl– ions were produced. These Cl– ions are partially integrated into the perovskite lattice, replacing some Br– ions and forming a $PEA_2Cs_{1.6}MA_{0.4}Pb_3Br_{10-x}Cl_x$ film. DPPOOH engaged with unsaturated lead dangling bonds on the periphery of the perovskite through P=O:Pb interactions and hydrogen bonds with halide ions (O–H···Cl and O–H···Br). DPPOCl treatment also reduced size distribution and diminished the effect of phase separation. Thus, PL spectrum of the $PEA_2Cs_{1.6}MA_{0.4}Pb_3Br_{10-x}Cl_x$ film exhibits a gradual blueshift with increasing Cl and DPPOCl concentration, although its PL lifetime remained largely unchanged, which is probably due to decreased nonradiative recombination processes.

2.5.3 Dimensionality engineering

Quasi-2D PVSKs are composed of mixed phases with n values ranging from low to high, enabling dimensionality engineering a powerful approach to tune optical properties. Changes in average n values can be manipulated by varying concentrations of larger organic cations for quasi-2D PVSKs. Low average n values lead to poor optical performance resulting in inefficient energy transfer, poor charge mobility, strong electron–phonon interaction, and a large exciton–exciton annihilation—factors which result in nonradiative recombination pathways. So, it is important to improve the mean n value for the optical effectiveness of quasi-2D PVSKs.

For example, Yang et al. incorporated MeS molecules into the precursor solution of PVSK and spin coated to form a quasi-2D $BA_2Cs_{n-1}Pb_nBr_{3n+1}$ film. Addition of MeS changed the phase distribution inside the PVSK, reducing uncoordinated Pb^{2+} ions. The strong hydrogen-bonding interaction of $-SO^{3-}$ of MeS and BA spacer cations effectively influenced crystallization

dynamics, promoting larger amounts of large-n phases with narrow-band-gap quantum wells (QWs). It also increased exciton energy migration from small-n to large-n phases.

Additionally, Sargent et al. indicated that varying confinement in QWs within quasi-2D PVSKs could result in nonradiative recombination losses and broadened emission spectra. To mitigate this problem, TFPPO molecules were added to the precursor solution to produce a quasi-2D PVSK $PEA_2Cs_{1.6}MA_{0.4}Pb_3Br_{10}$ film via spin-coating. The hydrogen atom present in TFPPO forms a bond with the organic cation (PEA), allowing for better control over PEA diffusion during spin coating while limiting the development of low-thickness QWs. Treatment with TFPPO led to dense, smooth, and uniform PVSK films exhibiting narrow-band emission and high PLQY, attributed to enhanced radiative recombination efficiency.

2.5.4 Large cation engineering

Quasi-2D PVSKs are layered crystals consisting of alternating inorganic $[BX_6]^{4-}$ octahedral frameworks, together with large organic cations or ligands. This unique framework makes it possible to engineer large organic cations. This is crucial in tuning their optical and electronic properties. Alterations to these organic components can carry additional electronic states, affect energy transfer processes and produce distortion in the inorganic lattice, affecting PL properties [49, 55, 86-88]. Weak van der Waals gaps between neighbouring inorganic layers may also retard efficient transfer of energy and reduce structural stability [89,90]. Thus, rational design and maximization of large organic cations are important in optimizing quasi-2D PVSK materials performance.

Recent works have emphasized on this approach in order to realize high-efficiency systems. For instance, Liao et al. used two organic ligands, PEABr and $NPABr_2$, to synthesize a $PEA_2NPA_1Cs_2Pb_3Br_{12}$ quasi-2D perovskite film by spin coating the precursor solution [91]. This film shows an ultrasmooth morphology with a surface roughness of 0.98 nm and a free area of pinholes. Compared with films with single ligands ($PEA_2Cs_2Pb_3Br_{12}$ and $NPA_1Cs_2Pb_3Br_{12}$), the dual-ligand technology exhibited various UV–vis and PL phenomena which were due to combined effects between PEA and NPA. More precisely, PEA-based films had a wide phase distribution between n=1 and n= ∞, the NPA-based ones a single phase with relatively similar thickness. In the mixed-ligand film the ratio of n = 2 to n = 3 layered structures were mostly observed. This

compositional tuning resulted in an emission color change from green (508 nm) of the PEA-only film to blue emission and the mixed system with a similar composition as in the NPA-based film. In addition, the photoluminescence quantum yield (PLQY) greatly increased to 20% compared to 6% of the NPA-only film.

Similarly, Su et al. applied together PBABr and PABr as co-interlayer ligands for producing (PBA/PA)$FA_{n-1}Pb_nBr_{3n+1}$ quasi-2D PVSK films [92]. By varying the amount of these ligands, a specific control over the crystallization and film morphology was obtained. Optical absorption analysis showed that increasing the percentage of PABr led to development of lesser-n (especially n = 2) and suppressed higher-n ($n \geq 3$) phases. Such compositional tuning led to a significant increase in PLQY, (from approximately 65% to 89%), as well as a significantly increased photoluminescence lifetime compared to a single-ligand system.

Elsewhere, Choy et al. prepared a bifunctional ligand 4-(2-aminoethyl)benzoic acid (ABA) to be applied in the precursor for the formation of $PEA_xPA_{2-x}(CsPbBr_3)_{n-1}PbBr_4$ quasi-2D PVSK films [93]. The introduction of ABA successfully decreased interlayer van der Waals gaps and facilitated interlayer coupling by its amino and carboxylic functional groups. The absorption spectra displayed features associated with n = 2 and n = 3 phases at about 428 and 453 nm respectively and a tail at longer wavelengths (~481 nm) suggesting higher-n phases. Improved interlayer interactions enhanced energy transfer efficiency, while the functional groups performed as defect passivation mechanisms by inhibiting metallic lead formation and lessening nonradiative recombination. This resulted in the observation of higher photoluminescence intensity of the ABA-modified films than pristine samples.

2.6 Emerging two-dimensional organic semiconductor incorporated quasi-2D PVSKs

2D PVSK systems are known to share a quantum-well architecture of inorganic layers separated by barrier structures. Within these systems, the HOMO of organic ligands operates below the inorganic framework VBM and the LUMO is located above the CBM. Such a large HOMO–LUMO gap is mostly ascribed to the insulating nature of the short-chain non-conjugated organic ligands. By introducing 2D organic ligand conjugated with a π long system, the band alignment can be modulation and the quantum-well structure can be shifted from type I to type II or even reversed type I configurations of hybrid organic–inorganic systems [94-97]. To distinguish

among these materials from typical hybrid perovskite, such 2D semiconducting perovskites integrated with functional conjugated organic cations are called conjugated organic cation incorporated perovskites (COCiPs). The COCiPs are applied in optoelectronic devices with several benefits.

(i) Rational molecular design, in turn, means the precision of energy level alignment can be controlled so that type I, type II and reversed type I band structure of devices result in large and tunable optoelectronic behaviour [94].

(ii) By secondary intermolecular interactions the structural optimization provides better order in the organization of organic layers, thereby reducing lattice strain and increasing the transfer capability of charge [95].

(iii) These materials provide a promising medium for modeling photophysical processes within self-assembled heterostructures on charge and energy transfer [96].

(iv) The rigid and hydrophobic structure of conjugated organic cations provides an excellent barrier to moisture penetration and ion migration and greatly improves environmental stability compared to short-chain 2D and 3D perovskites [97].

2.6.1 Molecular design of conjugated ligands

Conjugated organic ligands play a very important role to introduce new electronic functionalities in COCiPs. Nonetheless, the rational design and synthesis of such ligands—using optimal molecular geometry and efficient incorporation in 2D perovskite frameworks—still prove to be difficult and depend on wide-ranging experimental optimization. One promising design strategy capitalizes on these 2D PVSKs out-of-plane structural flexibility by increasing the π-conjugation level on the ligand layer, thus reducing the HOMO–LUMO gap. Conversely, the ligand has to preserve a relatively small cross-sectional size in order to fit the small gaps between the corner-sharing octahedral units of the inorganic lattice [98,99]. Relatedly, previously described conjugated ligands which can form 2D PVSKs, sorted by the number of aromatic rings, are listed in Figure 2.10, which have been further categorized into other types for polymeric or structurally unique systems. Simpler ligands with only one aromatic ring are excluded as due to their large HOMO–LUMO gaps as well as their insulating behaviour, they are considered conventional ligands. Ligands used in COCiPs can be broadly divided into four structural components: head group, conjugated core, linker, and side chains. The head group is usually a primary ammonium

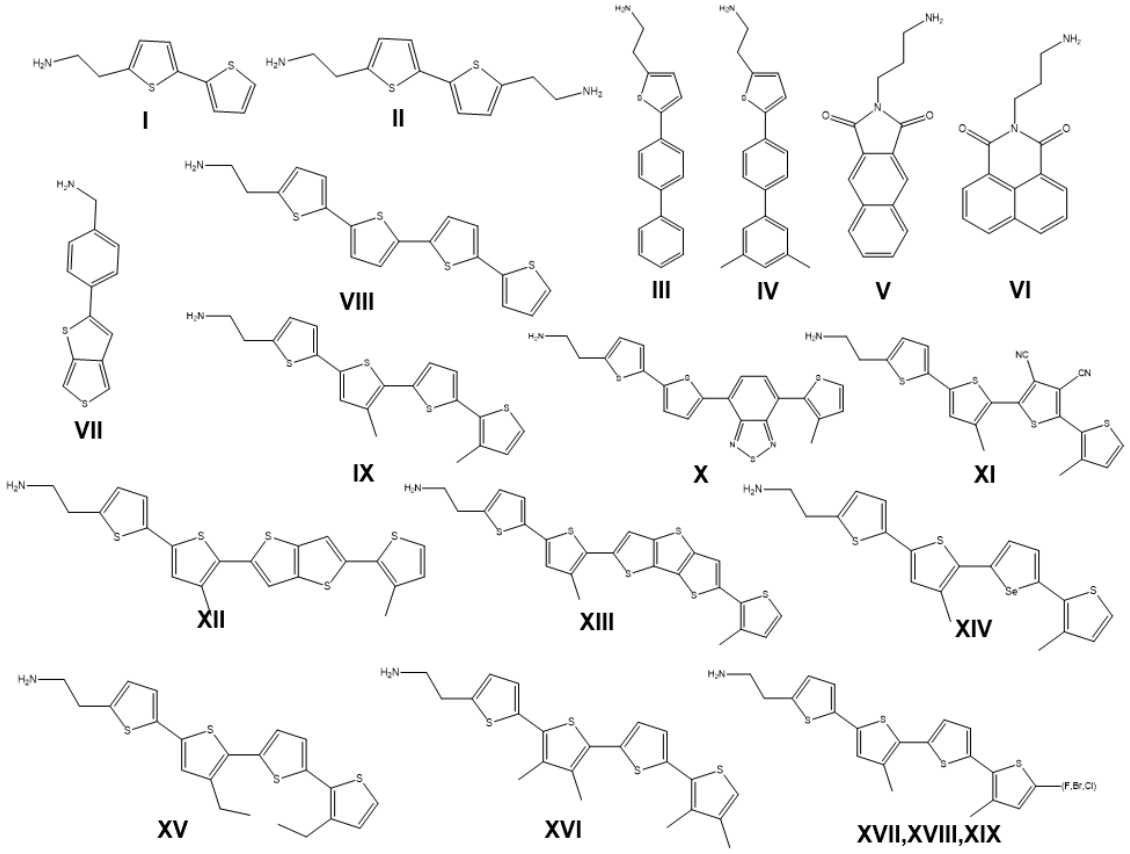

Figure 2.10. Conjugative organic cations that form 2D halide PVSKs. **(I)** 2-([2,2′-bithiophen]-5-yl)ethan-1-aminium **; (II)** 2,2′-([2,2′-bithiophene]-5,5′-diyl)bis(ethan-1-aminium)**; (III)** 2-(5-(2,2′-dimethyl-[1,1′-biphenyl]-4-yl)thiophen-2-yl)ethan-1-aminium **; (IV)** 2-(5-(3′,5′-dimethyl-[1,1′-biphenyl]-4-yl)thiophen-2-yl)ethan-1-aminium**; (V)** 3-(1,3-dioxo-1,3,3a,9a-tetrahydro-2H-benzo[f]isoindol-2-yl)propan-1-aminium**; (VI)** 3-(1,3-dioxo-1H-benzo[de]isoquinolin-2(3H)-yl)propan-1-aminium**; (VII)** thieno[3,2-b]thiophene-2-phenylmethylammonium**; (VIII)** 2-([2,2′:5′,2″:5″,2‴-quaterthiophen]-5-yl)ethan-1-aminium**; (IX)** 2-(3‴,4′-dimethyl-[2,2′:5′,2″:5″,2‴-quaterthiophen]-5-yl)ethan-1-aminium**; (X)** 2-(4′-methyl-5′-(7-(3-methylthiophen-2-yl)benzo[c][1,2,5]thiadiazol-4-yl)-[2,2′-bithiophen]-5-yl)ethan-1-aminium**; (XI)** 2-(3″,4″-dicyano-3‴,4′-dimethyl-[2,2′:5′,2″:5″,2‴-quaterthiophen]-5-yl)ethan-1-aminium**; (XII)** 2-(4′-methyl-5′-(5-(3-methylthiophen-2-yl)thieno[3,2-b]thiophen-2-yl)-[2,2′-bithiophen]-5-yl)ethan-1-aminium**; (XIII)** 2-(4′-methyl-5′-(6-(3-methylthiophen-2-yl)dithieno[3,2-b:2′,3′-d]thiophen-2-yl)-[2,2′-bithiophen]-5-yl)ethan-1-aminium**; (XIV)** 2-(4′-methyl-5′-(5-(3-methylthiophen-2-yl)selenophen-2-yl)-[2,2′-bithiophen]-5-yl)ethan-1-aminium**; (XV)** 2-(3‴,4′-diethyl-[2,2′:5′,2″:5″,2‴-quaterthiophen]-5-yl)ethan-1-aminium**; (XVI)** 2-(3′,3‴,4′,4‴-tetramethyl-[2,2′:5′,2″:5″,2-quaterthiophen]-5-yl)ethan-1-aminium**; (XVII)** 2-(5‴-fluoro-3‴,4′-dimethyl-[2,2′:5′,2″:5″,2‴-quaterthiophen]-5-yl)ethan-1-aminium**; (XVIII)** 2-(5‴-chloro-3‴,4′-dimethyl-[2,2′:5′,2″:5″,2‴-quaterthiophen]-5-yl)ethan-1-aminium**; (XIX)** 2-(5‴-bromo-3‴,4′-dimethyl-[2,2′:5′,2″:5″,2‴-quaterthiophen]-5-yl)ethan-1-aminium**.**

that minimizes steric hindrance and mediates ionic bonding with the $[BX_6]^{4-}$ octahedral framework. The linker, which usually has one or 2 carbons, links the head to the conjugated core.

The central conjugated unit can contain a myriad of aromatic or unsaturated structures such as thiophene, benzene, naphthalene, heteroaromatic rings, or carbon–carbon double bonds. Side chains (commonly introduced at positions other than that of the ammonium group) are then introduced at the opposite sides of the molecule to facilitate more functionalization. The overall molecular structure is very important for shaping ligand packing, as well as generating secondary intermolecular interactions, distortions to the octahedra in the inorganic lattice and the formation of the 2D perovskite structure. Ligands with two aromatic rings are typically synthesized via carbon–carbon cross-coupling reactions or direct modifications of naphthalene. These two-ring structures are relatively easy to synthesize, and the resulting COCiPs usually adopt type I band alignment [100]. Naphthalene, for instance, was incorporated into PVSK structures in the 1990s, with enhanced phosphorescence observed [101]. Modifying the linker length on naphthalene affects the penetration depth of the ammonium head group and the distortion of the inorganic layers. Bithiophene-based ligands (such as **I** and **II**) can form both DJ-phase and RP-phase 2D PVSKs [102,103]. A series of DJ-phase PVSKs with diammonium thiophene ligands (ranging from two to five units) and RP-phase PVSKs with monoammonium thiophene (ranging from two to four units) were developed, with longer chains not disrupting the formation of 2D structures. Other aromatic backbones, such as biphenyl or stilbene, have also been reported in conjunction with 2D PVSKs [104-106]. Additionally, incorporating photoswitchable azobenzene into the PVSK lattice is an interesting concept, but further optical studies are needed to confirm its photoswitching properties [107,108].

Conjugation on three aromatic rings sometimes comes with solubility and processing barriers, leading to obstacles in the actual device assembly [109]. To minimize these problems, ligands like III and IV were designed using methyl substituents for destabilizing planarity and structural deformation, which resulted in improving processability and LED performance. For example, three-ring conjugated ligands prepared from naphthalene cores and ligands using fluorophores in the 2D PVSK matrices are capable of tunable photoluminescence [101]. Deleporte et al. doping 10% of ligand V into PEA_2PbBr_4 (PEA = phenylethylammonium) framework significantly increased luminescence [110]. It was assigned to higher crystallinity and possibly resonance interactions between Wannier and Frenkel excitons. The same doping methods have been used in other systems (VI and VII) to realize room-temperature phosphorescence with triplet energy transfer mechanisms as well [111-113]. A class of mono-ammonium ligands from

quaterthiophene was also used and developed in order to study structure–property relation in 2D PVSKs. For instance, ligand VIII could be considered as an analogue to the butylammonium analogue where all the carbon are ablated for the thiophene rings [102]. Methyl substituents to disrupt planarity will yield ligand IX instead of VIII, which further improve solubility and processability [102]. Adaptable IX ligand has been extensively used in the field of optoelectronic research, ion migration in heterostructures, and use in solar cells, field-effect transistors, and thermoelectric devices [114-116]. IX was modified to include ligand X with the benzothiadiazole unit, and ligand XI with electron-withdrawing cyano moieties. Ligand X has a significantly narrower band gap and a reversed type-I band alignment with $[PbI_6]^{4-}$ octahedra [117].

Further morphological modification, for example the substitution of thiophene with the fused systems thienothiophene or dithienothiophene (ligands XII and XIII) provides enhancement of molecular planarity and enhanced intermolecular interactions and support to nucleation through structural modification [118]. Selenophene (ligand XIV) can also be replaced in this way that has the same properties as ligand XIII [119]. Changes to side chains, such as ethyl substitutions or enhanced methylation (e.g., ligands XV and XVI) modify solubility and lattice strain, resulting in clear differences in surface morphology patterns in 2D/3D PVSK heterostructures. Furthermore, halogen functionalization (e.g., XVII to XIX) offers reliable energy adjustment strategies. In the second layer, polymerized 2D COCiPs are formed by the continued expansion of conjugation. Many polymers, including polydiacetylene, polythiophene, polyaniline, polyacetylene, and polystyrene, which have been realized with ammonium groups, have been included as interconnected organic spacers in perovskite lattices [120-124]. Such polymer-based systems have exhibited enhanced mechanical and environmental stability. However, the formation of high-quality single crystals is an open challenge, and the majority of the researches are limited to the thin-film forms at the present. Further, polymerization conditions must be well treated to prevent the degradation of the perovskite structure, especially through adverse thermal or ultraviolet treatment. Secondary and tertiary amine-based head groups may also be applied, but they generally yield a dramatic change from the conventional crystal structure of the inorganic framework [125].

2.6.2 2D organic semiconductor incorporated PVSKs structure-properties relationship

2D PVSKs are intrinsic quantum-well structures, in which the inorganic layers serve as quantum wells, separated at the molecular scale by organic barrier layers that exhibit low dielectric constants [126]. Due to strong quantum and dielectric confinement effects, such systems tend to have large effective band gaps (often exceeding 2.5 eV) and high exciton binding energies, often exceeding 400 meV for lead-based halide perovskites [17, 55, 127]. Moreover, by increasing the number of inorganic layers (n), collectively referred to as forming "quasi-2D" structures, effectively thickening the well and make the band gap smaller. Metal cation choice further determines the electronic structure, since for instance Pb-based perovskites usually have bigger band gaps than Sn-based ones [128]. Furthermore, the characteristic of the halide ions (such as Cl, Br, I) affects their VBM through their hybridized p orbitals (Cl > Br > I) and thus exhibits a band gap trend of Cl > Br > I [129]. In contrast, organic spacers—especially in COCiP systems comprising longer conjugation—may also introduce frontier orbitals, alleviate dielectric mismatch, and indirectly modulate the band gap by a distortion of the lattice structure [97]. The differences in band alignment and steady state optical properties of COCiP materials produce various charge separation, recombination and energy transfer dynamics, as demonstrated by time-resolved spectroscopic investigations. The charge transport of 2D halide PVSKs is intrinsically anisotropic with relatively high in-plane conductivity, which can be attributed to continuous inorganic frameworks and poor out-of-plane transport due to insulating organic layers. Adding more inorganic layers improves overall conductivity by lowering the quantity of organic barriers. The first studies by Stupp et al. in out-of-plane transport in single-crystal 2D PVSKs evidenced that systems utilizing larger aromatic ligands, such as perylene and pyrene, displayed an enhanced conductivity to those using aliphatic spacers in relation to the system surface because of alignment to the inorganic lattice [130]. Conjugated polymers in the in-plane direction, for example polydiacetylenes can greatly increase charge transport over wide-length π-conjugated networks. In addition to J–V measurements done at electrode contacts, contactless methods, such as time-resolved microwave conductivity, are also used to investigate charge transport for 2D PVSKs [131-134]. In tandem with single-crystal analysis, these measurements have shown that ligands like XIX, which encourage higher packing efficiency deep in the organic layers, are the most conductive among halogen-substituted IX derivatives. Conductive atomic force microscopy also

offers spatial mapping of surface conductivity. Specifically, 4-fluorophenethylamine (F-PEA)-based 2D PVSKs possess nearly an order of magnitude higher conductivity relative to PEA-based systems employing an edge-to-face packing arrangement.

2.7 Aggregation-induced emission dyes

In aggregate form, luminophores might show reduced emission, preserved, or improved emission relative to their behavior in dilute solutions. In most standard systems, aggregation induces emission to be partially or completely quenched. This phenomenon, called aggregation-caused quenching (ACQ), dates back to Förster's 1954 report about concentration quenching [135]. Subsequent research studies have given a holistic characterization of the photophysical mechanisms behind ACQ. Usually, such luminophores have strong emission in dilute solutions, but experience large quenching when they aggregate. It's because tight molecular packing allows for strong intermolecular π–π interactions, particularly in planar or rod-like aromatic systems [136]. Such interactions favour non-radiative decay pathways in the excited state, thus reducing fluorescence. ACQ is generally not practical because it is ubiquitous and harmful. A representative example of ACQ behavior is perylene. With a good solvent such as tetrahydrofuran (THF), the fluorescence in dilute perylene solutions shows a strong reaction. However, as a ratio of poor solvent (e.g., water) increases, aggregation occurs resulting in a slow emission drop. At high water fractions (fw ≈ 80–90 vol%), strong aggregation causes quenching nearly to completion. This effect is due to planar polycyclic structures in perylene. The structure fosters ordered molecular stacking and excimerization, through π–π interactions.

By contrast, aggregation-induced emission (AIE) represents an opposite photophysical phenomenon: it was first discovered in 2001 [137]. In AIE systems, some luminogens are weakly emissive or non-emissive in solution but may become very luminescent upon aggregation. Where conventional "luminophores" emit as single molecules, however, AIE systems' "luminogens" are tailored to emit in a cohesive way, and such materials are often known as AIEgens. A classic example is hexaphenylsilole, which emits little in a good solvent such as THF but becomes highly emissive when aggregated (e.g., at high water volumes, ~80 vol%) [138]. Tetraphenylethene is another AIEgen well established with a central double bond and four phenyl rings [139]. In dilute solution, TPE shows little emission since the intramolecular rotations of the phenyl rings can dissipate excitation energy through non-radiative routes. Furthermore, the central olefinic bond is subject to structural relaxation mechanisms that also lead to loss of energy. In contrast, upon

aggregation, these intramolecular motions are restricted—a mechanism known as restriction of intramolecular rotation — which suppresses non-radiative decay and triggers strong emission. The twisted molecular geometry also prevents close π–π stacking, and further supports radiative recombination. The same mechanisms are evident in other propeller-shaped AIEgens. In the case of luminogens possessing a flexible and highly vibrational structure, the AIE effect can also occur owing to restriction of intramolecular vibration RIV. Vibrational motions in those systems become channels for dissipating non-radiative energy. As aggregation limits these motions, radiative decay becomes a more beneficial process. For example, in 10,10′,11,11′-tetrahydro-5,5′-bidibenzo[a,d]annulenylidene, the suppression of vibrational freedom has a major influence on the AIE of THBA [140]. Despite extensive studies and a rich background on ACQ, however, these materials (ACQphores) often demonstrate relatively poor solid state behavior due to diminished emission upon aggregation. This limits them from operating in real-world devices. AIE-activated compounds, on the other hand, disrupt the existing paradigm by exhibiting increased emission in aggregated form. AIEgens create more creative solutions in optoelectronics and photonics with applications that are hard to realize with conventional luminophores. More broadly, AIE systems show that it is indeed possible to achieve greater emission in aggregated molecular networks due to concerted molecular activity than individual molecules, leading to novel material strategies.

CHAPTER 3: EXPERIMENTAL METHODS

3.1. Materials

Aggregation induced emission dye

4-Hydroxybenzaldehyde (98%) and 3-(Boc-amino)propyl bromide (95%) were sourced from AKScientific. Additionally, 4′-methoxy-[1,1′-biphenyl]-4-carbaldehyde (96%) and 2,3,4,5,6-pentafluorophenyl acetonitrile (98%) were acquired from Thermo Fisher Scientific. The following reagents were obtained from Merck: trifluoroacetic acid (99%), a tetrabutylammonium hydroxide solution (1.0 M in methanol), anhydrous potassium carbonate (ACS reagent, ≥99%), sodium bicarbonate (ACS reagent, ≥99.7%), sodium hydroxide (98%), boron tribromide (99.9%), dichloromethane (98%), acetone (99.5%), and tert-butanol (99.3%).

2D and quasi-2D PVSKs

Lead (II) iodide (PbI_2, 98%), Lead (II) bromide ($PbBr_2$, 98%), methylammonium iodide (MAI, 98%), methylammonium bromide (MABr, 98%), formamidinium iodide (FAI, 98%), Butylamine (BA, 99.5%), Octylamine (OA, 99%), Acetic acid (99%), hydroiodic acid (57 wt% in water), hydrobromic acid (48%), dimethyl formamide (DMF, anhydrous 99%), and dimethyl sulfoxide (DMSO, anhydrous 99%) were obtained from Merck. Indium-doped and fluoride-doped tin oxide substrates (ITO and FTO) were sourced from OPV Technology in China. All chemicals were utilized as received without any additional purification.

3.2. Aggregation induced emission dye synthesis

Both precursors of the AIEE LP cations, (Z)-2-([1,1′-biphenyl]-4-yl)-3-(4-(3-aminopropoxy)phenyl)acrylonitrile (BPCSA) and (Z)-3-(4'-(3-aminopropoxy)-[1,1'-biphenyl]-4-yl)-2-(perfluorophenyl)acrylonitrile (FPCSA) were designed and synthesized by the following routes (see Figure 3.1). Detailed synthesis procedure for both AIEE LPs with NMR spectrums is presented in Chapter 4

3.3. Precursor solution preparation and thin film fabrication

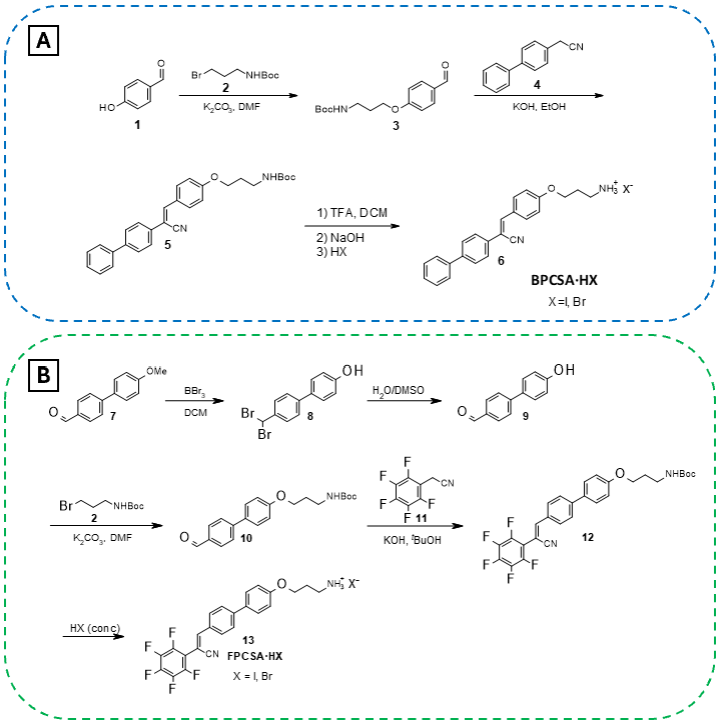

Figure 3.1. Synthetic route for (A) BPCSA and (B) FPCSA

The films were prepared on prepatterned ITO substrates, which were cleaned by sequential ultrasonic treatment in Hellmanex III solution, acetone, and isopropyl alcohol, with each solvent used for 10 minutes. To prepare the PVSK precursor solutions all precursor were mixed in certain stoichiometric ratio (see Table 3.1) in a vial and dissolved in DMF and DMSO (4:1 v/v ratio) by heating (up to 80 °C) and stirring. After stirring at 80 °C for 30 minutes, the PVSK precursor solution was spin-coated at 3000 rpm for 30 seconds, then annealed at 100 °C for 10 minutes to remove remaining solvent and to crystallize the film.

PbX_2, mmol	**MAX, mmol**	**OA, mmol**	**BPCSA/FPCSA, mmol**	**HX, mmol**	**Layer number, (*n*)**
0.05	-	0.1	-	0.12	1
0.05	0.027	0.033	-	0.04	2
0.05	-	-	0.1	0.12	1
0.05	0.027	-	0.033	0.04	2

Table 3.1. Stoichiometric ratio of PVSK precursors[1]

After vigorous mixing at 80 °C for 30 minutes, the PVSK precursor solution was spin-coated at 3000 rpm for 30 seconds, then annealed at 100 °C for 10 minutes to remove remaining solvent and crystallize the film.

3.4. Structural and spectroscopic characterization

3.4.1. X-Ray diffraction

X-ray diffraction (XRD) is a widely employed method for examining the crystallographic characteristics of materials. In crystalline structures, atoms are organized in a repetitive lattice formation, which leads to the diffraction of incoming X-rays by the atomic arrangement, resulting in interference patterns. The X-ray detector captures only constructive interference. By ensuring that the incident X-ray beam is phase-aligned and utilizing known values for wavelength (λ) and incident angle (θ), it is possible to determine the distinctive lattice spacing (d) through Bragg's law:

$$n\lambda = 2d \times sin\theta$$

where n signifies an integer indicating the order of diffraction. In systems with highly ordered atomic arrangements, most diffraction occurrences are elastic, which results in sharp peaks with significant intensity and a narrow full width at half maximum (FWHM). A smaller FWHM correlates with greater crystallinity. XRD analyses were performed using a Rigaku Smartlab diffractometer equipped with Cu Kα radiation (λ = 1.54 Å). The crystallographic features of AIE dye integrated into 2D PVSK films were assessed as synthesized, and the resulting XRD spectra were evaluated using SmartLab studio software.

3.4.2. UV-vis absorption spectroscopy

UV-visible absorption spectroscopy is an efficient method for assessing the optical bandgap of semiconductor materials. This technique operates on the principle that molecules containing both bonding and non-bonding electrons are capable of absorbing photon energy, which promotes these electrons to higher antibonding molecular orbitals. Photons with energy exceeding the material's bandgap are absorbed, allowing for electronic transitions into the conduction band. During the procedure, a monochromatic light source is aimed at the sample, while a photodetector

[1] In the Table 3.1 X=I,Br

captures the transmitted light. The light source can be modified to scan across wavelengths from ultraviolet to visible (high to low). To eliminate any effects from the substrate of the sample, a reference substrate is first measured, and its data is deducted from that of the sample's absorption spectrum. The UV-visible absorption spectrum reveals absorption intensity as a function of wavelength, with the beginning point of absorption signifying the material's bandgap (Eg). The absorbance spectra for PVSK films within the UV-visible range were recorded using a PerkinElmer Lambda 1050 spectrometer. Initially, the absorption spectrum of the pure substrate was documented and later subtracted from that of the sample.

3.4.3. Steady-state photoluminescence

For radiative recombination processes and emission properties of semiconductor materials, steady-state photoluminescence (PL) spectroscopy is a widely used technique. This method depends on the excitation of electrons from the valence band to higher energy states upon absorption of photons with sufficient energy. After excitation, electrons relax to lower energy states and then recombine with holes, resulting in the emission of photons. The emitted light gives useful insight into the band structure, defect states, and recombination dynamics of the material. The steady-state photoluminescence spectra of the prepared thin films were measured using a fluorescence spectrophotometer (FLS1000, Edinburgh Instruments) equipped with a 200 W xenon lamp as the excitation source.

3.4.4. Time-correlated single photon counting

Time-correlated single photon counting (TCSPC) is an established method for studying the dynamics of charge carriers in semiconductor materials. This technique assesses the duration of a material's excited state following light excitation. It operates by detecting individual photons and logging their arrival times against a reference signal generated by a short-pulse laser. The laser emits periodic short pulses ranging from 5 to 10 picoseconds, which are divided into two identical beams via a beam splitter. One beam is directed at the sample to excite it, leading to the emission of photons that are captured by photodiode 1, while the second beam serves for synchronization purposes and is detected by photodiode 2. The timing electronics track the arrival times of fluorescence photons post-laser excitation. By aggregating these timings across several cycles, a computer generates an intensity versus time profile. TCSPC measurements were conducted utilizing an Edinburgh Instruments spectrometer (FLS1000) equipped with a 375 nm pulsed laser.

3.4.5. Ultraviolet photoelectron spectroscopy

Ul Ultraviolet photoelectron spectroscopy (UPS) is an analytical method that is particularly sensitive to surfaces, allowing for the measurement of the energy distribution of electrons that are emitted from the surface of a sample when exposed to ultraviolet light. This technique yields insights into the density of states present in various materials. Due to the limited penetration depth of photoelectrons, which is around 5 nm, UPS primarily captures signals from just the uppermost layer of the sample. In this investigation, UPS measurements were performed using a NEXSA spectrometer from Thermo Scientific under ultrahigh vacuum conditions (approximately 1 × 10^-10 mbar). The monochromatic UV source used delivered photons at an energy level of 21.2 eV. A negative external bias voltage of -10V was applied to the perovskite films during analysis, and the resulting UPS spectra were evaluated utilizing Avantage software.

CHAPTER 4: DESIGN AND SYNTHESIS OF AGGREGATION INDUCED EMISSION DYES

4.1. Introduction

To meet the requirements of 2D PVSK integration and proper energy level alignment, two AIEE LPs (Z)-2-([1,1'-biphenyl]-4-yl)-3-(4-(3-aminopropoxy)phenyl)acrylonitrile (BPCSA) and (Z)-3-(4'-(3-aminopropoxy)-[1,1'-biphenyl]-4-yl)-2-(perfluorophenyl)acrylonitrile (FPCSA) were designed and synthesized.. Among the well-known AIE-active scaffolds—such as tetraphenylethene, cyanostilbene, bis(styryl)anthracene, and hydroxyphenylbenzoxazole we focused on a rod-like cyanostilbene derivative. Both BPCSA and FPCSA have a rod-shaped cyanostilbene derivative framework that has 1D bulkiness and a diameter well fitted to the 2D PVSK lattice. The propylamine group could serve as an anchor to PbI_6^- octahedrons through hydrogen bonding between protonated amine and I^- ions and facilitates cocrystallization with 2D PVSK layers. By introducing fluorine atoms into the AIE LPs, the highest electronegativity of fluorine can effectively lower both the HOMO and LUMO energy levels [141,142]. This energy level modulation is key in tuning the optoelectronic properties of AIE LPs. When both electron-donating (D) and electron-accepting (A) groups are incorporated into the same AIE LP molecule, significant narrowing of the bandgap can occur due to intramolecular charge transfer. BPCSA and FPCSA (D-A configurations), are donor–acceptor hybrids that can achieve reduced bandgaps

through efficient intramolecular charge transfer. These structures are also expected to demonstrate enhanced third-order nonlinear optical effects.

By systematically combining different AIE LPs with 2D PVSKs, a broad range of energy alignments can be achieved to optimize energy and charge transfer in hybrid systems. The ammonium-terminated cations of AIE LPs can interact directly with 2D PVSK layers. For example, the synthesis of quasi-2D PVSKs can be carried out using AIE-halide salts (AIEX), methylammonium halide (MAX), and PbX_2, yielding compositions of $(AIE)_2MA_{n-1}Pb_nX_{3n+1}$, where *n* defines the PVSK layer thickness.

The synthesis of BPCSA was accomplished via a sequence of Williamson etherification, Knoevenagel condensation, followed by acid-catalyzed deprotection of the amine-protecting group. BPCSA·HX was obtained by stirring the BPCSA base in concentrated HX (X=I, Br). FPCSA·HI was synthesized by sequence of demethylation, Williamson etherification, Knoevenagel condensation and HI-catalyzed deprotection of the amine-protecting group.

4.2.Synthesis of the proposed AIE dyes

4.2.1. Synthesis of BPCSA

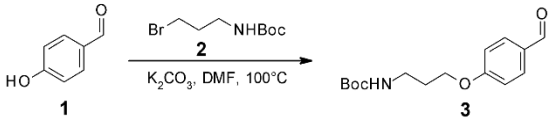

1 3

***tert*-Butyl (3-(4-formylphenoxy)propyl)carbamate (3)** A mixed solution of tert-butyl (3-bromopropyl)carbamate (2) (4.890 g, 20.5 mmol, 1.0 equiv), 4-hydroxybenzaldehyde (3.013 g, 24.6 mmol, 1.2 equiv), potassium carbonate (2.840 g, 20.5 mmol, 1.0 equiv), with DMF (30 mL) was stirred at ambient temperature for 4 h and allowed to heat at 100 °C for a further 30 min. Once the reaction was finished, the mixture was diluted with water and then methyl tert-butyl ether (MTBE) was used to extract the reaction product. The organic extract was washed sequentially with water (twice), 5% aqueous NaOH solution (twice), and again with water. The organic layer was subsequently dried (over anhydrous Na_2SO_4), filtered and reduced pressure concentrated. This residue was subsequently dried under vacuum to obtain compound 3, which was formed as a yellowish crystalline solid (4.684 g, 82%). ^{1}H NMR (500 MHz, $CDCl_3$): δ 1.43 (s, 9H), 1.93–2.07 (m, 2H), 3.27–3.42 (m, 2H), 4.09 (t, J = 6.01 Hz, 2H), 4.74–4.88 (m, 1H), 6.98 (d, J = 8.59 Hz, 2H), 7.82 (d, J = 8.59 Hz, 2H), 9.87 (s, 1H) ppm. ^{13}C NMR (126 MHz, $CDCl_3$): δ 28.3, 29.4, 37.7,

66.0, 79.3, 114.7, 129.9, 132.0, 156.0, 163.8, 190.8 ppm.

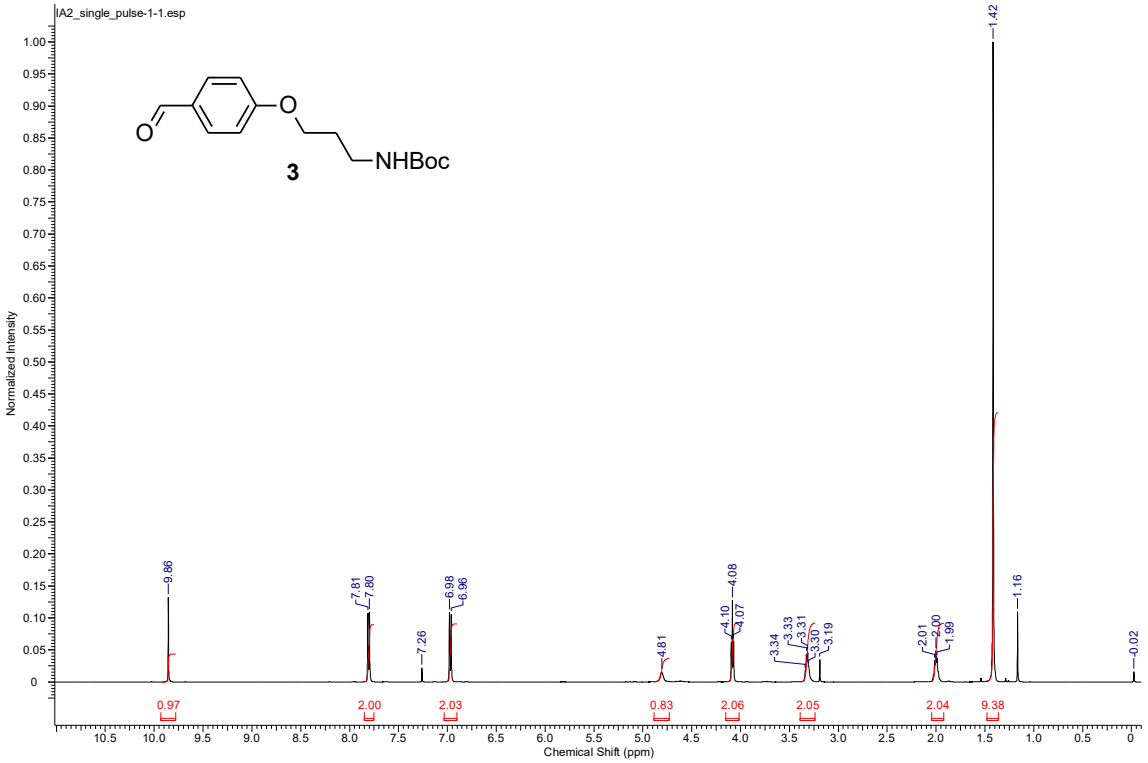

Figure 4.1. ^{1}H NMR spectra of compound **3**.

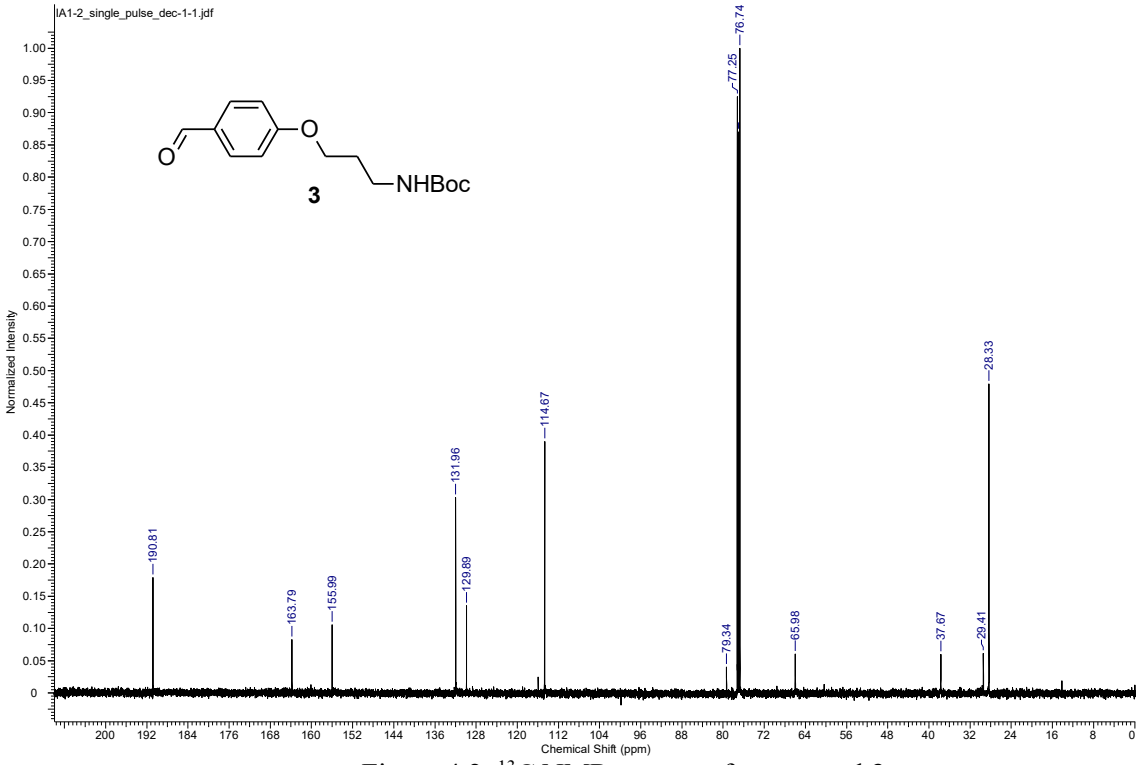

Figure 4.2. ^{13}C NMR spectra of compound **3.**

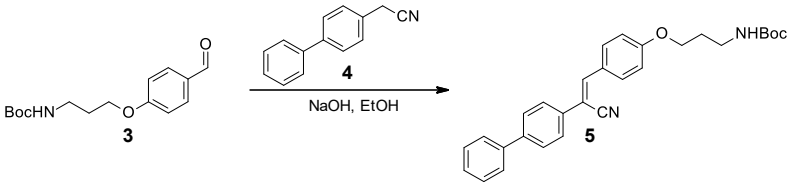

***tert*-Butyl(3-(4-(2-([1,1'-biphenyl]-4-yl)-2-cyanovinyl)phenoxy)propyl)carbamate (5).** Compound 3 (4.679 g, 16.7 mmol, 1.00 equiv), 2-([1,1′-biphenyl]-4-yl)acetonitrile (4) (3.403 g, 17.6 mmol, 1.05 equiv), and NaOH (1.00 g, 25.2 mmol, 1.5 equiv) were dissolved in ethanol (150 mL), and the resulting mixture was stirred at room temperature for 21 h.Upon completion, the formed precipitate was collected by filtration and washed successively with cold ethanol (twice) and diethyl ether (twice). The solid product was then dried to afford the target compound (7.103 g, 93%). ^{1}H NMR (500 MHz, $CDCl_3$): δ 1.46 (s, 9H), 1.99–2.08 (m, 2H), 3.36 (d, J = 6.30 Hz, 2H), 4.10 (t, J = 6.01 Hz, 2H), 6.99 (d, J = 8.59 Hz, 2H), 7.40 (d, J = 6.87 Hz, 1H), 7.48 (t, J = 7.45 Hz, 2H), 7.52 (s, 1H), 7.64 (d, J = 6.87 Hz, 2H), 7.66–7.77 (m, 4H), 7.91 (d, J = 8.59 Hz, 2H) ppm.

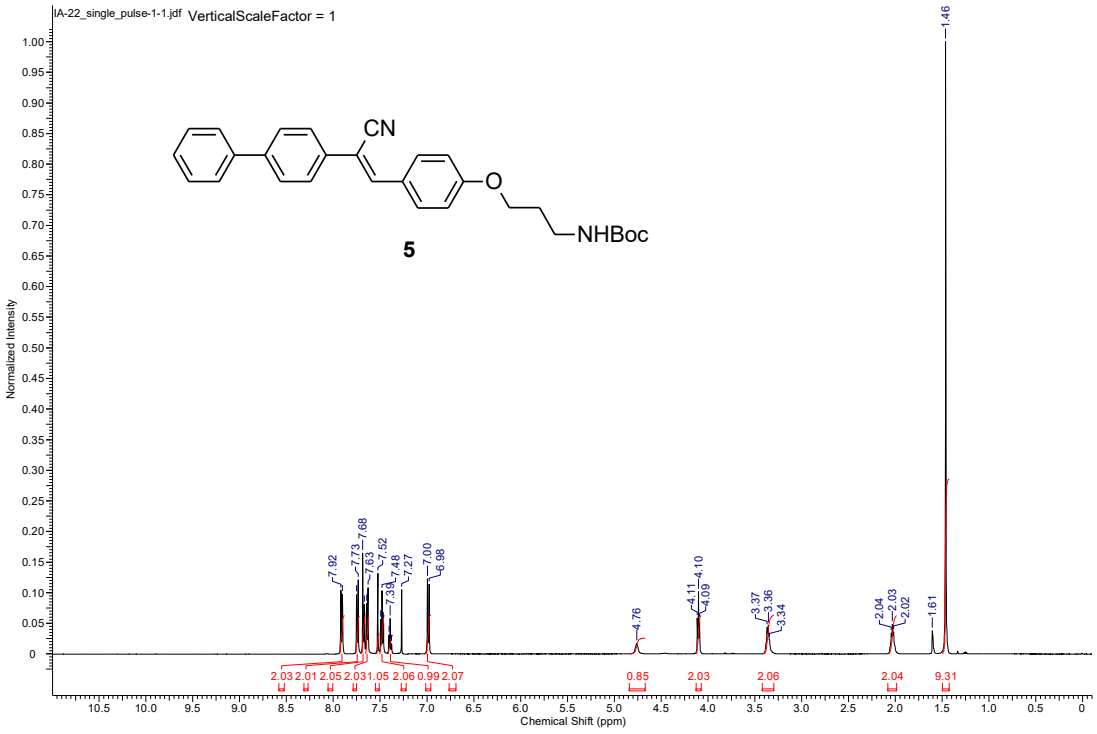

Figure 4.3. ^{1}H NMR spectra of compound **5.**

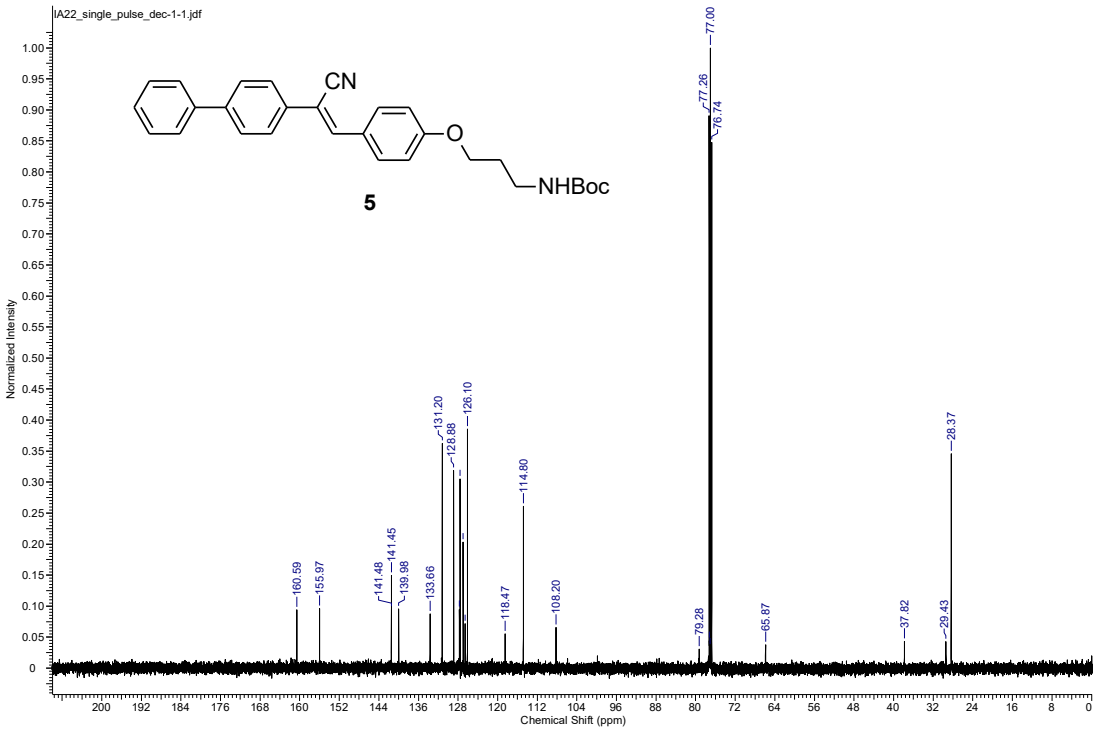

Figure 4.4. ^{13}C NMR spectra of compound **5.**

3-(4-(2-([1,1'-biphenyl]-4-yl)-2-cyanovinyl)phenoxy)propan-1-aminium 2,2,2-trifluoroacetate (BPCSA·TFA). Compound **5** (7.103 g, 15.6 mmol) was dissolved in dichloromethane (DCM, 50 mL), and trifluoroacetic acid (10 mL) was added to the solution. The reaction mixture was stirred at room temperature for 18 h. After completion, the solvent was removed under reduced pressure. The resulting solid was washed with diethyl ether, collected by filtration, and dried to obtain the product as a pale-yellow solid (7.341 g, quantitative yield). ^{1}H NMR (500 MHz, DMSO-d_6): δ 2.04 (quin, J = 6.69 Hz, 2H), 2.99 (br s, 2H), 4.16 (t, J = 6.09 Hz, 2H), 7.10–7.16 (m, 2H), 7.37–7.44 (m, 1H), 7.46–7.54 (m, 2H), 7.71–7.76 (m, 2H), 7.80–7.91 (m, 7H), 7.99 (d, J = 8.88 Hz, 2H), 8.05 (s, 4H) ppm. ^{13}C NMR (126 MHz, DMSO-d_6): δ 26.8, 36.3, 64.9, 106.8, 115.0, 118.4, 126.1, 126.5, 126.7, 127.3, 127.9, 129.1, 131.2, 133.2, 139.1, 140.4, 142.2, 158.4, 158.7, 160.3 ppm.

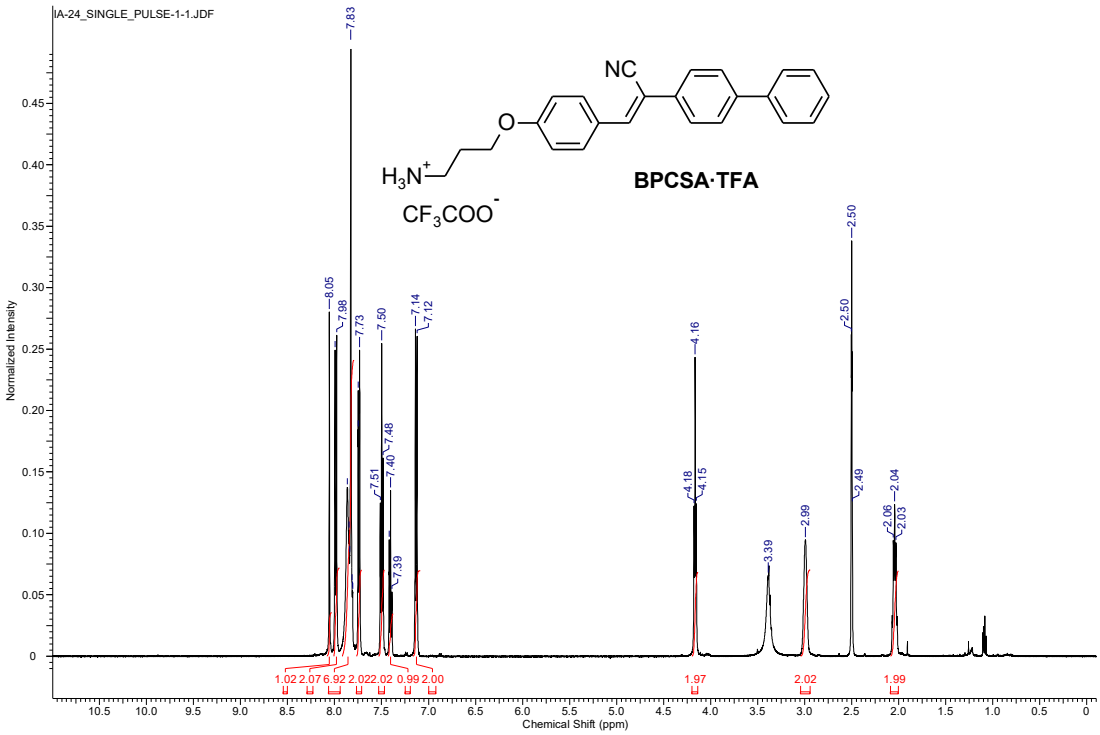

Figure 4.5. ^{1}H NMR spectra of compound BPCSA·TFA.

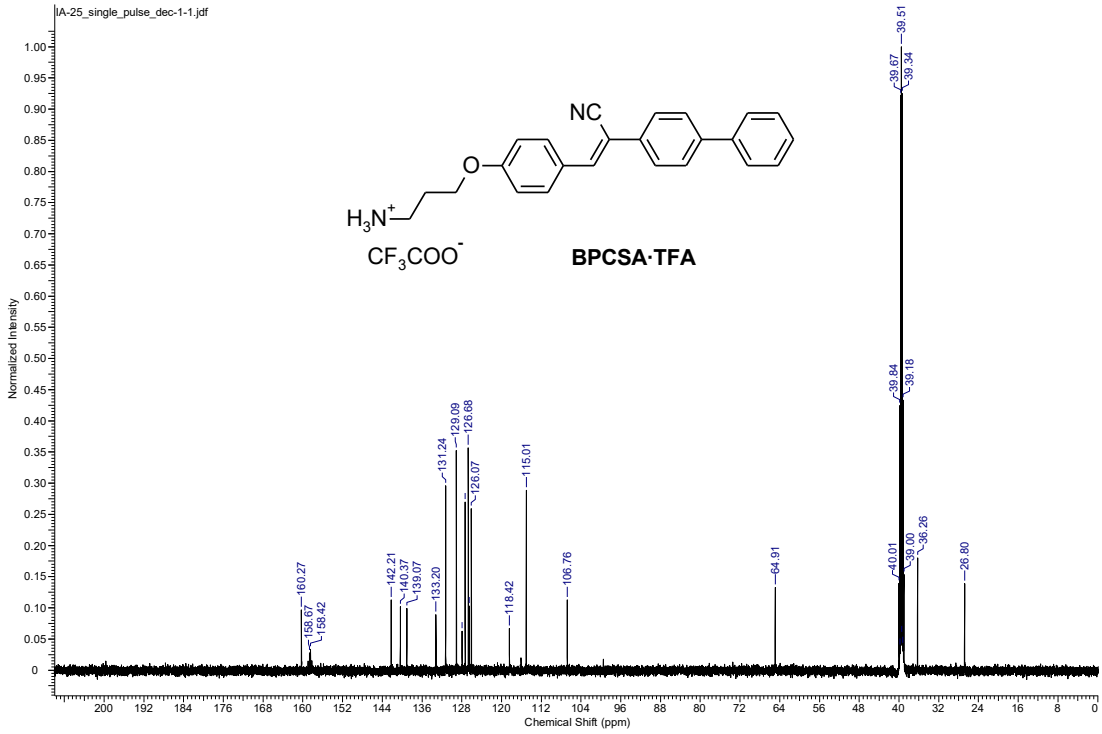

Figure 4.6. ^{13}C NMR spectra of compound BPCSA·TFA.

BPCSA (6). BPCSA·TFA (7.321 g, 15.6 mmol) was converted to its free base by suspending it in water (400 mL), followed by the addition of 5% aqueous sodium hydroxide solution (100 mL). The mixture was stirred vigorously for 15 min, after which the product was extracted with dichloromethane (DCM). The combined organic layers were dried over anhydrous Na_2SO_4, filtered, and concentrated under reduced pressure to yield the target compound as a pale-yellow solid (4.998 g, 90%). ^{1}H NMR (500 MHz, DMSO-d_6): δ 1.81 (quin, J = 6.59 Hz, 2H), 2.70 (t, J = 6.59 Hz, 2H), 4.13 (t, J = 6.30 Hz, 2H), 7.11 (d, J = 8.59 Hz, 2H), 7.36–7.44 (m, 1H), 7.50 (t, J = 7.73 Hz, 2H), 7.74 (d, J = 7.45 Hz, 2H), 7.82 (s, 4H), 7.97 (d, J = 8.59 Hz, 2H), 8.03 (s, 1H) ppm. ^{13}C NMR (126 MHz, DMSO-d_6): δ 32.6, 38.3, 65.9, 106.4, 115.0, 118.5, 126.0, 126.1, 126.7, 127.3, 127.9, 129.1, 131.3, 133.2, 139.1, 140.3, 142.3, 160.8 ppm.

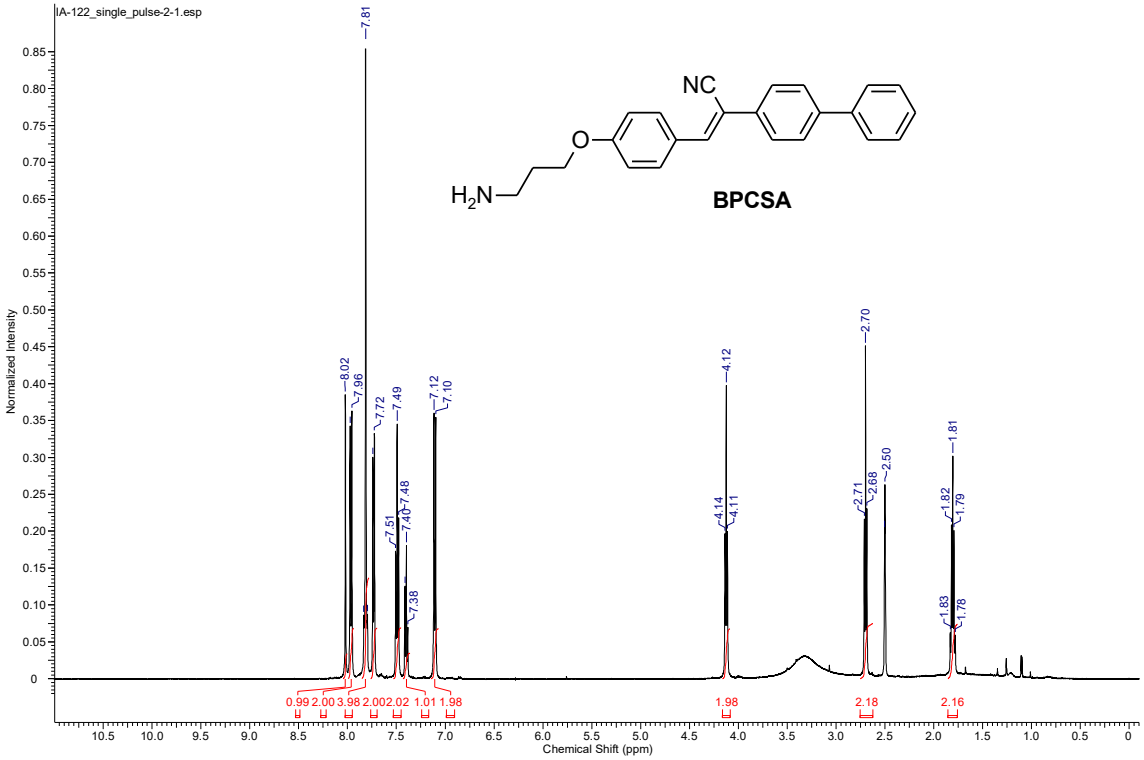

Figure 4.7. ^{1}H NMR spectra of compound BPCSA base.

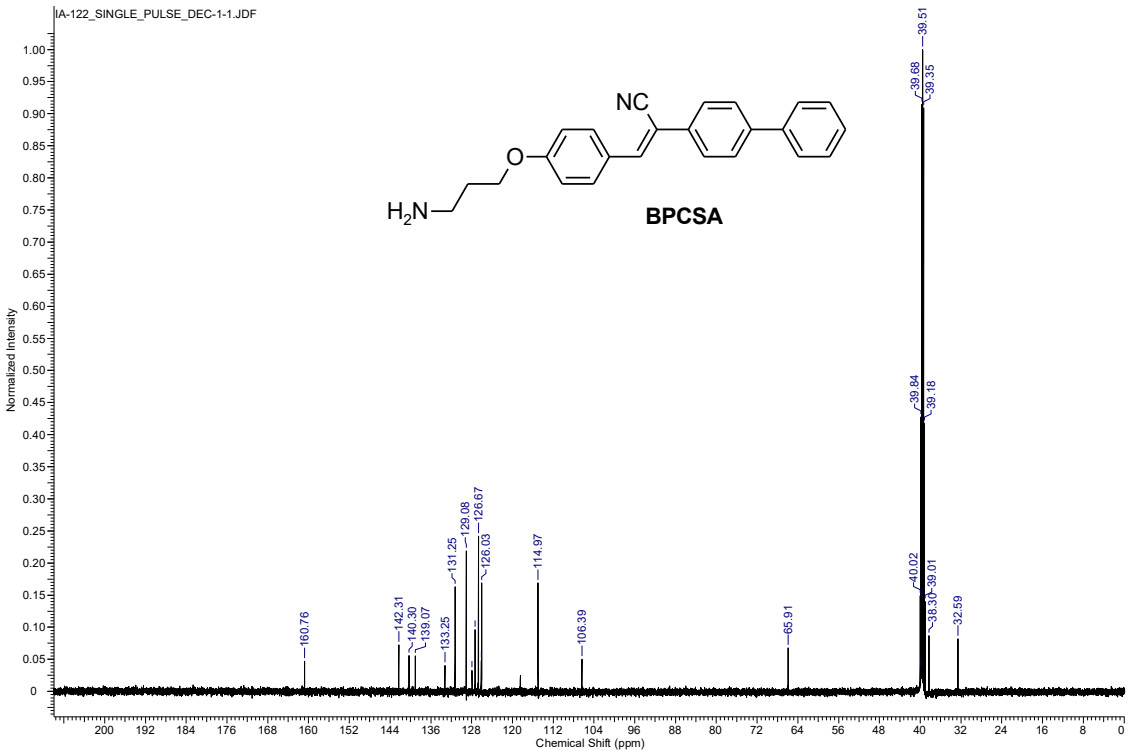

Figure 4.8. ^{13}C NMR spectra of compound BPCSA base.

Hydriodide salt **BPCSA·HI (6)** was prepared by dissolving free base BPCSA (0.893 g, 2.5 mmol) in 57% hydroiodic acid (10 mL) and stirring at room temperature for 3 h. The resulting solid was then isolated with centrifugation and washed three times with water. It was then dissolved in acetonitrile and the solvent was withdrawn under low pressure to free any remaining moisture and provide a high yield product (1.141 g, 95%). ^{1}H NMR (500 MHz, DMSO-d_6): δ 8.06 (s, 1H), 7.99 (d, J = 9.0 Hz, 2H), 7.83 (s, 4H), 7.74 (d, J = 7.3 Hz, 2H), 7.50 (t, J = 7.7 Hz, 2H), 7.43–7.38 (m, 1H), 7.13 (d, J = 8.9 Hz, 2H), 4.16 (t, J = 6.0 Hz, 2H), 2.96 (t, J = 7.3 Hz, 2H), 2.02 (quin, J = 6.7 Hz, 2H) ppm. ^{13}C NMR (126 MHz, DMSO-d_6): δ 27.5, 36.9, 65.4, 107.2, 115.4, 115.6, 118.9, 126.6, 127.0, 127.2, 127.8, 129.6, 131.7, 133.7, 139.5, 140.9, 142.8, 160.7 ppm.

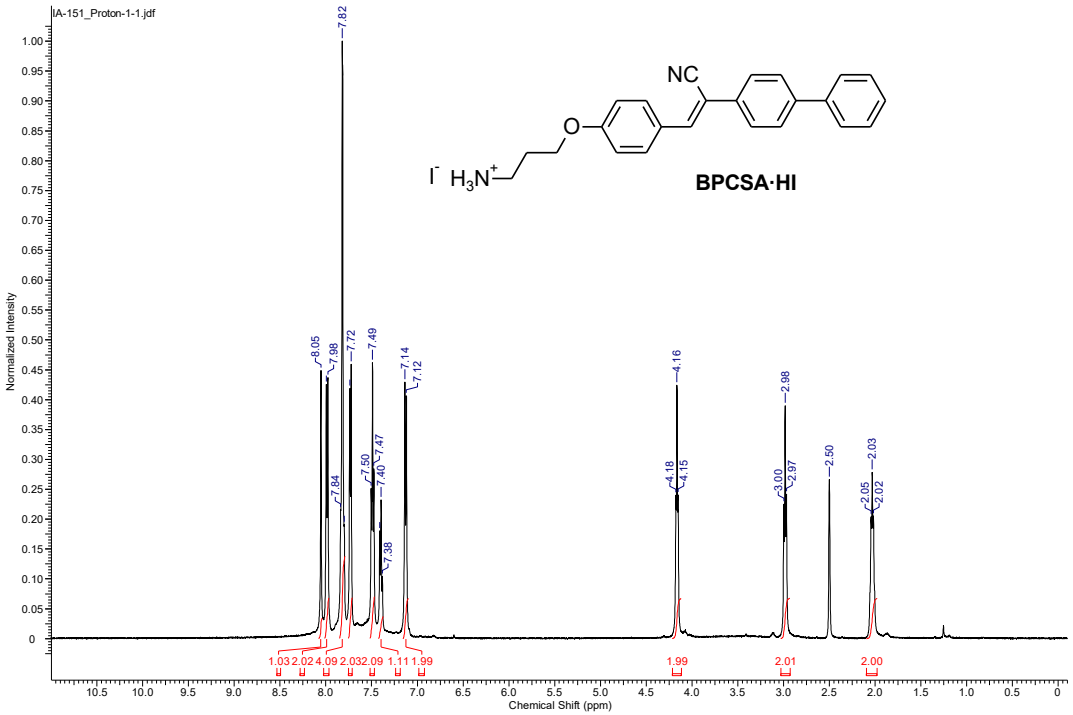

Figure 4.9. ^{1}H NMR spectra of compound **6**.

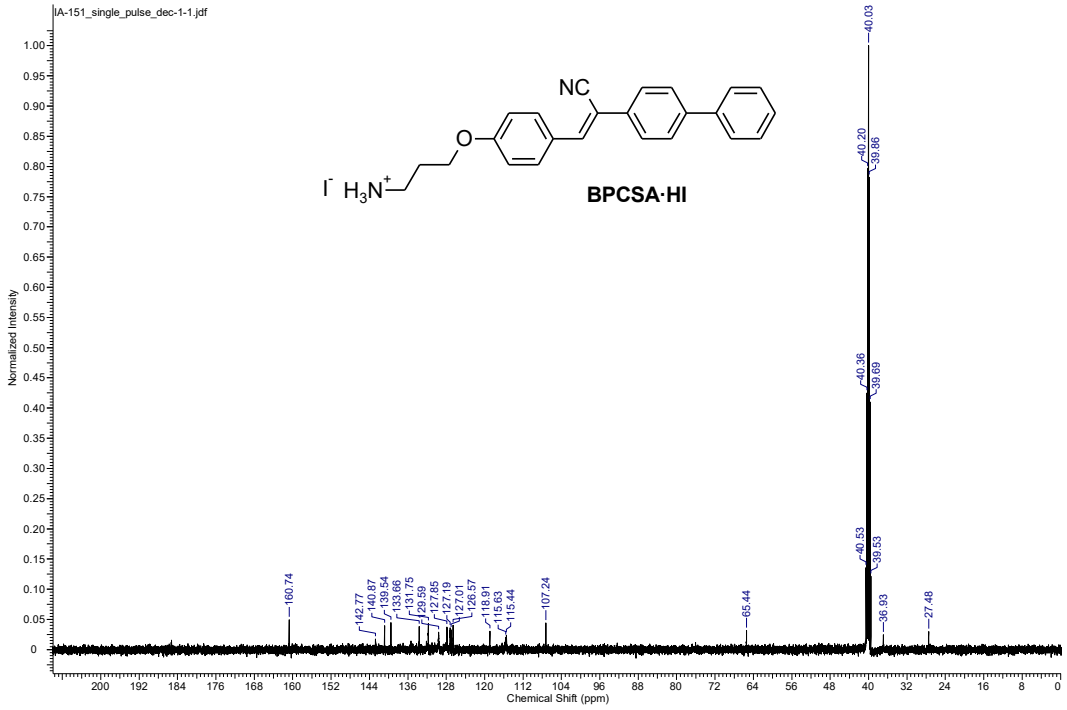

Figure 4.10. ^{13}C NMR spectra of compound **6**.

4.2.2 Synthesis of FPCSA

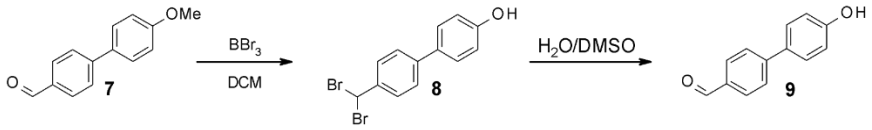

4'-Hydroxy-[1,1'-biphenyl]-4-carbaldehyde (9). A solution of aldehyde 7 (5.052 g, 23.6 mmol, 1.0 equiv) in dichloromethane (40 mL) was placed under an argon atmosphere, and boron tribromide (6.7 mL, 70.7 mmol, 3.0 equiv) was added dropwise. The reaction mixture was stirred at room temperature for 4 h.

Upon completion, the mixture was carefully quenched by pouring into an ice–water bath and stirred for an additional 15 min. The organic phase was then separated by extraction with dichloromethane. The combined extracts were washed with aqueous sodium bicarbonate solution (three times) followed by water (twice), dried over anhydrous Na_2SO_4, filtered, and concentrated under reduced pressure to yield crude intermediate 8, which was used directly in the next step without further purification.

Intermediate 8 was subsequently dissolved in a DMSO/H_2O mixture (56 mL / 10 mL), and the solution was stirred at room temperature overnight. The reaction mixture was then diluted with water and extracted with ethyl acetate. The combined organic layers were washed with water (three times), dried over Na_2SO_4, filtered, and concentrated under reduced pressure. The resulting residue was further dried under vacuum to afford compound 9 as the final product (7.620 g, 89%).

^{1}H NMR (500 MHz, DMSO-d_6): δ 6.89 (d, J = 9.17 Hz, 2H), 7.63 (d, J = 8.02 Hz, 2H), 7.82 (s, 2H), 7.94 (s, 2H), 9.80 (s, 1H), 10.01 (s, 1H) ppm. ^{13}C NMR (126 MHz, DMSO-d_6): δ

116.0, 126.4, 128.4, 129.3, 130.2, 134.2, 146.0, 158.3, 192.6 ppm.

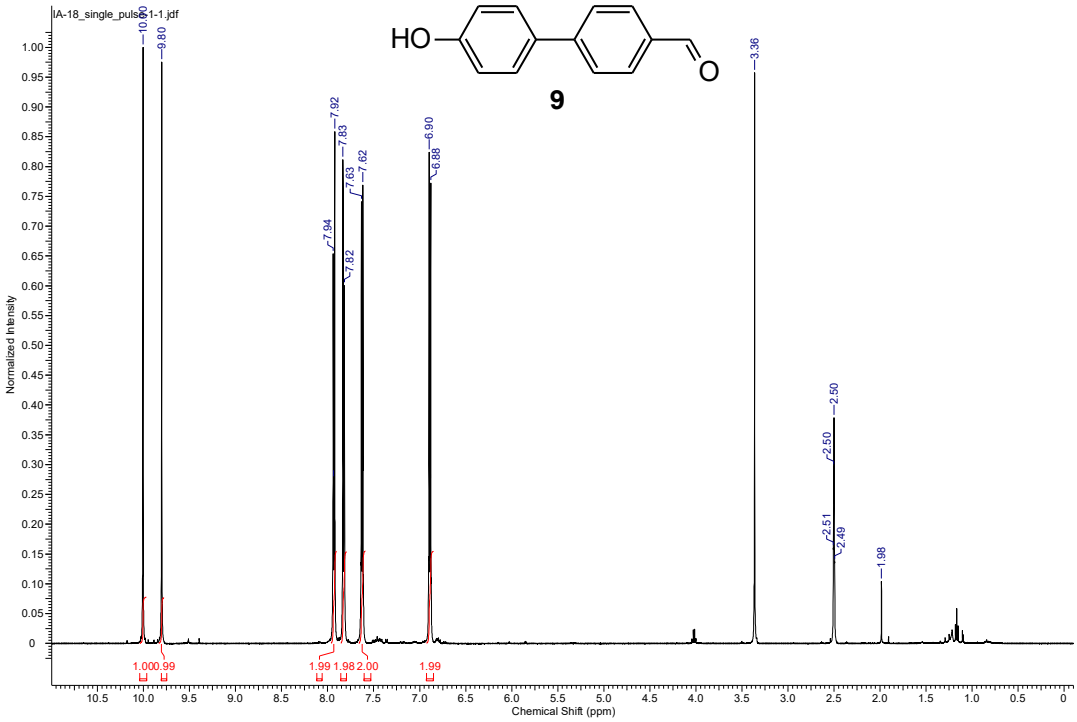

Figure 4.11. [1]H NMR spectra of compound **9**.

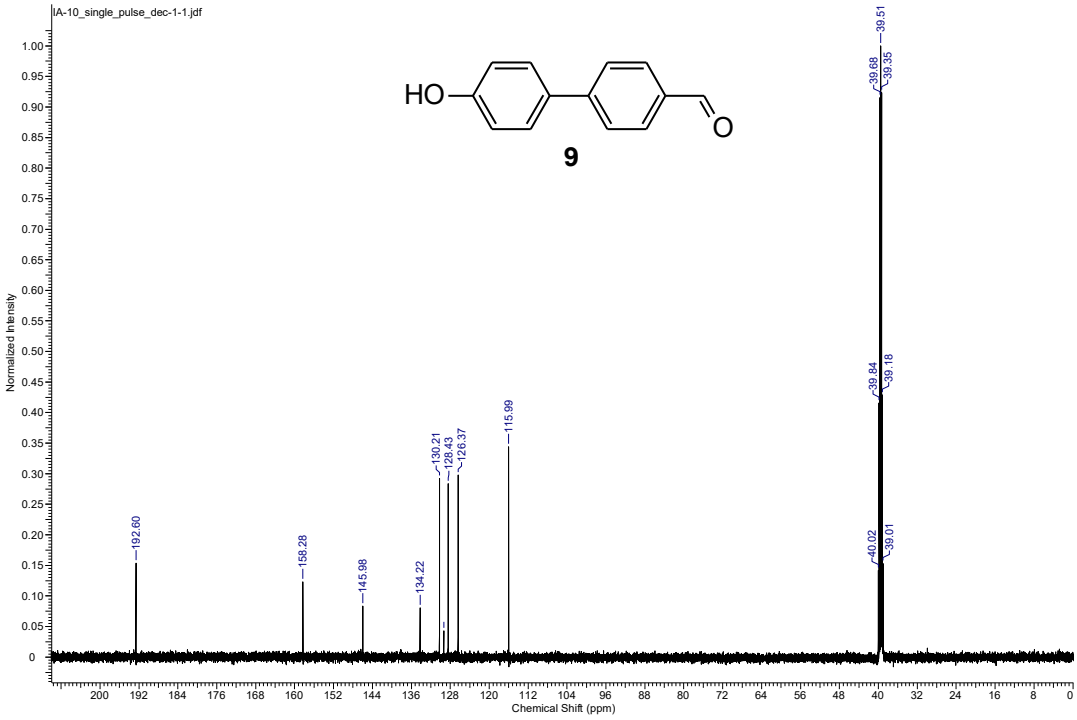

Figure 4.12. [13]C NMR spectra of compound **9**.

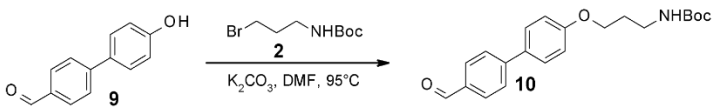

***tert*-Butyl (3-((4'-formyl-[1,1'-biphenyl]-4-yl)oxy)propyl)carbamate (10).** A mixture of 3-(Boc-amino)propyl bromide (2) (4.933 g, 20.7 mmol, 0.98 equiv), compound 9 (4.191 g, 21.1 mmol, 1.00 equiv), and potassium carbonate (8.775 g, 63.5 mmol, 3.00 equiv) was dissolved in DMF (52 mL) and stirred at 95 °C for 23 h. After completion, the reaction mixture was allowed to cool to room temperature, diluted with water, and extracted with methyl tert-butyl ether (MTBE). The combined organic extracts were washed sequentially with water, 5% aqueous NaOH solution, and again with water. The organic phase was dried over anhydrous Na_2SO_4, filtered, and concentrated under reduced pressure. The resulting residue was further dried under vacuum to afford compound 10 as a pure product (6.769 g, 90%). ^{1}H NMR (500 MHz, $CDCl_3$): δ 1.46 (s, 9H), 1.98–2.07 (m, 2H), 3.36 (q, J = 5.70 Hz, 2H), 4.09 (t, J = 5.73 Hz, 2H), 4.79 (br s, 1H), 7.00 (d, J = 8.59 Hz, 2H), 7.57–7.62 (m, 2H), 7.72 (d, J = 8.02 Hz, 2H), 7.93 (d, J = 8.02 Hz, 2H), 10.04 (s, 1H) ppm.

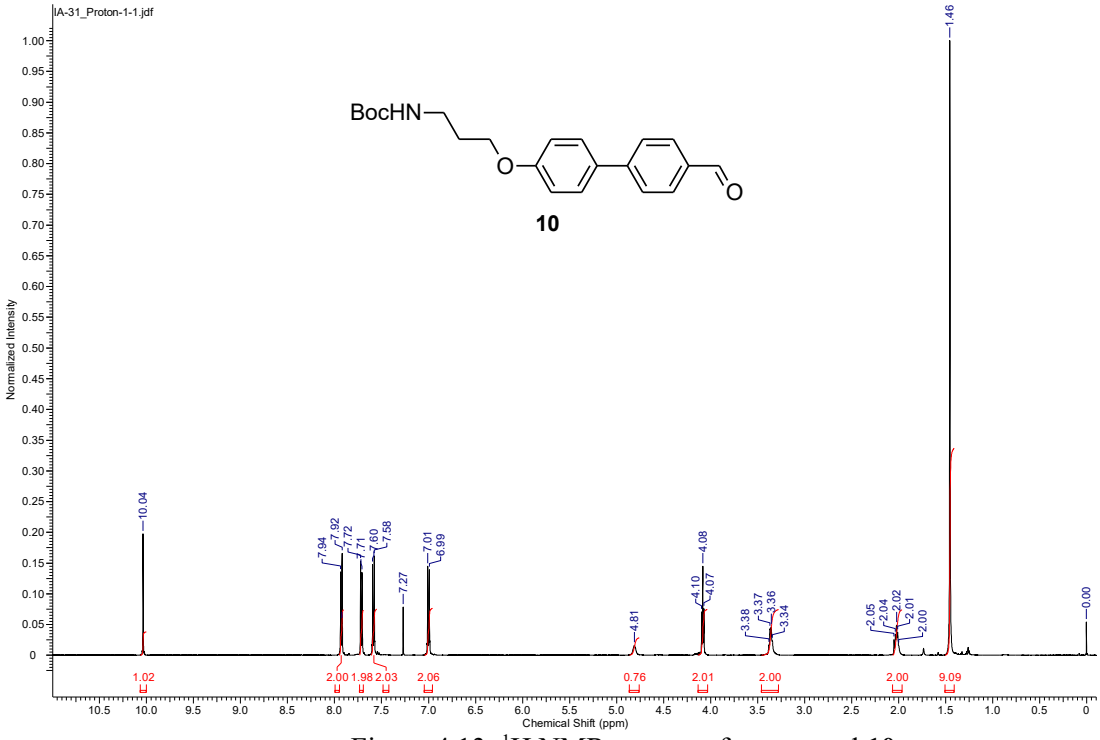

Figure 4.13. ^{1}H NMR spectra of compound **10**.

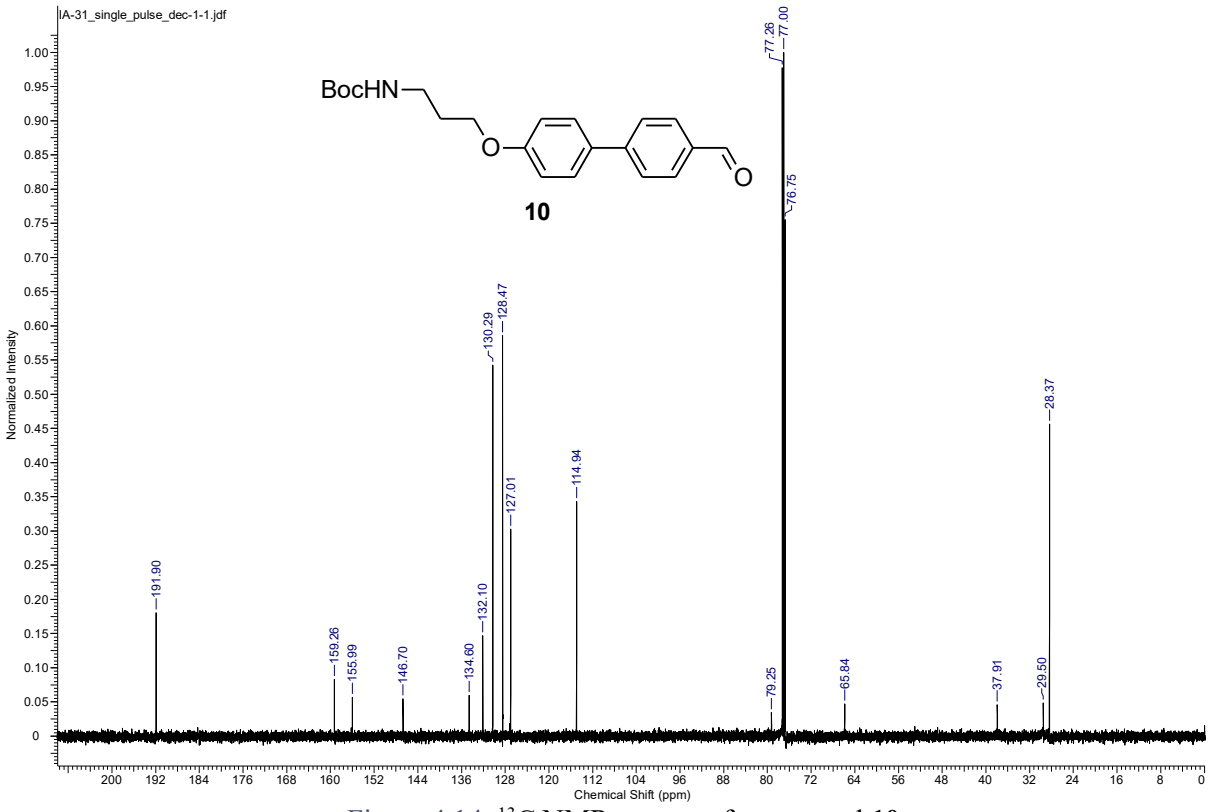

Figure 4.14. ^{13}C NMR spectra of compound **10**.

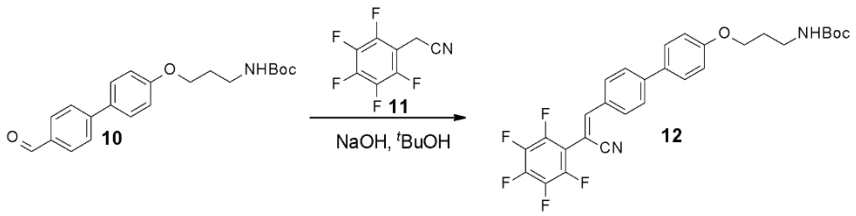

***tert*-Butyl (3-((4'-(2-cyano-2-(perfluorophenyl)vinyl)-[1,1'-biphenyl]-4-yl)oxy)propyl)carbamate (12).** Compound 10 (5.680 g, 16.0 mmol, 1.00 equiv), pentafluorophenylacetonitrile (**11**) (3.475 g, 16.78 mmol, 1.05 equiv), and NaOH (2.006 g, 47.9 mmol, 3.00 equiv) were mixed in tert-butanol (70 mL), and the reaction mixture was stirred at room temperature for 25 h. The resulting mixture was subsequently diluted with water and extracted with methyl tert-butyl ether (MTBE). The combined organic layers were rinsed with water, dried over anhydrous Na_2SO_4, filtered, and concentrated under reduced pressure. The resulting residue was redissolved in dichloromethane (DCM), and the product precipitated by the addition of hexane. The solid was collected by filtration, washed with diethyl ether, and dried to

afford the desired compound (6.208 g, 71%). ^{1}H NMR (500 MHz, DMSO-d$_6$): δ 1.38 (s, 9H), 1.85 (quin, J = 6.60 Hz, 2H), 3.10 (q, J = 6.60 Hz, 2H), 4.04 (t, J = 6.23 Hz, 2H), 6.94 (t, J = 5.58 Hz, 1H), 7.05 (d, J = 8.74 Hz, 2H), 7.75 (d, J = 8.73 Hz, 2H), 7.87–7.91 (m, 3H), 8.03 (d, J = 8.45 Hz, 2H) ppm. ^{13}C NMR (126 MHz, DMSO-d$_6$): δ 28.8, 29.7, 37.4, 65.9, 78.0, 93.7, 115.6, 116.9, 127.2, 128.6, 130.8, 131.0, 131.3, 143.8, 153.0, 156.2, 159.6 ppm.

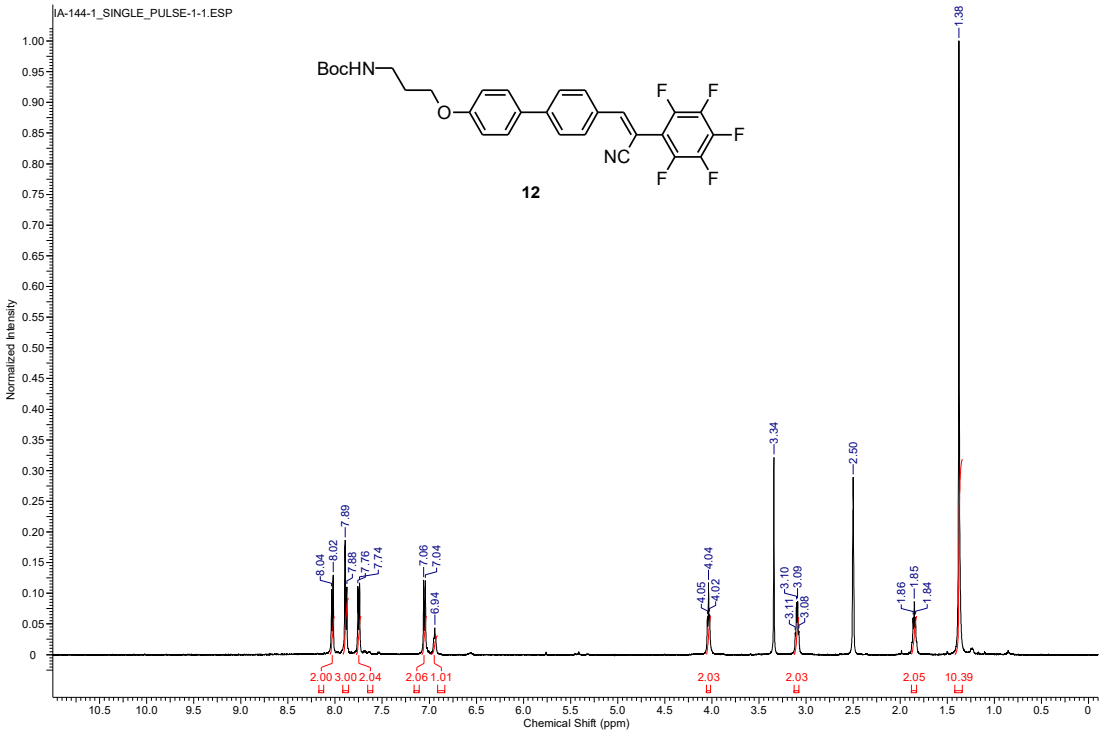

Figure 4.15. ^{1}H NMR spectra of compound **12**.

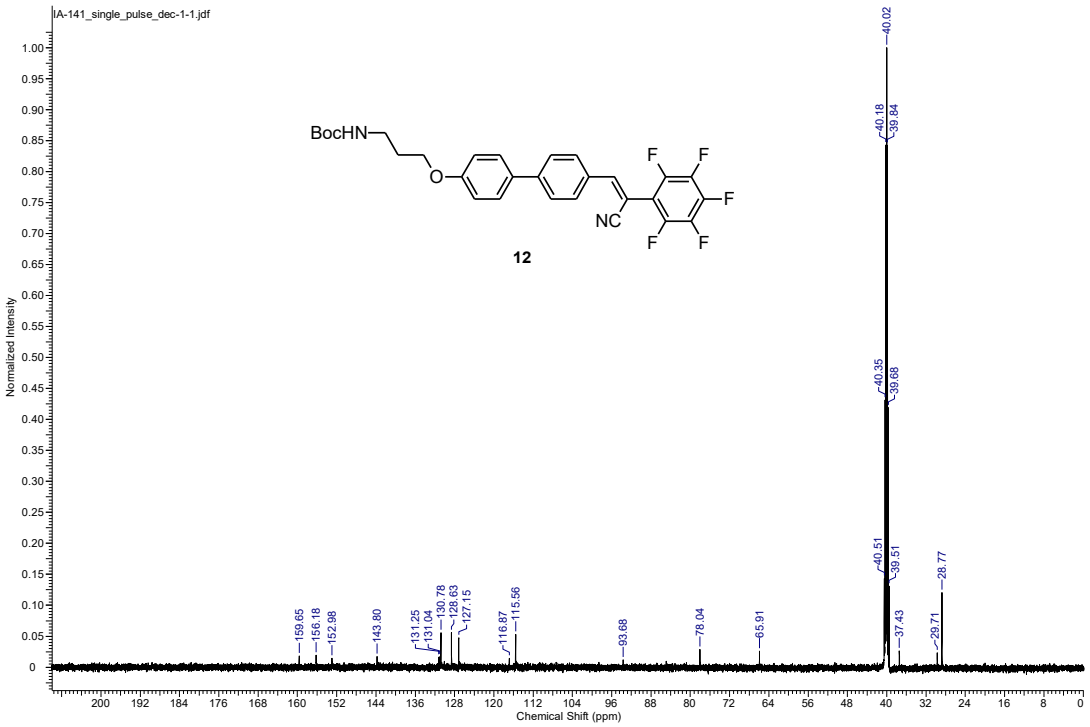

Figure 4.16. ^{13}C NMR spectra of compound **12**.

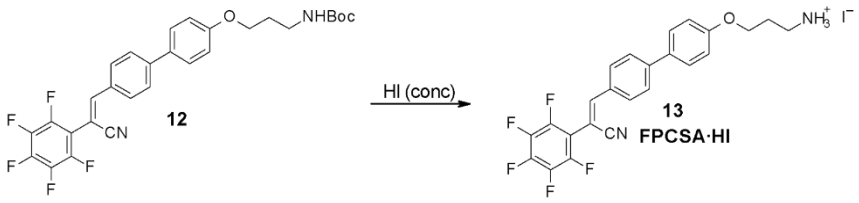

FPCSA·HI (**13**) Compound 12 (2.008 g, 3.69 mmol) was suspended in 57% aqueous hydroiodic acid (20 mL), and the mixture was stirred at room temperature for 4 h.

The resulting precipitate was isolated by centrifugation and washed three times with water. The wet solid was then dissolved in acetonitrile, and the solvent was removed under reduced pressure. The residue was further dried under vacuum to afford the final product (2.049 g, 97%). ^{1}H NMR (500 MHz, DMSO-d$_6$): δ 2.04 (quin, J = 6.80 Hz, 2H), 3.00 (sxt, J = 6.20 Hz, 2H), 4.14 (t, J = 6.01 Hz, 2H), 7.08 (d, J = 8.88 Hz, 2H), 7.67–7.75 (m, 3H), 7.75–7.80 (m, 2H), 7.88 (s, 1H), 7.88–8.07 (m, 4H) ppm. ^{13}C NMR (126 MHz, DMSO-d$_6$): δ 26.8, 36.4, 64.7, 93.2, 115.1, 116.3, 126.7, 128.2, 130.3, 130.6, 131.0, 143.2, 152.5, 158.8 ppm.

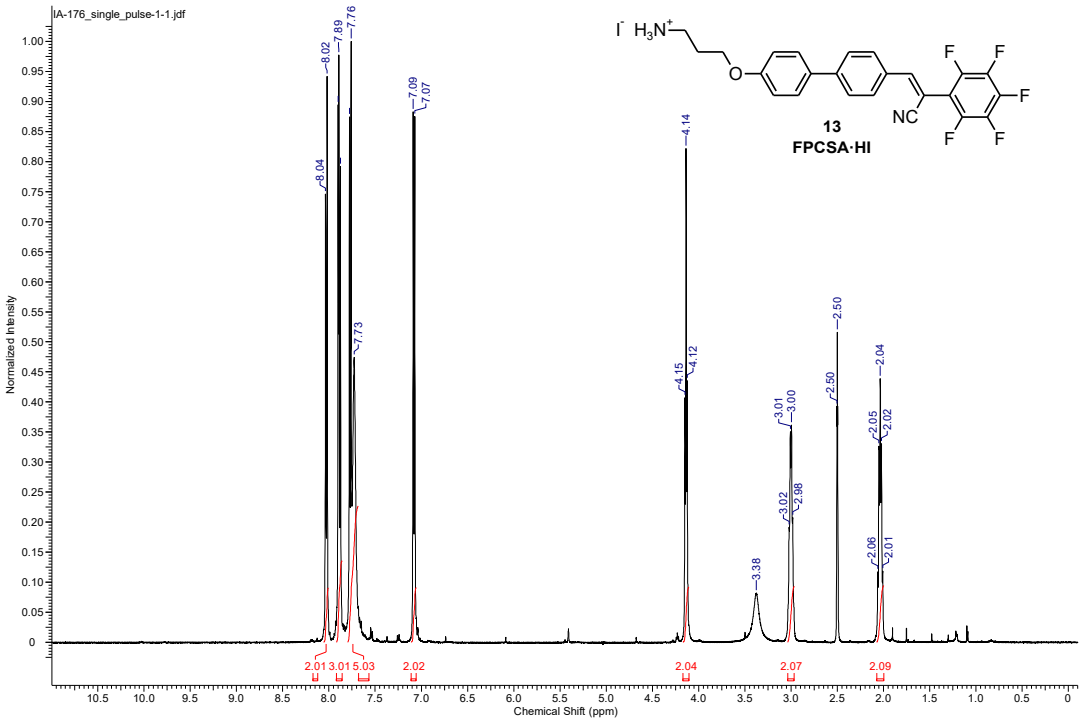

Figure 4.17. ^{1}H NMR spectra of compound **13**.

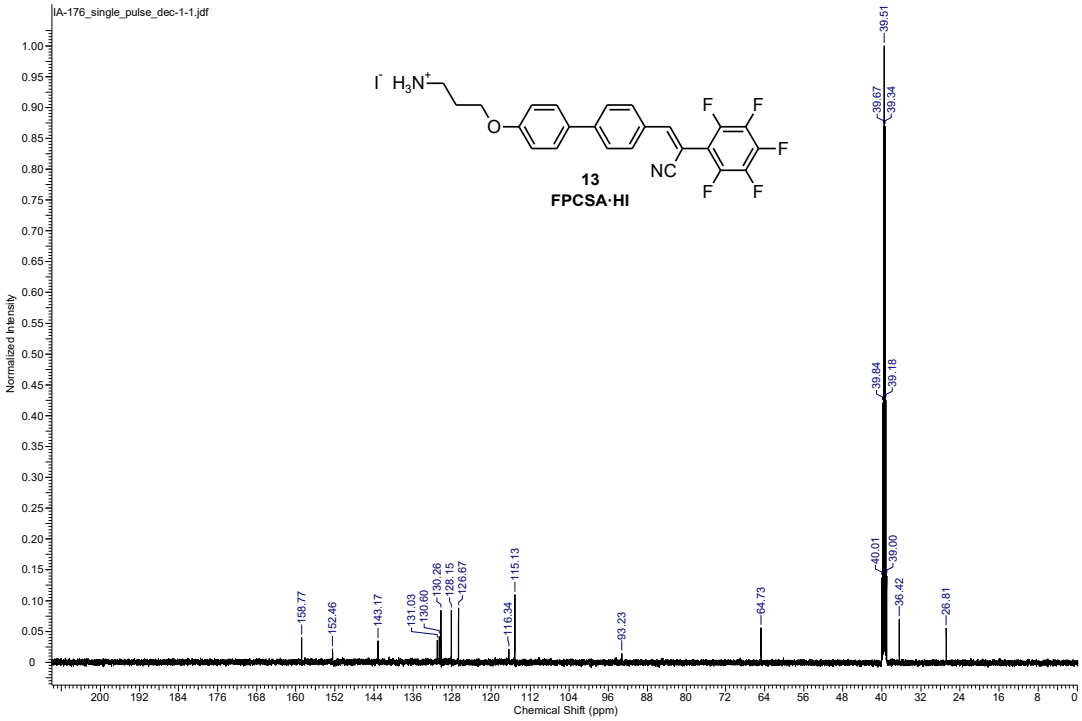

Figure 4.18. ^{13}C NMR spectra of compound **13**.

4.3.Structural and optical characterization

The synthesized AIE LPs display markedly different PL behavior in the solid state compared to solution, which is characteristic of aggregation-induced emission enhancement (AIEE). In diluted DMSO solution, the molecules remain largely isolated and undergo non-radiative relaxation pathways due to intramolecular motions, such as torsional rotation around phenyl rings. In contrast, when aggregated in the powder form, these non-radiative pathways are significantly restricted by intermolecular packing. As a result, radiative recombination is promoted, leading to strong fluorescence emission. This AIEE phenomenon is clearly observed in Figures 4.19A and 4.19C, where the PL intensity in powder form is substantially stronger than in solution.

The fluorine-substituted derivative, FPCSA, is reported as having the λ_{max} at 478 nm in solid form (see Figure 4.19D). In comparison to its non-fluorinated counterpart, BPCSA, which emits at 435 nm (see Figure 4.19B), this emission is red-shifted. Spectral variation can be explained by the electronic influence of fluorine substitution (Donor–π–acceptor [D–π–A]) at the structural level. The methoxy group (–OCH_3) acts as an electron donor and the cyano (–CN) and fluorine substituents act as electron-withdrawing groups. Because of its superior electronegativity, this particular fluorine stabilizes the LUMO with respect to electrons, resulting in a fall in the total bandgap of the molecule. The subsequent stabilization of the polarized LUMO explains the apparent bathochromic (red) shifting of emission. Curiously, both LP powders have red-biased photoluminescence excitation (PLE) spectra compared to their absorption spectra obtained in DMSO solution. In this way, the emission of solids is not only the result of a single phase of the molecule transition, but also the result of structural reorganization and intermolecular interaction after aggregation. The red-shift can be attributed to enhanced molecular planarization in the aggregated state which promotes conjugation along the π-backbone and is more conducive to

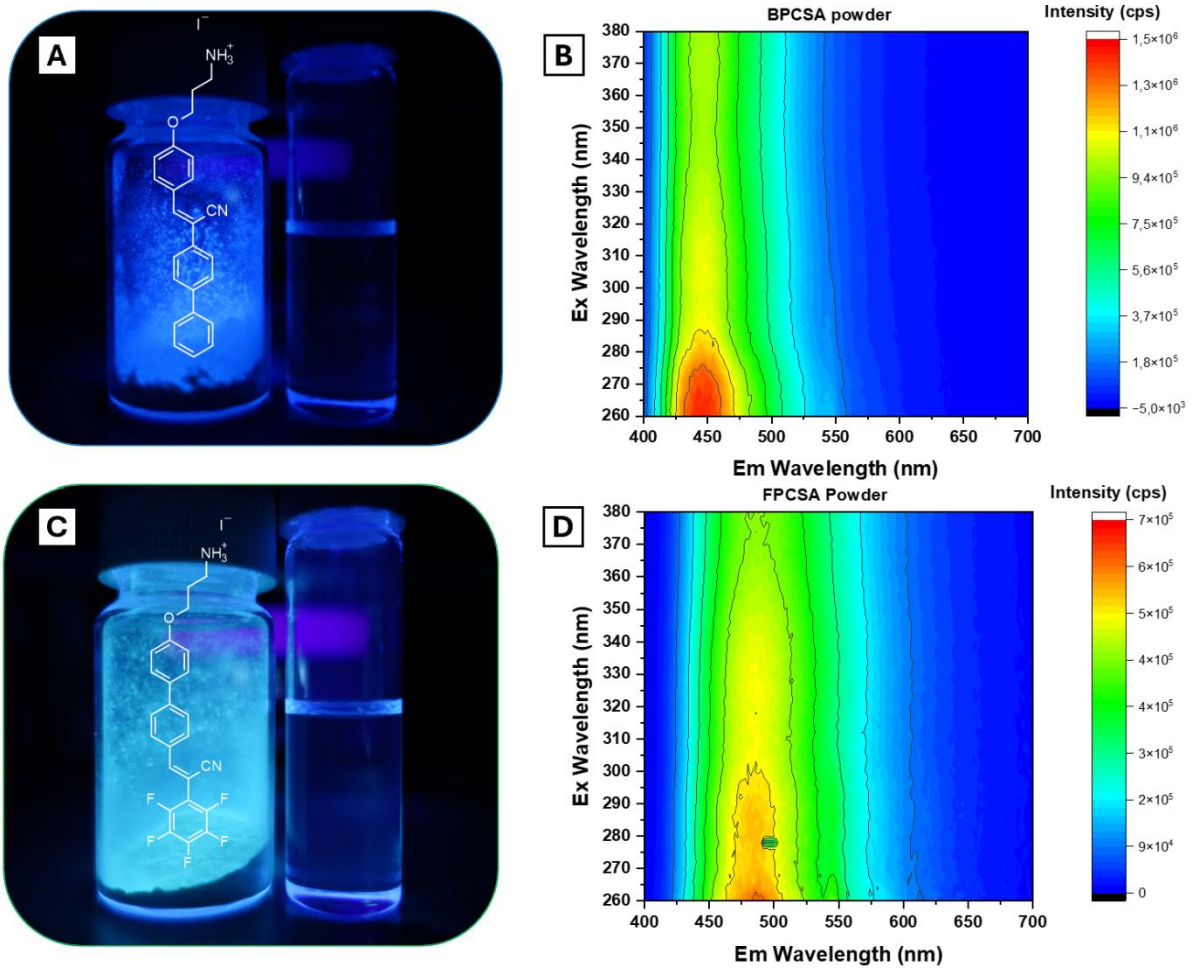

Figure 4.19. (A) and (C) – photographs of BPCSA and FPCSA, respectively in solution and powder form; (B) and (D) – excitation dependent PL emission color plot of BPCSA and FPCSA powders

delocalization of excitons. Additionally, the alignment of molecular dipoles in solid state can lead to stabilized excited states which result in further shift of emission to lower energies.

A reasonable explanation for this phenomenon is the solid state formation of J-aggregates [141, 143]. A typical J-aggregation consists of a head-to-tail molecular stacking that may produce red-shifted and narrow-band emission caused, to some extent, by exciton delocalization in the aggregate. The spectral features in the LP powders are consistent with these types of aggregation-induced effects, and thus imply that the molecules form proper packing arrangements that stabilize their emissive states. Besides J-aggregation, π–π stacking and dipole–dipole coupling might play a role in the red-shifts and the increased emission intensity [144]. These results are in line with the previously reported performances of cyanostilbene-based AIE systems that incorporate strong electron-withdrawing groups for efficient intramolecular charge transfer conversion and for the

generation of solid-state emission. For example, AIE frameworks incorporating fluorine have been extensively reported to exhibit lower bandgaps and increased AIEE activity because they modulate frontier orbital energies while positively promoting ordered packing in the solid state [142, 145]. The large difference of BPCSA and FPCSA in our results emphasizes the important influence of focused molecular design on the photophysical characteristics thus confirming the fluorine substitution strategy to be an effective means for tuning the emission behaviour of AIE cations to be used in 2D PVSK systems. Both BPCSA and FPCSA can be seen with equal absorption maximum centered at 3.54 eV in DMSO (see Figure 4.20A and 4.20B), demonstrating their π–π* electronic transition in the molecularly dispersed state when dissolved in DMSO. Such characteristics are common for isolated chromophores in a good solvent in which intermolecular interactions are rare. When also using thin films of these molecules as the substrate on glass, the absorption spectra have a remarkable change, where the single peak splits sharply into two bands, 3.8 eV and 3.2 eV. This splitting strongly suggests that there are multiple aggregation states present in the solid film. More precisely, this implies that the molecules crystallize into 2 or more packing motifs and create unique excitonic coupling environments. The higher-energy peak at 3.8 eV can be explained by H-type aggregation where face-to-face molecular stacking results in a blue-shifted absorption band because of strong excitonic repulsion. In contrast, the lower-energy band at 3.2 eV is due to J-type aggregation in which head-to-tail packing promotes a stable excitonic state, which leads to red-shifted absorption. It is not surprising that both heterogeneous H- and J-aggregation exist in such films, because polymorphic crystallization and local disorder usually result in inconsistent packing modes of AIE-active molecules. Such a dual structure of aggregation behavior implies a substantial photophysical landscape offering multiple optical transitions, which need to be utilized by tunable device applications. PL spectra presented in Figures 4.20C and 4.20D provide additional evidence for these aggregation effects. The films instead exhibit two or three peaks each at about 350 nm, 450 nm, and 750 nm, respectively, and their intensities are affected by the excitation wavelength. The short-wavelength emission wavelengths (~350 nm and ~450 nm) match with fluorescence of singlet excitons derived from various aggregated chromophore states. Emissions at ~350 nm are generally related to less-conjugated or more twisted chemical arrangements, while the ~450 nm band corresponds to planarized and better conjugated packing domains. The extremely broad red emission at ~750 nm, on the other hand, is a substantially new emissive phenomenon, it is located well below singlet emission energy and is accompanied by an

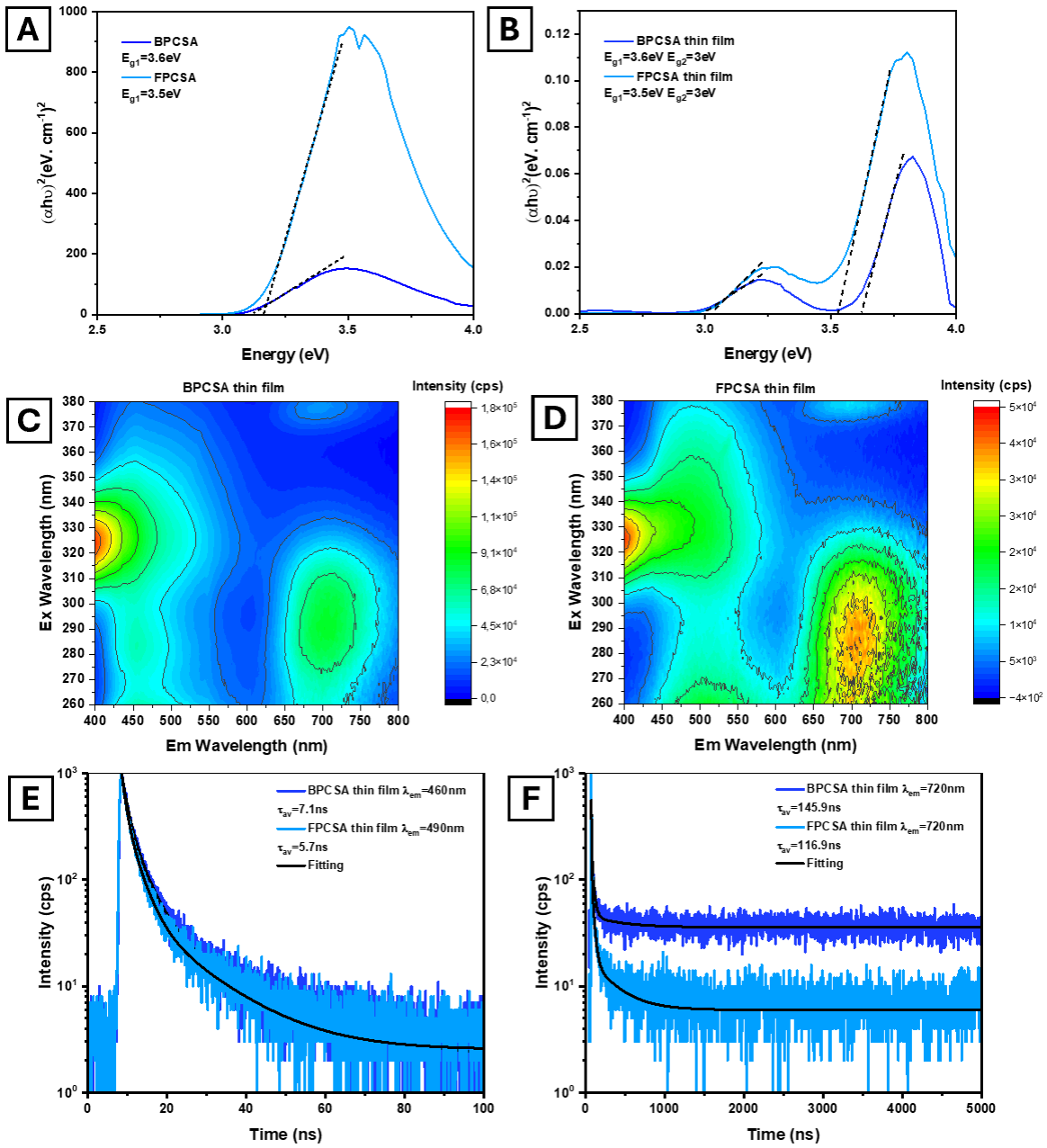

Figure 4.20. (A,B) – tauc plots; (C,D) excitation dependent PL emission, (E,F) TRPL of BPCSA and FPCSA thin films, respectively.

extremely long decay lifetime. PL studies found value in time resolution support this conclusion. The green emission band (centered near 450 nm) exhibited relatively short lifetimes of 7.1 ns for BPCSA and 5.7 ns for FPCSA thin films (see Figures 4.20E and 4.20F). These data are generally expected of prompt fluorescence and are in good agreement with radiative decay on the basis of singlet excited states. Red emission, by contrast, presents a much longer lifetime: 145.9 ns for BPCSA and 116.9 ns for FPCSA. The average values given are two orders of magnitude larger

than the singlet fluorescence lifetimes, thus the red emission is presumably derived from phosphorescence of triplet excitons.

This triplet emission could arise due to effective intersystem crossing (ISC) enabled by the molecular structure of the AIEE dyes. Strong electron-withdrawing substituents (e.g., fluorine and cyano groups) increase spin–orbit coupling through orbital mixing, thus favoring ISC from singlet to triplet states. The triplet excitons experience radiative decay once populated, leading to the long-lived red emission seen in the thin films [146]. This is particularly pertinent because organic molecules without heavy atoms exhibit extremely low phosphorescence at room temperature. The red phosphorescence found in these AIEE molecules imply that molecular packing and interaction between molecules in the solid state provide a rigid environment that inhibits non-radiative triplet quenching, leading to phosphorescence stability. The coexistence of multiple fluorescence bands and long-lived phosphorescence in thin films of BPCSA and FPCSA is consistent with wide degree of photophysical diversity that can be reached from molecular aggregation. Also significant, fluorinated FPCSA showed reduced triplet lifetimes versus BPCSA, which could perhaps reflect faster ISC efficiency and accelerated radiative decay owing to the more electron-withdrawing nature of fluorine. In terms of PVSK hybridity, this dual fluorescence–phosphorescence characteristic is very pertinent. The dual presence of singlet and triplet emissive channels in AIE LPs could offer various means to transfer energy to the PVSK lattice, and thus can potentially improve exciton harvesting and enhance the hybrid material emission spectrum. Furthermore, the red-shifted phosphorescence may favor the band edge at lead-halide PVSKs, enabling charge transfer or triplet sensitization. Hence, the photophysical properties of BPCSA plus FPCSA confirm not only that there are basic aggregation-driven processes, but they also hold great promise for adjusting exciton dynamics in AIE–PVSK optoelectronic systems.

CHAPTER 5: ASSEMBLY AND STUDY OF AGGREGATION INDUCED EMISSION ORGANIC CATION INCORPORATED 2D AND QUASI-2D PVSKS

5.1. Introduction

This chapter presents the mechanisms for combining AIE organic cations for 2D and quasi-2D PVSK structures. Inspired by Chapter 4 on molecular design and photophysical properties of AIE luminophores, we highlight in this section the process of adding these cations to a PVSK lattice and their effect on the formation, structure, morphology, and optoelectronic properties of the materials that emerge. One approach to overcome the shortcomings of traditional organic ligands is to incorporate conjugated organic cations into layered PVSKs as these will overcome the issue of photoluminescence quenching (due to strong intermolecular interactions). AIE-active molecules, on the other hand, shine much brighter when they are aggregated than conventional luminophores, due to their internal motion being restricted and are more appropriate for PVSK quantum-well structures. To establish hybrid structure according to the formula $(AIE)_2MA_{n-1}Pb_nX_{3n+1}$, AIE cations of BPCSA and FPCSA were introduced in PVSK precursor. XRD was used to characterize the structure, crystallinity, and phase distribution of the films. UV–vis absorption, PL spectroscopy, and TRPL spectroscopy were employed for optical properties assessment. In the hybrid system, the present study also investigates how AIE excitons engage PVSK excitonic states to aid with knowledge on energy and charge transfer. The AIE-active BPCSA and FPCSA cations investigated in this work can be considered a new class of organic semiconductor components incorporated into layered perovskites. Unlike conventional alkylammonium spacers, which primarily function as electronically insulating barriers, conjugated organic cations can contribute frontier molecular orbitals near the band edges of the inorganic framework and thereby modify the energy landscape of the hybrid material. Previous organic semiconductor-incorporated perovskites have demonstrated Type-I, Type-II, and reversed-Type-I alignments through variation of the conjugated ligand structure. The present work extends this strategy by incorporating AIE-active cyanostilbene cations, which combine tunable electronic energy levels with solid-state luminescence.

5.2. Single-layered 2D PVSKs

We studied the structure and electronic properties of $BPCSA_2PbI_4$, $FPCSA_2PbI_4$, $BPCSA_2PbBr_4$ and $FPCSA_2PbBr_4$ as well as their comparison with the reference aliphatic system OA_2PbI_4 and OA_2PbBr_4 to test the potentials of AIE-active organic cations for iodide/bromide-based single-layered 2D PVSKs.

We analyzed the electronic structure and alignment of bands using UPS and optical bandgap analysis for AIE-based 2D PVSK systems. Thanks to these techniques, we were able to understand the interfacial energetics controlling charge and energy transfer. The UPS spectra,

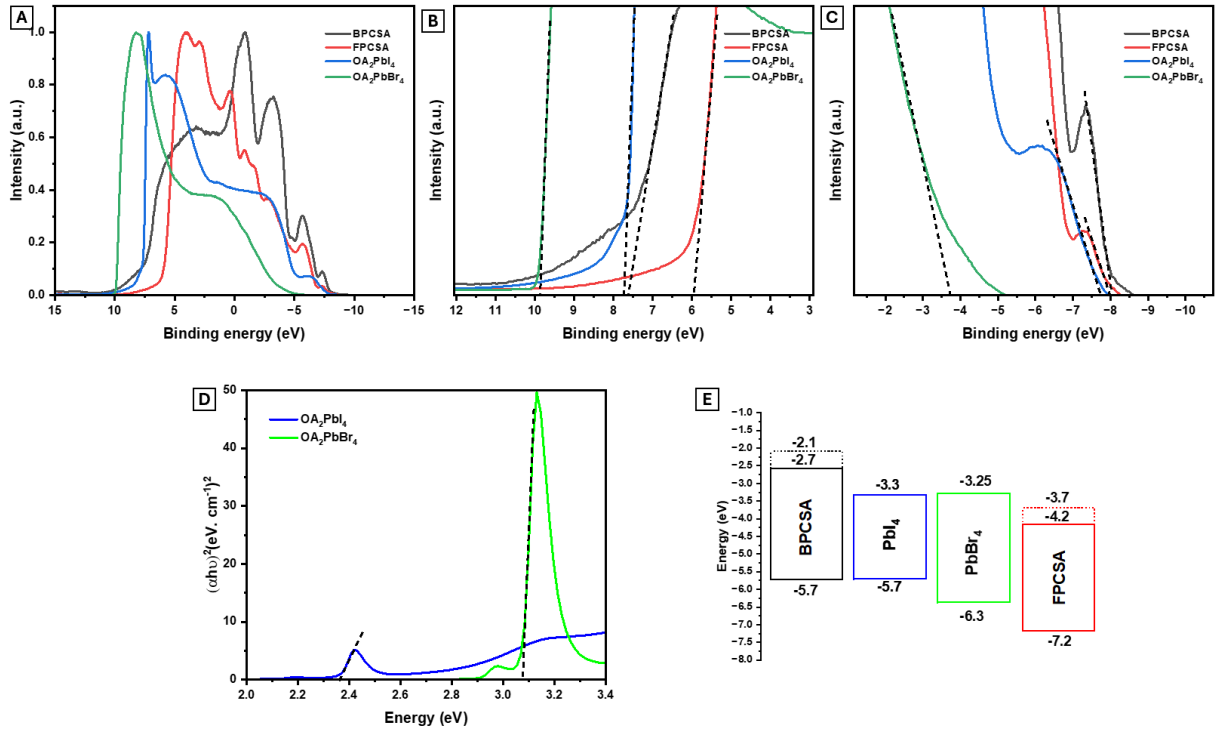

Figure 5.1. (A) - UPS plot of BPCSA, FPCSA, OA_2PbI_4 and OA_2PbBr_4; (B) and (C) – secondary electron cutoff region and valence band edge region originated from UPS plot, respectively; (D) – Tauc plot of OA_2PbI_4 and OA_2PbBr_4 and (E) – energy band diagram.

presented on Figure 5.1A, showed a significant difference in secondary electron cutoff and valence band edge between BPCSA, FPCSA and reference PVSK systems. This reflects important molecular-design-induced change in work function and frontier orbital energies.

In general the summary UPS spectra of BPCSA shows that this material has a higher secondary electron cutoff than FPCSA, thus suggesting lower work function, shallower electronic framework or structure. But on the other hand, we see the FPCSA exhibits a clear transition to lower energy suggesting a deeper work function and the greater electron withdrawing effect. This is consistent with the role played by fluorine in FPCSA which stabilizes filled and empty molecular

orbitals. The PVSK reference (OA_2PbI_4) sits between these two, demonstrating a more inorganic electronic architecture of the material. For BPCSA < PbI_4 < FPCSA, work function values were calculated from the analysis of the secondary electron cutoff region (see Figures 5.1B). These studies show that changes of organic spacer can systemically alter the surface electronic properties of the hybrid material. The deeper work function of the FPCSA means higher electron affinity or electronic state stabilization, which is directly proportional to interfacial charge transfer or carrier confinement. The valence band region and Tauc plots is further used to examine the alignment of the electronic states (see Figure 5.1C and D, respectively). The VBM of the PbI_4 layer is about −5.7 eV, as in many kinds of iodide-based 2D PVSKs [49,147-149]. BPCSA's maximum occupied molecular orbital (HOMO) value is close to −5.7 eV with valence band near PVSK valence band. Due to the close association there is minimal energy barrier for holes to transfer between the organic and inorganic phase in the system, indicating some kind of electronic coupling or interfusion between organic and inorganic. Meanwhile, FPCSA has an HOMO peak of ~ -7.2 eV, giving rise to a wide energy-gap distance away from the PVSK valence band, making for hole transfer less favorable due to much deeper HOMO. These results support the optical bandgaps of Tauc-analysis. The inorganic PVSK exhibits a bandgap between around 2.4–2.5 eV and its CBM is around −3.3 eV. BPCSA displays optical transitions of approximately 3.0 eV, and its LUMO exists above the PVSK conduction band. After excitation, electrons and holes generally remain in the inorganic layer which makes this quasi-type-I alignment. Consequently, the energy that BPCSA absorbs is rapidly transferred to the PVSK, resulting in highest emission of the inorganic group. In contrast, FPCSA exhibits a deeper LUMO at −4.2 eV, significantly lower than the PVSK conduction band. When it is coupled with its deeper HOMO level, these have a strongly staggered band alignment with wide energy gaps at both the valence and conduction band edges. These gap distances (0.4–1.0 eV) are sufficient to make charge and energy transfer across the interface much smaller [150]. In this way, the excitons generated in FPCSA remain in the organic, and those in PVSK stay in the inorganic. The energy level diagram outlines the differences visible on the interface. With a small energy gap between the HOMO of the organic cation and the VBM of the PVSK, the energy from HOMO is transferred to the inorganic layers in a reduced gap in the BPCSA system. That is why organic emission is quenched efficiently in photoluminescence tests. In a FPCSA system, large energy gaps distinguish between the two sections, preventing recombination at the interface and permitting free emission of both organic and inorganic layers.

The present UPS results are consistent with the broader concept of organic semiconductor-incorporated perovskites, in which the electronic structure of the organic component can be deliberately positioned relative to the inorganic band edges. While conventional wide-bandgap spacers generally form Type-I quantum wells, conjugated organic cations can generate Type-II or reversed-Type-I alignments. In the present systems, fluorination of the cyanostilbene core stabilizes the frontier molecular orbitals of FPCSA and changes its alignment relative to the lead-halide framework. Thus, the transition in band alignment is achieved through targeted molecular modification of an AIE-active cation rather than by changing the entire conjugated backbone.

X-ray diffraction and excitation–emission contour mapping presented in Figure 5.2A and Figure 5.2B-E, respectively, verify the structure and the photophysical behavior of the PVSKs incorporated with AIE. These approaches demonstrate that molecular design strongly influences the lattice organization and the emission in both iodide and bromide systems. It can then be inferred from X-ray diffraction patterns that all the samples like $BPCSA_2PbI_4$, $FPCSA_2PbI_4$, and their bromide mixtures possess the characteristic layered RP structure. The frequent (00*l*) sharp reflections like (002), (004), (006), (008) suggest the crystallographic structure is highly ordered followed by clear stacking of inorganic layers separated with organic spacers. All samples displayed similar peak patterns such that altering the organic cation did not result in any distortion

of the layered structure. Nevertheless, slight variations in peak positions and intensities between iodide and bromide systems indicate a change in the interlayer spacing and lattice periodicity.

This change can be explained by factors such as halide action on octahedral shape and size and electronic properties on the AIE cations. The introduction of the π-conjugated cations appears

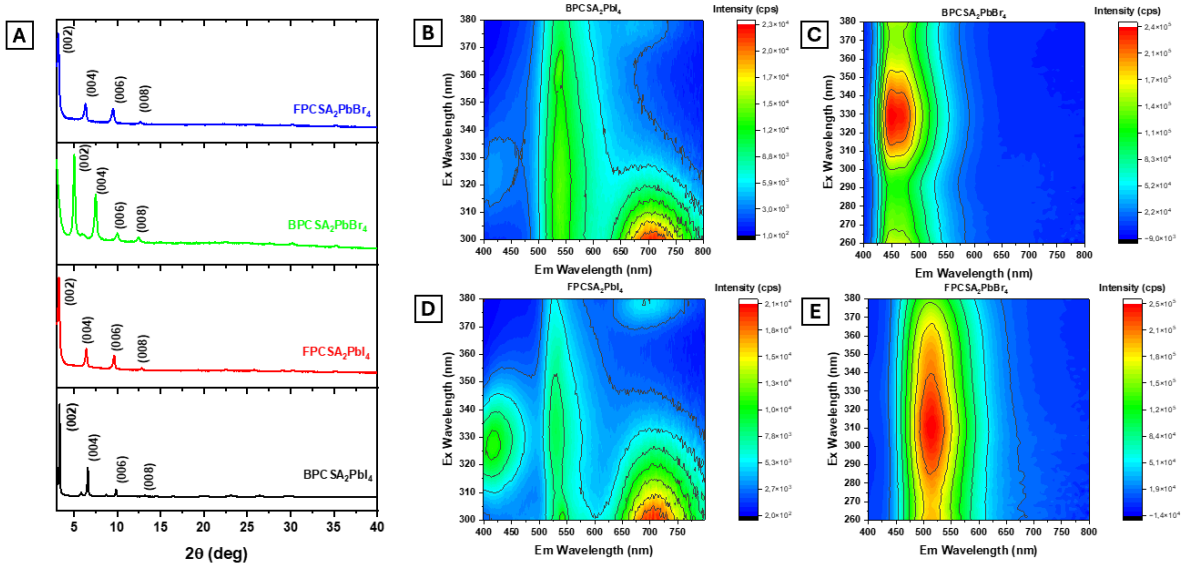

Figure 5.2. (A) – XRD patterns of n=1 AIE dye incorporated 2D PVSKs; Excitation dependent PL emission color map of (B) – $BPCSA_2PbI_4$, (C) – $BPCSA_2PbBr_4$, (D) $FPCSA_2PbI_4$ and (E) – $FPCSA_2PbBr_4$.

to favor further ordering of stacking and slightly alters layer spacing, similar to the aliphatic conventional systems, which are characterized by stronger interactions within the organic layers. Excitation–emission contour maps illustrate how the emission processes are dependent on the excitation wavelength. A 2-feature enhancement for BPCSA-based iodide PVSK from band-edge free exciton (FE) recombination at 520–550 nm and a strong and broad emission from ~650–750 nm attributed to self-trapped excitons (STE) were observed. The wide spectrum of red-shifted emission indicates that there is an excellent exciton–phonon coupling and a readily available formation of localized states in the soft iodide structure. STE emission is enhanced with higher-energy excitation, and therefore reaching these localized states requires additional energy, which were probably produced by thermal or tunnel mechanisms. The BPCSA is also different emission pattern when it comes to bromide. Its contour map mainly has this small region at 450–480 nm, and the emission is much weaker at longer wavelengths. This is attributed to the increased bandgap and stronger lattice of the bromide PVSK preventing exciton self-trapping coupled with direct

band-edge recombination. The absence of a strong red emission band indicates that the electron–phonon coupling is weak and the self-trapped states are fewer than in iodide system. FPCSA-based systems display a much different behavior than UPS systems due to the electronic decoupling. In FPCSA PVSK based on iodide, the contour map of various emission channels appears. Apart from the band-edge emission at 530–560 nm and the broad self-trapped exciton emission at 700 nm, there is also high energy blue emission at around 400–430 nm, which is due to radiative recombination in the FPCSA cation. As a result of this blue emission, it remains visible in different excitation wavelengths because organic excitons are largely apart from inorganic, and therefore energy transfer is inhibited. FE and STE emissions produce a varied, multi-band emission pattern. In the bromide form of the FPCSA system, emission is largely in the blue–green region, with an overall main band at 450–500 nm and low emission at longer wavelengths. The stiffer lattice makes it less likely that self-trapped excitons will form, like the BPCSA bromide system. Nevertheless, the high-energy emission intensity is a good indication that the organic exciton is active, indicating that the organic and inorganic components exist electronically separate in FPCSA-based systems.

The time-resolved photoluminescence measurements of the n = 1 systems, now including the reference octylammonium-based PVSKs, provide a comprehensive picture of how organic spacer chemistry governs exciton dynamics and recombination pathways in layered structures. The decay profiles clearly distinguish between band-edge free exciton recombination and slower processes associated with self-trapped excitons, while also highlighting the fundamental differences between aliphatic and AIE-based spacer systems.

The decay of OA-based reference samples shows relatively fast and simple decay behavior that is typical for sufficiently constrained 2D PVSKs with a small amount of lattice distortion [151]. At ~520 nm, OA_2PbI_4 emission corresponds to a very short lifetime of approximately 0.65 ns, demonstrating the rapid radiative recombination of free excitons without causing any carrier trapping. Likewise, OA_2PbBr_4 exhibits a slightly longer but still fast decay of ~1.83 ns at ~410 nm, indicating band-edge recombination in a wider bandgap system. The absence of any long-lived component in both iodide and bromide OA-based samples confirms that self-trapped exciton

formation is effectively suppressed due to the flexible aliphatic spacer, which minimizes lattice strain and electron–phonon coupling.

In contrast, the incorporation of rigid, π-conjugated AIE cations significantly alters the

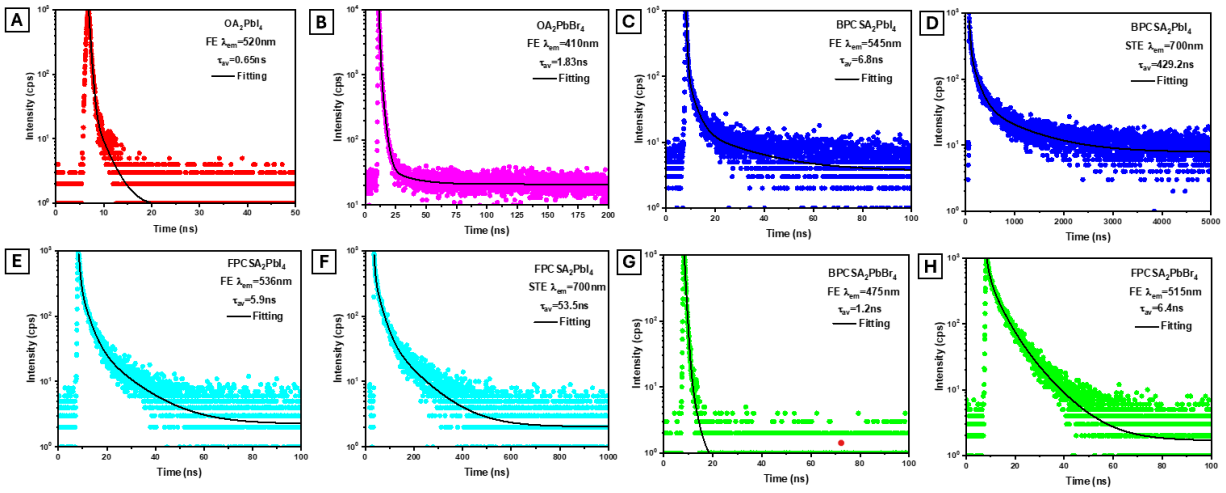

Figure 5.3. TRPL spectra of (A) – OA_2PbI_4 λ_{em}=520nm; (B) – OA_2PbBr_4 λ_{em}=410nm; (C) - $BPCSA_2PbI_4$ λ_{em}=545nm, (D) – $BPCSA_2PbI_4$ λ_{em}=700nm; (D) $FPCSA_2PbI_4$ λ_{em}=536nm, (F) – $FPCSA_2PbI_4$ λ_{em}=700nm; (G) - $BPCSA_2PbBr_4$, λ_{em}=475nm and (H) - $FPCSA_2PbBr_4$, λ_{em}=515nm.

recombination mechanism. In the case of $BPCSA_2PbI_4$, the free exciton emission at about 545 nm has a lifetime of ~6.8 ns, much longer than that for the OA-based iodide system which indicates reduced recombination rate and enhanced carrier interaction with the lattice. Even more remarkably, the self-trapped exciton emission at ~700 nm has a very long lifetime of ~429 ns, supporting the formation of deeply localized states sustained by strong lattice distortion. This substantial temporal separation of free and self-trapped exciton decay channels indicates the rigid cation in AIE causes exciton localization and slows recombination once the carriers are trapped.

The $FPCSA_2PbI_4$ exhibits the same dual channel characteristics but a very different set of dynamics. FE emission at ~536 nm has a lifetime of ~5.9 ns, which is close to the lifetime of the BPCSA system, and indicates that band-edge recombination in the inorganic layer is mostly unharmed by the specific AIE cation. The STE emission at ~700 nm has a much shorter lifetime (approximately ~53.5 ns) compared to $BPCSA_2PbI_4$ lifetime. Such large reduction suggests that the trapped state is unstable and that carriers can recombine or exit from the localized configuration. The above behavior is in accordance with the decreased trapping depth and faster recombination activity by the deeper electronic levels and changed band alignment that fluorination introduces.

In addition, the bromide-based AIE systems highlight the importance of lattice stiffness in inhibiting carrier localization. In $BPCSA_2PbBr_4$, the emission at ~475 nm has a rapid decay at ~1.2 ns, similar to the OA-based bromide system, which implies dominant band-edge recombination with little trapping. There is also no notable long-lived component characteristic of the sample indicating the absence of many self-trapped excitons at bromide lattice because of weaker electron–phonon coupling. $FPCSA_2PbBr_4$ emission at ~515 nm has a lifetime slightly longer near (~6.4 ns), which might represent a decreased impact of non-radiative losses or partial carrier confinement, but continues to be limited to the nanosecond range which confirms band-edge recombination. The addition of specific references based on OA techniques unequivocally points out the change from simple excitonic recombination in flexible, loosely interacting lattices to complex multi-channel recombination in AIE systems. The aliphatic OA spacer provides high-speed and low-trapping free exciton discharge, while the rigid AIE cations induce large lattice distortion and allow for long-lasting self-trapped excitons to form, especially for iodide systems. The comparison of BPCSA and FPCSA is further proof-point that some small alterations such as fluorination affect the stability and lifetime of trapped states rather than band-edge recombination. From above results, it is seen that both spacer stiffness and electronic material configuration are relevant parameters to control exciton motion and emission of a 2D PVSK.

The optical absorption or emission of n=1 AIE-based PVSKs also offers more understanding regarding the role of organic spacer and halide composition on light–matter behavior and the total photophysical efficiency. The UV–visible absorption spectra demonstrate that all of the samples still have the typical excitonic absorption characteristics of layered PVSKs, with a prominent peak found in the near-UV to visible region. The reference OA_2PbI_4 demonstrates a clear excitonic absorption at the ~500 nm peak phase, corresponding to the band-edge transition position of the PbI_4 inorganic layer. However, OA_2PbBr_4 displays a distinctly blue-shifted absorption edge near ~400 nm, consistent with the broader bandgap of the bromide system. Furthermore, following the introduction of AIE cations, complementary absorption features are obtained in the higher-energy region (300–400 nm), as the π–π* transitions of conjugated organic molecules are shown. BPCSA- and FPCSA-based iodide PVSKs exhibit broad absorption profiles that extend across the UV spectrum, suggesting absorption from the organic component overlapped with excitation wavelengths detected for PL measurements. The bromide analogues exhibit comparable patterns, but overall blue-shifted absorption because of the halide substitution.

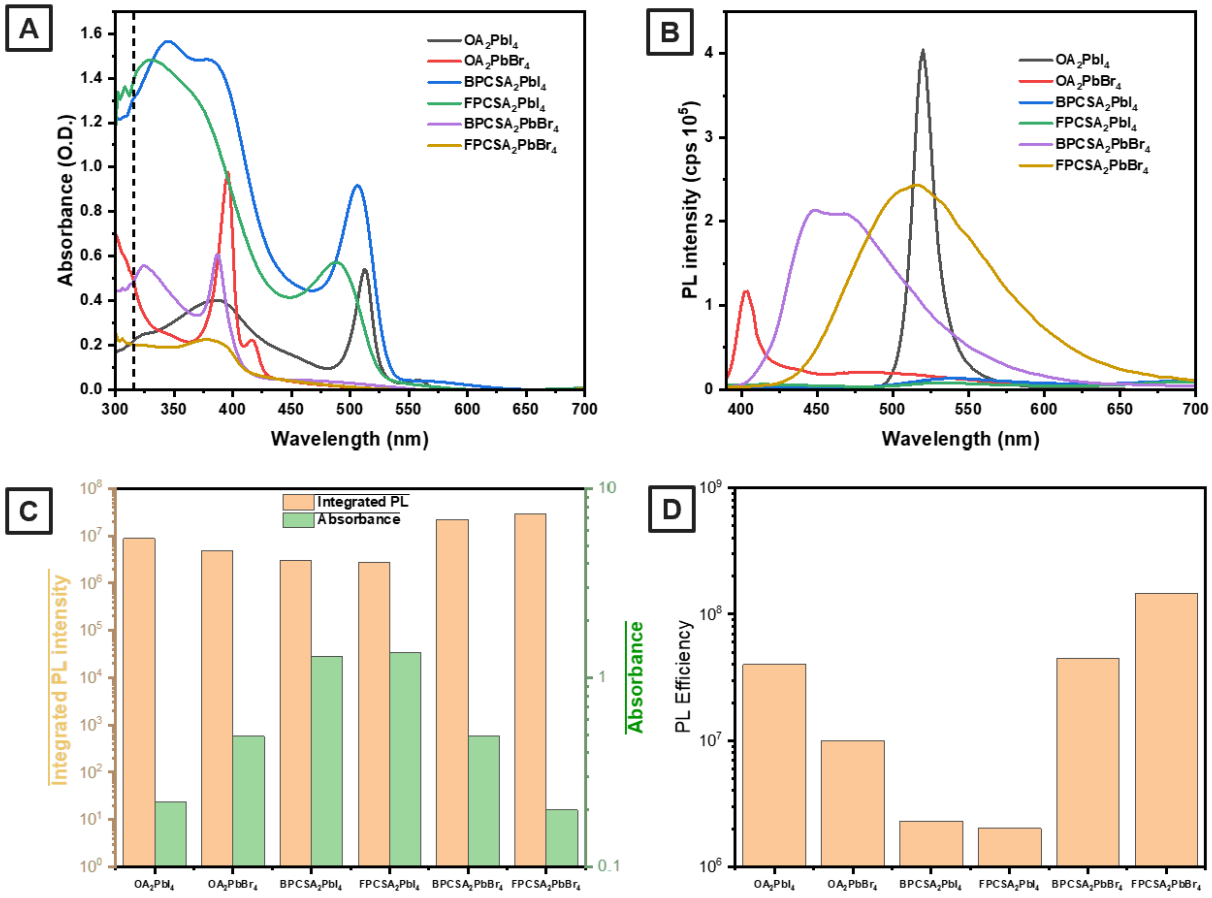

Figure 5.4. (A) – UV-vis absorbance spectra, (B) – PL emission spectra and (C) – ratio of Integrated PL to absorbace at 315nm and (D) – PL efficiency of OA-based n=1 PVSKs and AIE dye incorporated 2D perovskites.

The steady-state photoluminescence spectra demonstrate significant emission behaviour differences between spacer cation and halide. The reference OA_2PbI_4 shows a relatively narrow emission near ~520 nm that mirrors the free recombination of excitons in a tightly confined 2D PVSK without lattice distortion. The $BPCSA_2PbI_4$ emission, however, has a dual emission with a green range ~540–550 nm and a broad red spectral region extending toward ~700 nm, both reflecting the presence of band-edge and self-trapped exciton recombination. This broad, red-shifted emission reflects improved exciton–phonon coupling and more lattice distortion due to the rigid, π-conjugated AIE cation. $FPCSA_2PbI_4$ shows an even more complicated emission pattern with lower intensity in the green region and a greater broad emission at longer wavelengths, indicating that the modified electronic structure and interfacial energetics further promote non-band-edge recombination paths. For bromide systems, OA_2PbBr_4 shows a sharp emission near ~410 nm, while $BPCSA_2PbBr_4$ and $FPCSA_2PbBr_4$ exhibit broadened emission profiles, albeit with

shifts toward longer wavelengths, though the overall spectral width is significantly narrower with respect to iodide-related systems. Such behaviour highlights the reduced lattice softness and weaker electron–phonon coupling of bromide PVSKs, restricting the generation of strongly localized self-trapped states.

Although absolute PLQY values were not measured in the present work due to instrumentation limitations, several experimental observations indicate efficient radiative recombination in the developed AIE-incorporated perovskites. o provide a comparative assessment of the emission efficiency of the synthesized perovskites, the integrated photoluminescence (PL) intensity was normalized by the absorbance at the excitation wavelength (315 nm), as shown in Figures 5.4C and D. . Since all samples were measured under identical excitation conditions, the ratio between integrated PL and absorbance provides a relative measure of the radiative emission efficiency by accounting for differences in the amount of absorbed excitation light and emitted light. This approach, unfortunately, can't be used to measure PLQY, however we can estimate to what extend PL efficiency of AIE incorporated 2D PVSKs is higher or lower compared to control samples. Although the AIE-based PVSKs showed high absorption rates in the UV region, their integrated PL intensities varied significantly between the cation and halide. For the bromide series, $BPCSA_2PbBr_4$ and $FPCSA_2PbBr_4$ exhibit approximately 4-fold and 14-fold higher relative PL efficiencies, respectively, than OA_2PbBr_4. This substantial enhancement demonstrates that replacing the insulating OA spacer with conjugated AIE cations effectively suppresses non-radiative recombination and increases the fraction of absorbed photons converted into emitted photons. Strong exciton confinement is known to favor radiative recombination in conventional n = 1 layered perovskites. However, the present comparison with OA-based controls shows that confinement alone does not determine the emission efficiency. The considerably higher relative PL efficiency of $BPCSA_2PbBr_4$ and $FPCSA_2PbBr_4$ indicates an additional contribution associated with the optically active AIE cations and their coupling to the inorganic layer [102, 110, 111, 134, 140, 152]. In contrast, the iodide analogues ($BPCSA_2PbI_4$ and $FPCSA_2PbI_4$) show lower relative PL efficiencies than OA_2PbI_4, despite their comparable absorption. This reduction is attributed to the formation of a type-II band alignment, which promotes interfacial charge transfer and competes with radiative exciton recombination. These results demonstrate that AIE incorporation does not universally increase emission efficiency; rather, the outcome depends strongly on the electronic band alignment. When efficient charge transfer is absent, as in the

bromide systems, AIE cations markedly improve the radiative efficiency compared with the OA-based reference.

The steady-state photoluminescence, plus the excitation-emission maps, combined with these results offer an overview of the emission mechanisms in AIE–PVSK hybrids. A strong tool available for controlling emission bandwidth, color balance and timing of these materials is the modulation not just of the formation of self-trapped excitons but also of their lifetime using the molecular design and halide selection. Unpulsed steady-state photoluminescence spectra, when irradiated with ultraviolet light, further support the theory that the effects of the organic cation design on excitonic processes determine the final emission pattern and colors perceived by the hybrid systems. At 315 nm of UV excitation, the $FPCSA_2PbI_4$ sample's emission is extensive and multi-component covering most of the visible area. Three spectral contributions are clearly identifiable: a highly energetic band around 420 and 440 nm due to radiative recombination of the FPCSA cation; a green emission centered between 520 and 550 nm caused by free exciton recombination of the inorganic PbI_4 layer; and a broad red band ranging from 650 to 780 nm from self-trapped excitons. These three emission channels are balanced and show a continuous spectral distribution similar to white light.

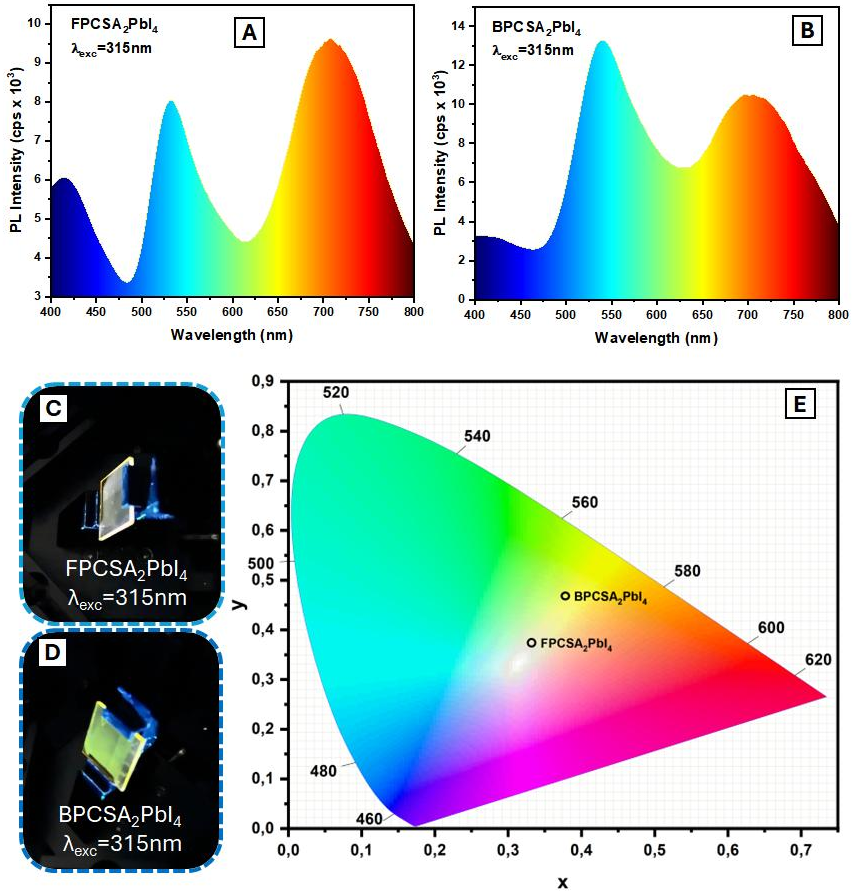

Figure 5.5. (A) and (B) – PL emission spectra of $FPCSA_2PbI_4$ and $BPCSA_2PbI_4$ at λ_{exc}=315nm, respectively; (C) and (D) - photographs of $FPCSA_2PbI_4$ and $BPCSA_2PbI_4$ thin films at λ_{exc}=315nm, respectively; (E) – CIE coordinates.

Conversely, the emission spectrum of $BPCSA_2PbI_4$ under the same excitation conditions is dominated by two main bands. A robust green emission around 540–550 nm arises from band-edge excitonic recombination, while a broad red emission around 700 nm represents self-trapped excitons. The blue emission associated with the organic cation is weak or absent, indicating that the excitation energy absorbed by BPCSA is efficiently transferred to the PVSK lattice. As a result, the total emission is deficient in short-wavelength contributions and appears shifted toward the yellow region. These differences in spectral distribution are directly reflected in the actual luminescence photographs.

The sample based on FPCSA emits a bright white light under UV illumination, whereas the BPCSA-based sample shows a warmer yellow emission. This difference is also expressed in chromaticity coordinates from the corresponding Commission Internationale de l'Éclairage (CIE). Concentrated in the CIE diagram, the emission of $FPCSA_2PbI_4$ is near the central region, with

coordinates around (0.33, 0.38), suggestive of balanced white emission. By contrast, $BPCSA_2PbI_4$ is found at higher x and y values, around (0.38, 0.47), indicating a yellowish output dominated by longer wavelengths. The presence of white light emission in the FPCSA-based system can be traced back to the inhibited interfacial coupling between the organic and inorganic constituents. The large energetic offsets generated by fluorination prevent efficient energy transfer from the organic cation to the PVSK lattice, thereby allowing the blue emission from FPCSA to coexist with the green band-edge and red self-trapped exciton emissions. On the contrary, the favorable energetic alignment in the BPCSA system allows rapid energy transfer, which effectively quenches the organic emission and narrows the spectral coverage.

Collectively, the findings indicate that fine-tuning of interfacial energetics facilitates the optimization of emission spectra that range from dual-band to full-spectrum white light emission. Organic exciton emission, band-edge recombination, and self-trapped exciton processes can be optimized for targeted chromaticity, without the need for external phosphors or multi-component blending. This points to the possibility of AIE–PVSK hybrid systems being inherently broadband emitters for solid-state lighting and display applications.

5.3. Double-layered quasi-2D PVSKs

In order to explore the influence of AIE organic cations on higher-order layered perovskites, we explored the electronic structure of n = 2 quasi-2D systems, $OA_2MAPb_2I_7$ and $OA_2MAPb_2Br_7$, in combination with BPCSA and FPCSA. The UPS spectral results, the obtained bandgap and the associated energy level alignments are presented under Figure 5.6. The complete UPS spectra (see Figure 5.6A) show prominent electronic characteristics of the organic AIE molecules and of quasi-2D perovskites. The work function and the highest occupied electronic states were determined from the secondary electron cutoff region (see Figure 5.6)), and the valence band onset (see Figure 5.6C) was used to extract the highest occupied electronic states. These measurements also give values indicating that the HOMO levels of the AIE molecules correspond

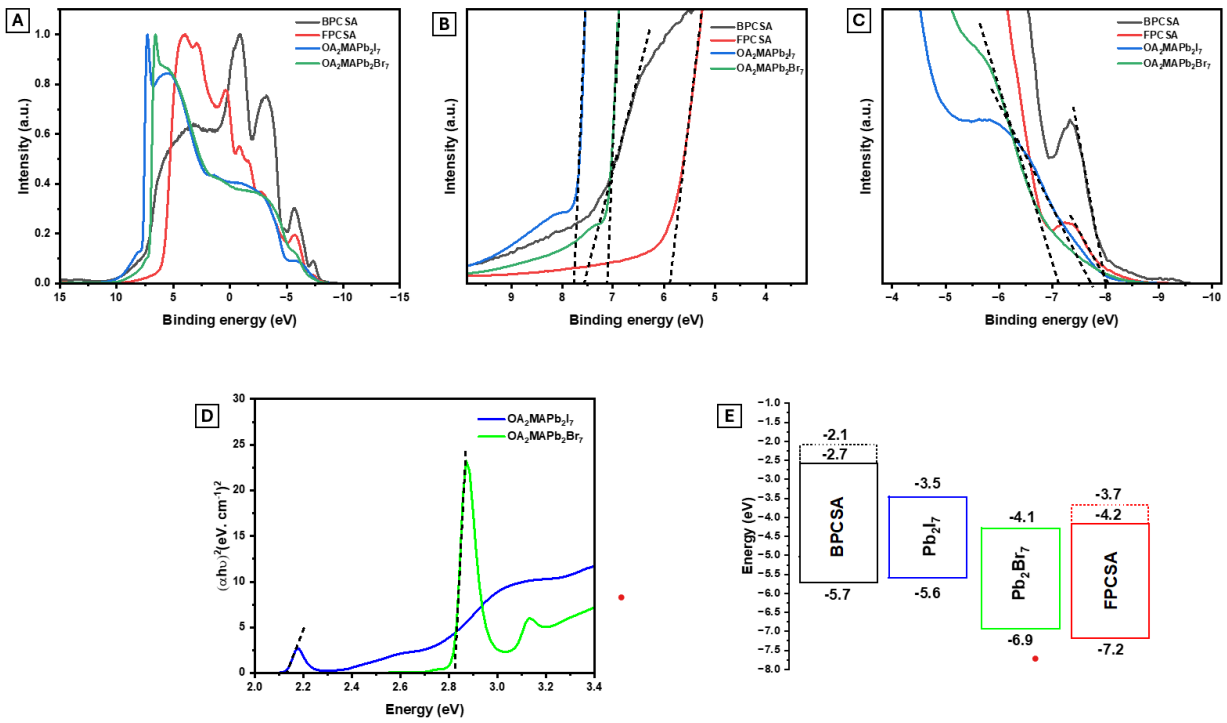

Figure 5.6. (A) - UPS plot of BPCSA, FPCSA, $OA_2MAPb_2I_7$ and $OA_2MAPb_2Br_7$; (B) and (C) – secondary electron cutoff region and valence band edge region originated from UPS plot, respectively; (D) – Tauc plot of $OA_2MAPb_2I_7$ and $OA_2MAPb_2Br_7$and (E) – energy band diagram.

to about −5.7 eV for BPCSA and −7.2 eV for FPCSA. The strongly binding effect of fluorine replacement to stabilize the molecular electronic structure contributes to th e much more profound HOMO in FPCSA. For the quasi-2D perovskites, the valence band maxima for $OA_2MAPb_2I_7$ were found to be around −5.6 eV and −6.9 eV for $OA_2MAPb_2Br_7$. This deeper valence band of the bromide-based system is congruent with the higher electronegativity of bromine than iodide, which enhances orbital stabilization. The optical bandgaps on the quasi-2D perovskites were acquired from Tauc plots (see Figure 5.6D). $OA_2MAPb_2I_7$ shows a bandgap of about 2.2 eV and $OA_2MAPb_2Br_7$ reveals a bandgap of ~2.9 eV. These results are significantly smaller than in n = 1 systems, indicating that the quantum interphase confinement is less, the result of the thickening of the inorganic layers. Moreover, some characteristics of the absorption spectra are provided, especially for the iodide-based system, demonstrating the existence of mixed n phases. This phase distribution is what quasi-2D perovskites exhibit and produces energy funneling, whereby excitations pass from the higher-bandgap to lower-bandgap domains before recombination. The UPS and optical data-based energy level figure (Figure X(E)) shows the interfacial electronic

interactions. For BPCSA, the HOMO level (−5.7 eV) reflects strongly the valence band of $OA_2MAPb_2I_7$ (−5.6 eV) indicating strong electronic coupling and a near-type-I band alignment. This arrangement effectively allows for energy transfer from organic cation to the inorganic perovskite layer with most excitons being confined in the inorganic structure. In contrast, FPCSA shows considerably deeper frontier orbitals, leading to a type-II alignment with Pb_2I_7 and type-I alignment with Pb_2Br_7. This may result in more efficient energy transfer from FPCSA to Pb_2Br_7 framework and enhances coupling between the organic and inorganic components and at the same time it may result in charge-transfer emission at the FPCSA/Pb_2I_7 interface.

The structural and excitation–emission features of n = 2 double layered AIE-based PVSKs also demonstrate that both the layered design as well as the photophysical behavior strongly depend on the interaction effect of organic spacer formulation and halide composition. The shapes of all compositions, including the $BPCSA_2MAPb_2I_7$, $FPCSA_2MAPb_2I_7$, and equivalent bromide, exhibit distinct layered RP phases with a clear X-ray diffraction pattern (see Figure 5.7A). Multiple higher-order reflections (00l) such as (002), (004), (006) and further imply that it is a fairly crystalline and periodic stacking from the out-of-plane direction. The diffraction patterns of n = 2 PVSKs also appear more complex than those of n = 1 systems, showing more reflective peaks than the ones that are observed for n = 1 systems and corresponding growth of the unit cell. The presence of sharp and consistently spaced peaks in all samples indicates that the incorporation of the AIE cations does not inhibit the deposition of the double-layer framework, but is entirely compatible with the crystallization of relatively thicker inorganic slabs. Diffraction patterns of iodide and bromide systems also differ. The bromide-based PVSKs show peaks shifted toward the higher angles, which is in agreement with decrease of lattice parameters, in view of bromide having a smaller ionic radius than iodide. Furthermore, the peak intensity and sharpness differences indicate minor variations of crystallinity and layer order are likely a compromise between halides and cations, particularly between AIE cations. The BPCSA-loaded systems manifest stronger higher-order reflections, indicating well-arranged stacking, while the FPCSA-loaded ones become more apparent. A reflection of more structural disorder or distinct packing interactions associated

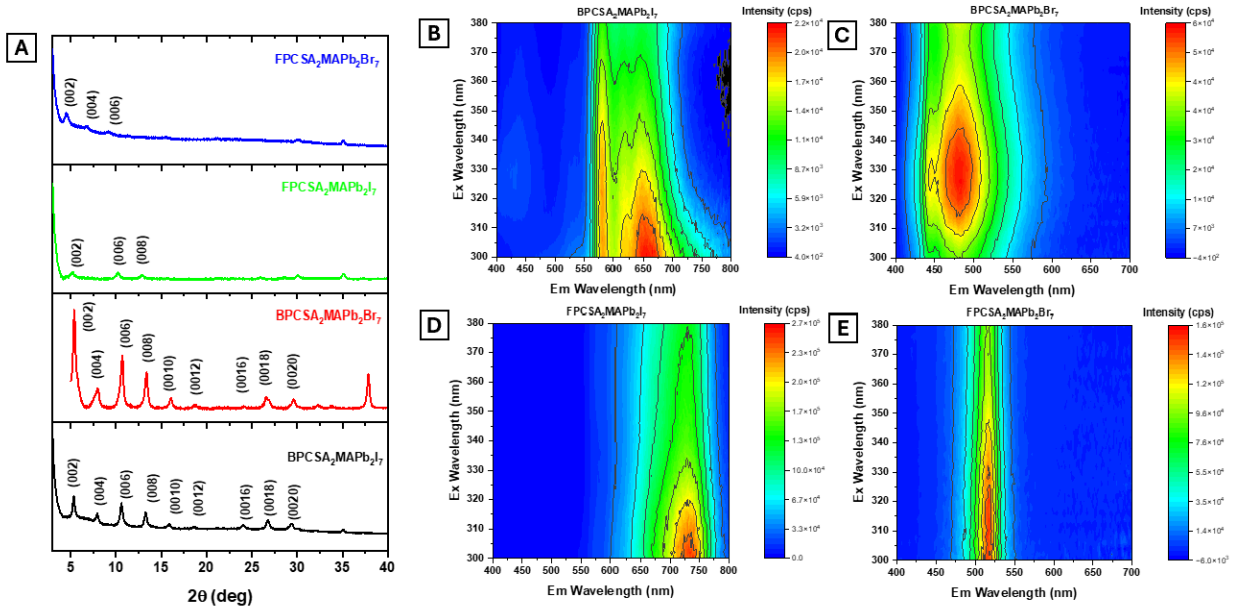

Figure 5.7. (A) – XRD patterns of n=2 AIE dye incorporated 2D PVSKs; Excitation dependent PL emission color map of (B) – $BPCSA_2MAPb_2I_7$, (C) – $BPCSA_2MAPb_2Br_7$, (D) $FPCSA_2MAPb_2I_7$ and (E) – $FPCSA_2MAPb_2Br_7$.

to fluorination. Excitation–emission contour maps give useful information of how emission processes change in the n = 2 systems. In BPCSA-based iodide PVSK, emission consists mostly of a large band focusing on 650–720 nm, which extends in a large section of excitation wavelengths (see Figure 5.7B). This characteristic property underlies the strong self-trapped exciton emission and suggests that the thicker inorganic slab in n = 2 still provides strong lattice distortion and carrier localization. A less visible yet weak emission band around 520–560 nm in the green region is also seen, which reflects free exciton recombination. The presence of these features indicates that the band-edge and self-trapped states remain accessible, but that the trapping process is particularly efficient in the iodide-based n = 2 system.

In contrast, the bromide analogue of the BPCSA (Figure 5.7C) system exhibits a much narrower emission profile centered around 450–500 nm, with minimal contribution from longer wavelengths. This behavior reflects the larger bandgap and reduced lattice softness of the bromide PVSK, which suppresses self-trapped exciton formation and favors direct recombination of free excitons. The emission intensity is also more localized in excitation space, indicating a more straightforward relaxation pathway with fewer competing emissive states.

As shown by our observations, the emission behavior of n = 2 FPCSA-based systems exhibits distinct behavior that mirrors the electronic decoupling inferred from band alignment

analysis. For iodide-based FPCSA PVSK, the emission is highly red-shifted with the most dominant band extending from approximately 650 to 780 nm. One can conclude that STE emission is highly favored, probably owing to the strong electron–phonon coupling within the iodide lattice and reduced interfacial energy transfer that would otherwise compete with trapping processes. However, this ~700 nm emission exhibits a fast decay (τ_{av} = 6.8 ns [see Figure 5.8D]), which excludes the possibility of a STE contribution. Moreover, the typical emission wavelength for an n = 2 iodide-based 2D perovskite is around 450 nm, suggesting that the observed 700 nm emission likely arises from charge transfer $LUMO_{FPCSA} \rightarrow VB_{Pb2I7}$. It can be observed on Figure 5.6E, that energy gap between $LUMO_{FPCSA}$ and VB_{Pb2I7} is 1.4 eV, which is approximately 700nm. For the bromide-based FPCSA system, the emission is predominantly in the green region around 500–530 nm, with a relatively narrow distribution and negligible long-wavelength tail. This again demonstrates the rigidity of the bromide lattice and the reduced propensity for exciton self-trapping. By contrast, the lack of significant high-energy emission features in the contour map leads to the conclusion that while FPCSA is electronically coupled with Pb_2Br_7. In previously reported Type-II COCiPs, spatial separation of electrons and holes frequently resulted in substantial quenching of both inorganic and organic excitonic emission [102,103,134,152, 153]. In contrast, $FPCSA_2MAPb_2I_7$ exhibits an intense broad red-shifted band, indicating that the separated interfacial carriers retain a radiative recombination pathway. This suggests the formation of an emissive interfacial charge-transfer state rather than exclusively non-radiative charge separation.

The time-resolved photoluminescence behavior of the n = 2 double-layered PVSKs further illustrates how enhancement of the inorganic slab thickness alters exciton dynamics without losing the potent contribution of the organic spacer. The recombination processes in n = 2 structures are generally faster and more dominated by band-edge emission compared to the n = 1 structures, which indicates reduced quantum confinement and altered lattice relaxation pathways. The OA-related reference samples demonstrate rapid decay dynamics, which is characteristic of free exciton recombination with minimal trapping once more. In $OA_2MAPb_2I_7$, emission at ~570 nm demonstrates very short lifetime (~0.46 ns), even shorter than n = 1, suggesting highly efficient radiative recombination in the thicker inorganic slab.

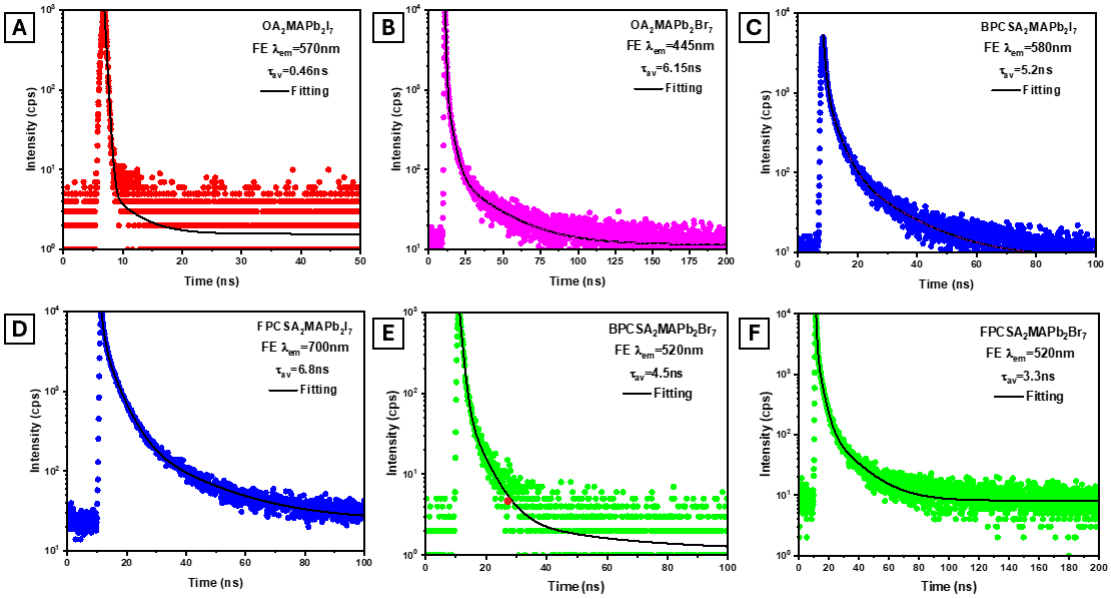

Figure 5.8. TRPL spectra of (A) – $OA_2MAPb_2I_7$ λ_{em}=570nm; (B) – $OA_2MAPb_2Br_7$ λ_{em}=445nm; (C) - $BPCSA_2MAPb_2I_7$ λ_{em}=580nm, (D) – $FPCSA_2MAPb_2I_7$ λ_{em}=700nm; (D) $BPCSA_2MAPb_2Br_7$ λ_{em}=520nm, (F) – $FPCSA_2MAPb_2Br_7$ λ_{em}=520nm.

On the other hand, $OA_2MAPb_2Br_7$ shows a rapid decay of ~6.15 ns at ~445 nm consistent with the band-edge recombination of bromide. The absence of any long-lived component proves that exciton localization is still negligible in these flexible, aliphatic spacer systems, even in the n = 2 configuration. Furthermore, the inclusion of AIE cations results in a clear increase of carrier lifetime—even if its behavior differs from the n = 1 case. In $BPCSA_2MAPb_2I_7$, the emission at ~580 nm is ~5.2 ns long lifetime and significantly longer compared to OA-based iodide system. This shows that the rigid, conjugated spacer introduces an extra connection into the excitonal process, causing recombination to slow. But in contrast to the n = 1 analogue, no robust long-lived component corresponding to self-trapped excitons is observed within the measured time window. This indicates that, while lattice distortion remains, the thicker inorganic slab diminishes the stability or formation probability of deeply trapped states.

A more specific pattern has been observed for $FPCSA_2MAPb_2I_7$, the emission near ~700 nm has a lifetime of ~6.8 ns. Although the red-shifted emission could point to the involvement of self-trapped excitons, the short lifetime suggests that the excitons in these states are not as localized as in n = 1 systems. Rather, the emission is most likely attributable to shallow localized states or evolved band-edge recombination affected by the electronic properties of the FPCSA cation. Not possessing a long-lived decay component suggests that exciton trapping is no longer successful in

the n = 2 iodide system despite the influence of a rigid AIE spacer. In addition, the bromide-guided AIE systems provided additional evidence of dominant band-edge recombination in n = 2-type structures confirms in this case.

The emission in $BPCSA_2MAPb_2Br_7$ at ~520 nm is found to be ~4.5 ns, whereas $FPCSA_2MAPb_2Br_7$ exhibits a slightly shorter lifetime of ~3.3 ns at a similar wavelength. Such values are still in the nanosecond range and reflect efficient radiative recombination with limited contribution of the local states. The absence of a slow decay component once again indicates that self-trapped excitons are severely inhibited by the rigid lattice and weaker electron-phonon coupling of bromide-based systems. The comparison of n = 1 and n = 2 systems gives a vivid dimensionality effect on the dynamics of excitons. The results showed that n = 1 iodide PVSKs easily facilitate the generation of long-lived self-trapped excitons, and that n = 2 structures generally recombined more rapidly with less trapping, even with rigid AIE cations. The thicker inorganic slab seems to reduce lattice distortion and destabilize regions of local states, hence giving a more bandlike recombination behavior. Moreover, the presence of AIE cations extends the exciton lifetimes more than OA-based references, implying that lattice interaction induced by spacer is still a significant factor.

The optical structure and spectra of n = 2 double-layered PVSKs also demonstrate how the thickness of the inorganic slab alters light absorption, emission pathways, and general photophysical efficiency in AIE-based hybrid systems. UV–vis absorption spectra (see Figure 5.9A) reveal that all compositions retain the distinct excitonic characteristics of PVSKs with multilevels, although the spectral profiles become broader compared to the n = 1 versions. In the figure 5.9B the iodide-based $OA_2MAPb_2I_7$ has a sharp excitonic absorption characteristic in the ~560–580 nm region that is red shifted in comparison to n = 1 systems on the basis of the decreased quantum confinement in the thicker inorganic slab. The bromide derivative exhibits an analogous blue-shifted absorption edge in the region ~430–450 nm consistent with its larger bandgap. Upon incorporation of AIE cations, the absorption spectra are substantially extended over the UV region (300–400 nm) that corresponds to strong π–π^* transitions from conjugated organic spacers. Additionally, both BPCSA- and FPCSA-based systems demonstrate relatively higher peak absorption in the high-energy domain, which indicates that organic materials play an important part in light harvesting in the hybrid framework.

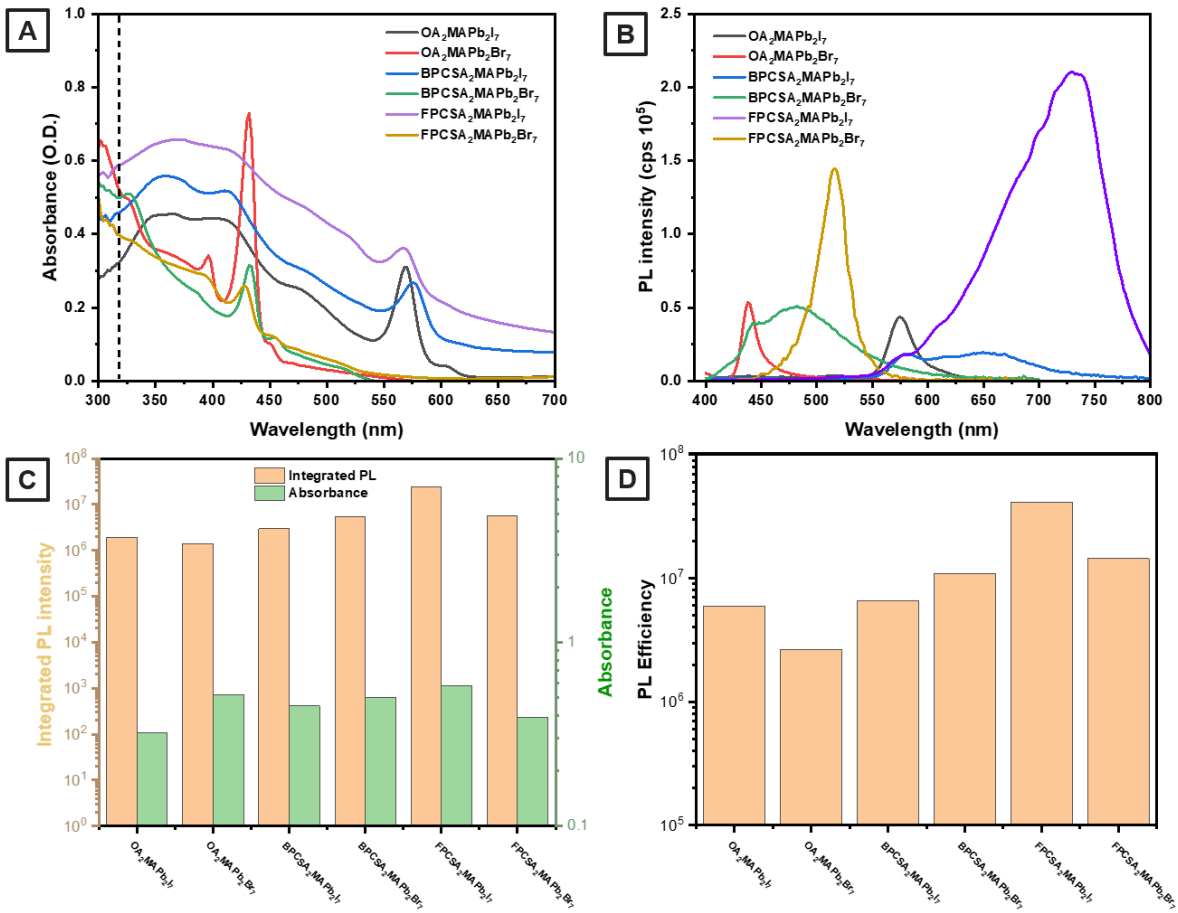

Figure 5.9. (A) – UV-vis absorbance spectra, (B) – PL emission spectra and (C) – ratio of Integrated PL to absorbace at 315nm and (D) – PL efficiency of OA-based n=2 PVSKs and AIE dye incorporated 2D perovskites.

Compared with the stationary conditions, PL spectra of the n = 2 systems show wider emission profiles and are much more complex, which indicates the increased diversity of recombination pathways. In comparison, the reference $OA_2MAPb_2I_7$ exhibits a relatively narrow emission that is centered around ~560 nm, which is attributable to band-edge free exciton recombination with reduced confinement. $BPCSA_2MAPb_2I_7$ shows a wider emission from ~500 to ~700 nm, which clearly implies band-edge emission and contributions arising from localized states. The system of $FPCSA_2MAPb_2I_7$ demonstrates a more prominent red-shifted and broader emission, with the predominant band extending in areas >~700 nm. This trend confirms that the thicker inorganic slab at n = 2 iodide systems still offers a high level of exciton–phonon coupling, which is reinforced by the modified electronic structure with FPCSA, ultimately favoring relaxation into lower energy emissive states, presumably resulting from charge transfer from FPCSA LUMO level to VB of Pb_2I_7. For the bromide-based n = 2 systems, emission behavior

varies significantly. $OA_2MAPb_2Br_7$ emission is of a distinct region near ~450 nm, consistent with a band-edge recombination in a wider bandgap. $BPCSA_2MAPb_2Br_7$ has a more open emission around ~470–520 nm, which suggests its state-partially localized but still dominated by band-edge process. In contrast, $FPCSA_2MAPb_2Br_7$ shows a unique emission peak around ~500–520 nm possessing a distinct high-intensity and a moderately wide spectral range, implying efficient radiative recombination with reduced self-trapping. The bromide analogues exhibit a much weaker long-wavelength emission compared to the iodide systems, attesting that the more rigid structure restricts exciton localization and favors direct recombination pathways.

To further evaluate the emissive properties of the n = 2 perovskites, the integrated PL intensity was normalized by the absorbance at the excitation wavelength (315 nm), and the resulting relative PL efficiencies are presented in Figures 5.9C and D. Although all AIE-based PVSKs have an increased absorption in the UV, owing to the organic spacers, the integrated PL intensities change depending upon halide content and cation species. Regarding the iodide-based n = 2 systems, $FPCSA_2MAPb_2I_7$ demonstrates the maximum relative PL efficiency and moderate absorbance, indicating ahighly efficient radiative recombination of the interfacial charge-transfer excitons formed in the type-II band alignment. A comparison was performed for the n = 2 layered perovskites, and the normalized PL efficiencies are summarized in Figures 5.9C and D. In contrast to the OA-based references, all AIE-incorporated perovskites exhibit higher relative PL efficiencies. $BPCSA_2MAPb_2Br_7$ shows approximately a 4-fold increase, while $FPCSA_2MAPb_2Br_7$ exhibits an approximately 5-fold enhancement compared with $OA_2MAPb_2Br_7$. More importantly, $FPCSA_2MAPb_2I_7$ displays the highest relative PL efficiency among all investigated samples, approximately 7-fold greater than $OA_2MAPb_2I_7$. The enhancement is consistent with the intense broad emission centered at ~720 nm, originating from efficient charge-transfer recombination enabled by the type-II band alignment. Even $BPCSA_2MAPb_2I_7$ exhibits a modest increase relative to the OA analogue demonstrating that replacing the conventional OA spacer with AIE-active organic cations substantially improves the radiative efficiency of n = 2 layered perovskites by enhancing exciton utilization and suppressing non-radiative losses. Individually, the differences in absorption and emission properties of n = 2 systems demonstrate the interactions of lower quantum confinement, halide-dependent lattice dynamics, and the design of organic spacer. These thicker inorganic layers cause red-shifted absorption and emission, while the selection of halide impacts the equilibrium between band-edge and self-trapped exciton recombination. At the same time, the

addition of AIE cations improves absorption and adds additional paths for energy relaxation. So the resulting quantum efficiency shows which processes are in competition, bromide-based systems prefer efficient radiative recombination, and iodide-based ones exhibit wider multi-channel emission. This result indicates a further degree of freedom for tuning spectral performance and emission efficiency with n = 2 PVSKs in hybrid AIE–PVSK materials. Previous layered-perovskite studies have shown that the intermolecular arrangement of chromophores within the organic layer can either quench emission or generate new aggregate and excimer states [152]. The use of AIE-active BPCSA and FPCSA provides an alternative strategy in which molecular aggregation is intended to restrict intramolecular motion and preserve solid-state emission. The enhanced relative PL efficiency of several AIE-incorporated compositions compared with their OA references supports the usefulness of this approach, although the final emission efficiency remains strongly dependent on band alignment and competing charge-transfer processes. Parts of this work presented in this chapter was published in the Internation Journal of Molecular Sciences [154]

CHAPTER 6: CONCLUSION

6.1. Results and significance

The integration of AIE active organic cations into both low-dimensional and quasi-two-dimensional perovskites has been the topic of extensive study in this thesis to define structure–property relationships regulating band alignment, interfacial coupling, as well as photophysical properties. Using two completely different AIE molecules, BPCSA and FPCSA, this work shows that molecular design, as well as perovskite dimensions and halide composition, are essential tools for optimization of exciton dynamics and emission parameters. For n = 1 two-dimensional perovskites, BPCSA provides type-I band conformation of PbI_4 in relation to its electron transport system, and the high rate of energy exchange and direct coupling of organic and inorganic components is favored. On the other hand, BPCSA exhibits a type-II alignment towards $PbBr_4$ due to its lower interfacial coupling. Due to its fluorinated geometry with deeper frontier orbitals, FPCSA always conforms to type-II with both PbI_4 and $PbBr_4$, which results in decreased energy transfer and better electronic decoupling. The differences directly map onto emission pathways, and BPCSA-based systems prefer perovskite-dominated emission, whereas FPCSA permits multiple emission channels. In n = 2 quasi-2D systems, the band alignment strongly correlates both to the molecular design of the structure and the halide composition. BPCSA has type-I alignment with Pb_2I_7 but type-II alignment with Pb_2Br_7, whereas FPCSA has type-I alignment with Pb_2I_7 and Pb_2Br_7. This change underlines that the interaction between the organic energy levels and inorganic band structure is paramount. In this new system, FPCSA sensitizes very well the Pb_2Br_7 framework, and hence, FPCSA produced a very small and greatly improved emission than the classical $OA_2MAPb_2Br_7$ system, demonstrating that optimal coupling leads to markedly enhanced radiative recombination efficiency. A study in photophysics indicates that such AIE cations are a key player in exciton generation and recombination processes. Notably $FPCSA_2MAPb_2I_7$ presents a distinctive emission band at about 720 nm that corresponds to charge-transfer emission between organic-inorganic materials owing to its nature. An important product of it, the broadband and tunable emissions and white light emission, is achieved. In contrast to most previously reported Type-II conjugated organic cation-incorporated perovskites, where spatial charge separation primarily results in photoluminescence quenching, the $FPCSA_2MAPb_2I_7$ system demonstrated intense broad charge-transfer emission while maintaining prolonged excited-state dynamics. This finding suggests that appropriate molecular design of AIE-active organic

cations enables Type-II heterojunctions that preserve radiative recombination, thereby extending the functionality of conjugated organic cation-incorporated perovskites beyond conventional charge-separation behavior and providing new opportunities for designing hybrid materials with tunable interfacial emission characteristics.It is worth noting that in Type-I heterostructures, efficient exciton confinement promotes strong radiative recombination, which is advantageous for high-brightness LEDs and low-threshold laser materials. In contrast, the Type-II band alignment demonstrated for the FPCSA-based perovskites facilitates interfacial charge transfer, resulting in broad, red-shifted charge-transfer emission extending beyond the intrinsic bandgap emission of the individual organic and inorganic components. Such long-wavelength emission provides an additional degree of freedom for tuning the photoluminescence toward the near-infrared spectral region, which is attractive for applications including NIR spectroscopy, integrated optical sensing, and telecommunications. Moreover, the photo-induced charge separation associated with the Type-II heterostructure may also facilitate charge extraction at interfaces with charge-transport layers, suggesting that the proposed molecular design strategy could be extended beyond light-emitting devices to other optoelectronic technologies, such as photovoltaic and photodetector devices.

6.2. Future work

Building upon the successful demonstration of AIE organic cation engineering in RP layered perovskites, future research will focus on extending this molecular design strategy to DJ quasi-two-dimensional perovskites for highly efficient near-infrared NIR quantum-cutting materials. Compared with RP perovskites, DJ structures possess diammonium spacers that connect adjacent inorganic layers through two ammonium groups, resulting in stronger interlayer interactions, improved structural rigidity, and enhanced environmental stability. These characteristics are expected to provide a more favorable platform for exciton confinement and energy transfer processes.

The proposed research strategy is illustrated in Figure 6.1. DJ spacer with AIE properties will be employed to synthesize n = 3 bromide perovskites, while Yb^{3+} ions will be incorporated into the inorganic framework as quantum-cutting centers. Upon ultraviolet excitation, AIE DJ spacer is expected to act as an efficient photosensitizer by harvesting excitation energy and

transferring it to the inorganic perovskite framework through favorable energy level alignment. The excited perovskite can subsequently sensitize Yb^{3+} ions through cooperative energy transfer, producing two NIR photons at approximately 980 nm from a single high-energy excitation event.

Preliminary experimental results demonstrate the feasibility of this approach. Yb-doped DJ perovskites exhibit visible emission centered at approximately 490 nm together with characteristic Yb^{3+} emission around 980 nm, confirming successful energy transfer from the perovskite host to the lanthanide ions. However, the NIR quantum-cutting emission remains relatively weak, indicating that the current energy-transfer efficiency is still limited. Future work will therefore concentrate on optimizing several key parameters, including spacers configuration, Yb^{3+} concentration, halide composition, and perovskite dimensionality, to maximize spectral overlap and suppress non-radiative recombination pathways. In addition, systematic photophysical investigations, including temperature-dependent photoluminescence, time-resolved spectroscopy, and absolute photoluminescence quantum yield measurements, will be performed to clarify the

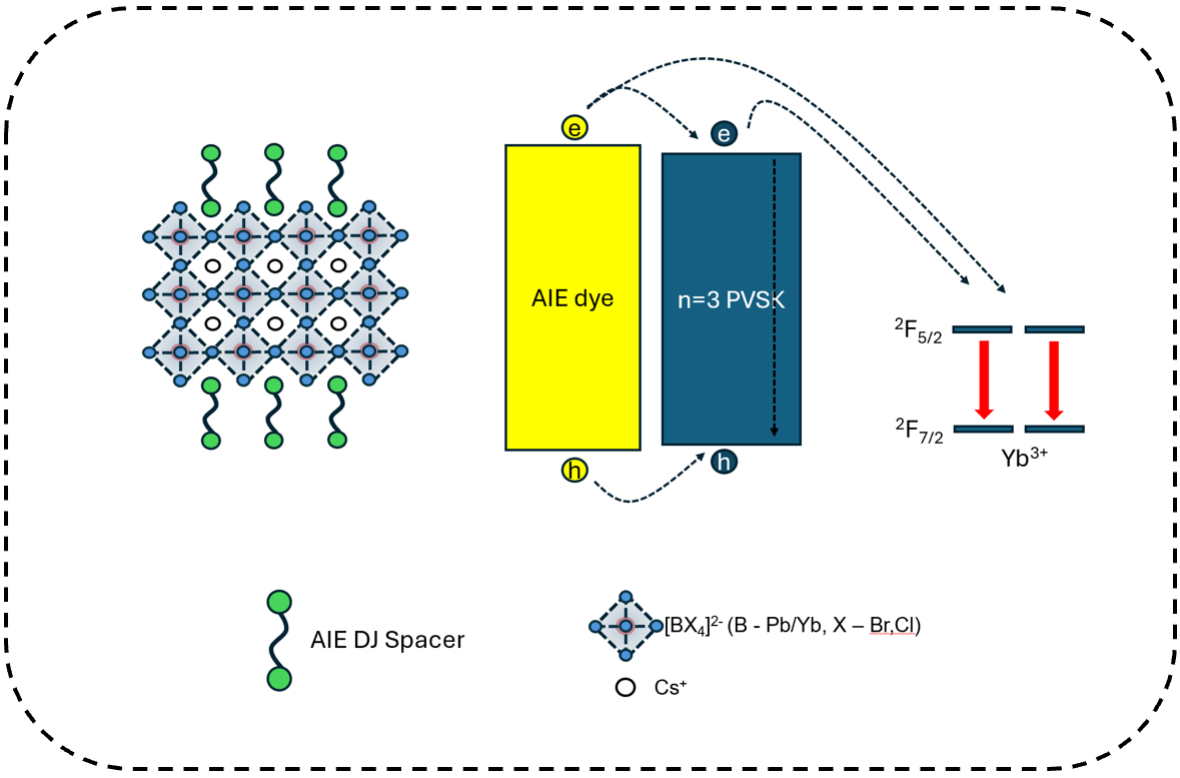

Figure 6.1. Schematic illustration of the proposed AIE DJ spacer-assisted energy transfer mechanism in Yb^{3+}-doped n = 3 DJ perovskites

energy-transfer mechanism and quantify the quantum-cutting efficiency. Successful implementation of this strategy is expected to establish AIE sensitization as an effective molecular

engineering approach for developing highly efficient NIR-emitting layered perovskites for wavelength conversion, optical sensing, telecommunications, and other photonic applications.

BIBLIOGRAPHY

[1] Kojima, A., Teshima, K., Shirai, Y., & Miyasaka, T. (2009). Organometal halide perovskites as Visible-Light sensitizers for photovoltaic cells. *Journal of the American Chemical Society*, *131*(17), 6050–6051. https://doi.org/10.1021/ja809598r

[2] Kim, H., Lee, C., Im, J., Lee, K., Moehl, T., Marchioro, A., Moon, S., Humphry-Baker, R., Yum, J., Moser, J. E., Grätzel, M., & Park, N. (2012). Lead Iodide Perovskite Sensitized All-Solid-State Submicron Thin Film Mesoscopic Solar Cell with Efficiency Exceeding 9%. *Scientific Reports*, *2*(1), 591. https://doi.org/10.1038/srep00591

[3] Green, M. A., Ho-Baillie, A., & Snaith, H. J. (2014). The emergence of perovskite solar cells. *Nature Photonics*, *8*(7), 506–514. https://doi.org/10.1038/nphoton.2014.134

[4] Cao, Y., Wang, N., Tian, H., Guo, J., Wei, Y., Chen, H., Miao, Y., Zou, W., Pan, K., He, Y., Cao, H., Ke, Y., Xu, M., Wang, Y., Yang, M., Du, K., Fu, Z., Kong, D., Dai, D., . . . Huang, W. (2018). Perovskite light-emitting diodes based on spontaneously formed submicrometre-scale structures. *Nature*, *562*(7726), 249–253. https://doi.org/10.1038/s41586-018-0576-2

[5] Deschler, F., Price, M., Pathak, S., Klintberg, L. E., Jarausch, D., Higler, R., Hüttner, S., Leijtens, T., Stranks, S. D., Snaith, H. J., Atatüre, M., Phillips, R. T., & Friend, R. H. (2014). High photoluminescence efficiency and optically pumped lasing in Solution-Processed mixed halide perovskite semiconductors. *The Journal of Physical Chemistry Letters*, *5*(8), 1421–1426. https://doi.org/10.1021/jz5005285

[6] Dong, Q., Fang, Y., Shao, Y., Mulligan, P., Qiu, J., Cao, L., & Huang, J. (2015). Electron-hole diffusion lengths > 175 μm in solution-grown CH 3 NH 3 PbI 3 single crystals. *Science*, *347*(6225), 967–970. https://doi.org/10.1126/science.aaa5760

[7] Fang, Y., & Huang, J. (2015). Resolving weak light of sub-picowatt per square centimeter by hybrid perovskite photodetectors enabled by noise reduction. *Advanced Materials*, *27*(17), 2804–2810. https://doi.org/10.1002/adma.201500099

[8] Lin, K., Xing, J., Quan, L. N., De Arquer, F. P. G., Gong, X., Lu, J., Xie, L., Zhao, W., Zhang, D., Yan, C., Li, W., Liu, X., Lu, Y., Kirman, J., Sargent, E. H., Xiong, Q., & Wei, Z. (2018). Perovskite light-emitting diodes with external quantum efficiency exceeding 20 per cent. *Nature*, *562*(7726), 245–248. https://doi.org/10.1038/s41586-018-0575-3

[9] Tan, Z., Moghaddam, R. S., Lai, M. L., Docampo, P., Higler, R., Deschler, F., Price, M., Sadhanala, A., Pazos, L. M., Credgington, D., Hanusch, F., Bein, T., Snaith, H. J., & Friend, R. H. (2014). Bright light-emitting diodes based on organometal halide perovskite. *Nature Nanotechnology*, *9*(9), 687–692. https://doi.org/10.1038/nnano.2014.149

[10] Xing, G., Mathews, N., Lim, S. S., Yantara, N., Liu, X., Sabba, D., Grätzel, M., Mhaisalkar, S., & Sum, T. C. (2014). Low-temperature solution-processed wavelength-tunable perovskites for lasing. *Nature Materials*, *13*(5), 476–480. https://doi.org/10.1038/nmat3911

[11] Zhou, H., Chen, Q., Li, G., Luo, S., Song, T., Duan, H., Hong, Z., You, J., Liu, Y., & Yang, Y. (2014). Interface engineering of highly efficient perovskite solar cells. *Science*, *345*(6196), 542–546. https://doi.org/10.1126/science.1254050

[12] Zhu, H., Fu, Y., Meng, F., Wu, X., Gong, Z., Ding, Q., Gustafsson, M. V., Trinh, M. T., Jin, S., & Zhu, X. (2015). Lead halide perovskite nanowire lasers with low lasing thresholds and high quality factors. *Nature Materials*, *14*(6), 636–642. https://doi.org/10.1038/nmat4271

[13] Stranks, S. D., & Snaith, H. J. (2015). Metal-halide perovskites for photovoltaic and light-emitting devices. *Nature Nanotechnology*, *10*(5), 391–402. https://doi.org/10.1038/nnano.2015.90

[14] Sutherland, B. R., & Sargent, E. H. (2016). Perovskite photonic sources. *Nature Photonics*, *10*(5), 295–302. https://doi.org/10.1038/nphoton.2016.62

[15] Møller, C. K. (1958). Crystal structure and photoconductivity of cæsium plumbohalides. *Nature*, *182*(4647), 1436. https://doi.org/10.1038/1821436a0

[16] Mitzi, D. B. (1999). Synthesis, structure, and properties of Organic-Inorganic Perovskites and related materials. *Progress in Inorganic Chemistry*, 1–121. https://doi.org/10.1002/9780470166499.ch1

[17] Hong, X., Ishihara, T., & Nurmikko, A. V. (1992). Dielectric confinement effect on excitons inPbI4-based layered semiconductors. *Physical Review. B, Condensed Matter*, *45*(12), 6961–6964. https://doi.org/10.1103/physrevb.45.6961

[18] Stranks, S. D., Eperon, G. E., Grancini, G., Menelaou, C., Alcocer, M. J. P., Leijtens, T., Herz, L. M., Petrozza, A., & Snaith, H. J. (2013). Electron-Hole diffusion lengths exceeding 1 micrometer in an organometal trihalide perovskite absorber. *Science*, *342*(6156), 341–344. https://doi.org/10.1126/science.1243982

[19] Xing, G., Mathews, N., Sun, S., Lim, S. S., Lam, Y. M., Grätzel, M., Mhaisalkar, S., & Sum, T. C. (2013). Long-Range balanced electron- and Hole-Transport lengths in Organic-Inorganic CH 3 NH 3 PBI 3. *Science*, *342*(6156), 344–347. https://doi.org/10.1126/science.1243167

[20] Wehrenfennig, C., Eperon, G. E., Johnston, M. B., Snaith, H. J., & Herz, L. M. (2013). High charge carrier mobilities and lifetimes in organolead trihalide perovskites. *Advanced Materials*, *26*(10), 1584–1589. https://doi.org/10.1002/adma.201305172

[21] Tan, Z., Moghaddam, R. S., Lai, M. L., Docampo, P., Higler, R., Deschler, F., Price, M., Sadhanala, A., Pazos, L. M., Credgington, D., Hanusch, F., Bein, T., Snaith, H. J., & Friend, R. H. (2014). Bright light-emitting diodes based on organometal halide perovskite. *Nature Nanotechnology*, *9*(9), 687–692. https://doi.org/10.1038/nnano.2014.149

[22] Yakunin, S., Sytnyk, M., Kriegner, D., Shrestha, S., Richter, M., Matt, G. J., Azimi, H., Brabec, C. J., Stangl, J., Kovalenko, M. V., & Heiss, W. (2015). Detection of X-ray photons by solution-processed lead halide perovskites. Nature Photonics, 9(7), 444–449. https://doi.org/10.1038/nphoton.2015.82

[23] Wei, W., Zhang, Y., Xu, Q., Wei, H., Fang, Y., Wang, Q., Deng, Y., Li, T., Gruverman, A., Cao, L., & Huang, J. (2017). Monolithic integration of hybrid perovskite single crystals with heterogenous substrate for highly sensitive X-ray imaging. *Nature Photonics*, *11*(5), 315–321. https://doi.org/10.1038/nphoton.2017.43

[24] Cao, Y., Wang, N., Tian, H., Guo, J., Wei, Y., Chen, H., Miao, Y., Zou, W., Pan, K., He, Y., Cao, H., Ke, Y., Xu, M., Wang, Y., Yang, M., Du, K., Fu, Z., Kong, D., Dai, D., . . . Huang, W. (2018). Perovskite light-emitting diodes based on spontaneously formed submicrometre-scale structures. *Nature*, *562*(7726), 249–253. https://doi.org/10.1038/s41586-018-0576-2

[25] Protesescu, L., Yakunin, S., Bodnarchuk, M. I., Krieg, F., Caputo, R., Hendon, C. H., Yang, R. X., Walsh, A., & Kovalenko, M. V. (2015). Nanocrystals of Cesium Lead Halide Perovskites (CsPbX3, X = Cl, Br, and I): Novel Optoelectronic Materials Showing Bright Emission with Wide Color Gamut. *Nano Letters*, *15*(6), 3692–3696. https://doi.org/10.1021/nl5048779

[26] Basiricò, L., Ciavatti, A., & Fraboni, B. (2020). Solution-Grown organic and Perovskite X-Ray Detectors: a new paradigm for the direct detection of ionizing radiation. Advanced Materials Technologies, 6(1). https://doi.org/10.1002/admt.202000475

[27] Kirschner, M. S., Diroll, B. T., Guo, P., Harvey, S. M., Helweh, W., Flanders, N. C., Brumberg, A., Watkins, N. E., Leonard, A. A., Evans, A. M., Wasielewski, M. R., Dichtel, W. R., Zhang, X., Chen, L. X., & Schaller, R. D. (2019). Photoinduced, reversible phase

[28] Green, M. A., Dunlop, E. D., Siefer, G., Yoshita, M., Kopidakis, N., Bothe, K., & Hao, X. (2022). Solar cell efficiency tables (Version 61). *Progress in Photovoltaics Research and Applications*, *31*(1), 3–16. https://doi.org/10.1002/pip.3646

[29] Al-Ashouri, A., Köhnen, E., Li, B., Magomedov, A., Hempel, H., Caprioglio, P., Márquez, J. A., Vilches, A. B. M., Kasparavicius, E., Smith, J. A., Phung, N., Menzel, D., Grischek, M., Kegelmann, L., Skroblin, D., Gollwitzer, C., Malinauskas, T., Jošt, M., Matič, G., . . . Albrecht, S. (2020). Monolithic perovskite/silicon tandem solar cell with >29% efficiency by enhanced hole extraction. *Science*, *370*(6522), 1300–1309. https://doi.org/10.1126/science.abd4016

[30] Lal, N. N., Dkhissi, Y., Li, W., Hou, Q., Cheng, Y., & Bach, U. (2017). Perovskite Tandem Solar cells. *Advanced Energy Materials*, *7*(18). https://doi.org/10.1002/aenm.201602761

[31] Dong, H., Ran, C., Gao, W., Li, M., Xia, Y., & Huang, W. (2023). Metal Halide Perovskite for next-generation optoelectronics: progresses and prospects. *eLight*, *3*(1). https://doi.org/10.1186/s43593-022-00033-z

[32] Saparov, B., & Mitzi, D. B. (2016). Organic–Inorganic perovskites: structural versatility for functional materials design. *Chemical Reviews*, *116*(7), 4558–4596. https://doi.org/10.1021/acs.chemrev.5b00715

[33] Stoumpos, C. C., & Kanatzidis, M. G. (2015). The renaissance of halide perovskites and their evolution as emerging semiconductors. *Accounts of Chemical Research*, *48*(10), 2791–2802. https://doi.org/10.1021/acs.accounts.5b00229

[34] Kulkarni, S. A., Yantara, N., Tan, K. S., Mathews, N., & Mhaisalkar, S. G. (2019). Perovskite nanostructures: Leveraging quantum effects to challenge optoelectronic limits. *Materials Today*, *33*, 122–140. https://doi.org/10.1016/j.mattod.2019.10.021

[35] Filip, M. R., & Giustino, F. (2014). GWquasiparticle band gap of the hybrid organic-inorganic perovskiteCH3NH3PbI3: Effect of spin-orbit interaction, semicore electrons, and self-consistency. *Physical Review B*, *90*(24). https://doi.org/10.1103/physrevb.90.245145

[36] Stranks, S. D., & Snaith, H. J. (2015). Metal-halide perovskites for photovoltaic and light-emitting devices. *Nature Nanotechnology*, *10*(5), 391–402. https://doi.org/10.1038/nnano.2015.90

[37] Yin, W., Shi, T., & Yan, Y. (2014). Unique properties of halide perovskites as possible origins of the superior solar cell performance. *Advanced Materials*, *26*(27), 4653–4658. https://doi.org/10.1002/adma.201306281

[38] Glazer, A. M. (1972). The classification of tilted octahedra in perovskites. *Acta Crystallographica Section B*, *28*(11), 3384–3392. https://doi.org/10.1107/s0567740872007976

[39] Marronnier, A., Roma, G., Boyer-Richard, S., Pedesseau, L., Jancu, J. M., Bonnassieux, Y., ... & Even, J. (2018). Anharmonicity and disorder in the black phases of cesium lead iodide used for stable inorganic perovskite solar cells. *ACS nano*, *12*(4), 3477-3486.

[40] Liu, S., Sun, S., Gan, C. K., Del Águila, A. G., Fang, Y., Xing, J., ... & Xiong, Q. (2019). Manipulating efficient light emission in two-dimensional perovskite crystals by pressure-induced anisotropic deformation. *Science advances*, *5*(7), eaav9445.

[41] Palazon, F., Almeida, G., Akkerman, Q. A., De Trizio, L., Dang, Z., Prato, M., & Manna, L. (2017). Changing the dimensionality of cesium lead bromide nanocrystals by reversible postsynthesis transformations with amines. *Chemistry of Materials*, *29*(10), 4167-4171.

[42] Hao, F., Stoumpos, C. C., Chang, R. P. H., & Kanatzidis, M. G. (2014). Anomalous band gap behavior in mixed SN and PB perovskites enables broadening of absorption spectrum in solar cells. *Journal of the American Chemical Society*, *136*(22), 8094–8099. https://doi.org/10.1021/ja5033259

[43] Song, J., Li, J., Li, X., Xu, L., Dong, Y., & Zeng, H. (2015). Quantum Dot Light-Emitting Diodes Based on Inorganic Perovskite Cesium Lead Halides (CsPbX3). *Advanced Materials (Deerfield Beach, Fla.)*, *27*(44), 7162-7167.

[44] Dong, H., Zhang, C., Liu, X., Yao, J., & Zhao, Y. S. (2020). Materials chemistry and engineering in metal halide perovskite lasers. *Chemical Society Reviews*, *49*(3), 951-982.

[45] Sutherland, B. R., Hoogland, S., Adachi, M. M., Wong, C. T., & Sargent, E. H. (2014). Conformal organohalide perovskites enable lasing on spherical resonators. *ACS nano*, *8*(10), 10947-10952.
[46] Wang, Y., Li, X., Song, J., Xiao, L., Zeng, H., & Sun, H. (2015). All-Inorganic Colloidal Perovskite Quantum Dots: A New Class of Lasing Materials with Favorable Characteristics. *Advanced Materials (Deerfield Beach, Fla.)*, *27*(44), 7101-7108.
[47] Chen, S., Roh, K., Lee, J., Chong, W. K., Lu, Y., Mathews, N., ... & Nurmikko, A. (2016). A photonic crystal laser from solution based organo-lead iodide perovskite thin films. *Acs Nano*, *10*(4), 3959-3967.
[48] Chen, S., & Nurmikko, A. (2017). Stable green perovskite vertical-cavity surface-emitting lasers on rigid and flexible substrates. *Acs Photonics*, *4*(10), 2486-2494.
[49] Katan, C., Mercier, N., & Even, J. (2019). Quantum and dielectric confinement effects in lower-dimensional hybrid perovskite semiconductors. *Chemical reviews*, *119*(5), 3140-3192.
[50] Wang, G., Mei, S., Liao, J., Wang, W., Tang, Y., Zhang, Q., ... & Xing, G. (2021). Advances of nonlinear photonics in low-dimensional halide perovskites. *Small*, *17*(43), 2100809. https://doi.org/10.1002/smll.202100809Digital Object Identifier (DOI)
[51] Yuan, M., Quan, L. N., Comin, R., Walters, G., Sabatini, R., Voznyy, O., Hoogland, S., Zhao, Y., Beauregard, E. M., Kanjanaboos, P., Lu, Z., Kim, D. H., & Sargent, E. H. (2016). Perovskite energy funnels for efficient light-emitting diodes. *Nature Nanotechnology*, *11*(10), 872–877. https://doi.org/10.1038/nnano.2016.110
[52] Zhang, L., Sun, C., He, T., Jiang, Y., Wei, J., Huang, Y., & Yuan, M. (2021). High-performance quasi-2D perovskite light-emitting diodes: from materials to devices. *Light Science & Applications*, *10*(1), 61. https://doi.org/10.1038/s41377-021-00501-0
[53] Quan, L. N., De Arquer, F. P. G., Sabatini, R. P., & Sargent, E. H. (2018). Perovskites for light emission. *Advanced Materials*, *30*(45), e1801996. https://doi.org/10.1002/adma.201801996
[54] Fu, Y., Zhu, H., Chen, J., Hautzinger, M. P., Zhu, X., & Jin, S. (2019). Metal halide perovskite nanostructures for optoelectronic applications and the study of physical properties. *Nature Reviews Materials*, *4*(3), 169–188. https://doi.org/10.1038/s41578-019-0080-9
[55] Blancon, J., Stier, A. V., Tsai, H., Nie, W., Stoumpos, C. C., Traoré, B., Pedesseau, L., Kepenekian, M., Katsutani, F., Noe, G. T., Kono, J., Tretiak, S., Crooker, S. A., Katan, C., Kanatzidis, M. G., Crochet, J. J., Even, J., & Mohite, A. D. (2018). Scaling law for excitons in 2D perovskite quantum wells. *Nature Communications*, *9*(1), 2254. https://doi.org/10.1038/s41467-018-04659-x

[56] Quan, L. N., Yuan, M., Comin, R., Voznyy, O., Beauregard, E. M., Hoogland, S., ... & Sargent, E. H. (2016). Ligand-stabilized reduced-dimensionality perovskites. *Journal of the American Chemical Society*, *138*(8), 2649-2655.
[57] Yuan, M., Quan, L. N., Comin, R., Walters, G., Sabatini, R., Voznyy, O., ... & Sargent, E. H. (2016). Perovskite energy funnels for efficient light-emitting diodes. *Nature nanotechnology*, *11*(10), 872-877.
[58] Grancini, G., Roldán-Carmona, C., Zimmermann, I., Mosconi, E., Lee, X., Martineau, D., ... & Nazeeruddin, M. K. (2017). One-Year stable perovskite solar cells by 2D/3D interface engineering. *Nature communications*, *8*(1), 15684.
[59] Jeon, N. J., Noh, J. H., Yang, W. S., Kim, Y. C., Ryu, S., Seo, J., & Seok, S. I. (2015). Compositional engineering of perovskite materials for high-performance solar cells. *Nature*, *517*(7535), 476-480. https://doi.org/10.1038/nature14133

[60] Xiao, Z., Dong, Q., Bi, C., Shao, Y., Yuan, Y., & Huang, J. (2014). Solvent annealing of Perovskite-Induced crystal growth for Photovoltaic-Device efficiency enhancement. *Advanced Materials*, *26*(37), 6503–6509. https://doi.org/10.1002/adma.201401685

[61] Li, X., Bi, D., Yi, C., Décoppet, J., Luo, J., Zakeeruddin, S. M., Hagfeldt, A., & Grätzel, M. (2016). A vacuum flash–assisted solution process for high-efficiency large-area perovskite solar cells. *Science*, *353*(6294), 58–62. https://doi.org/10.1126/science.aaf8060

[62] Ahn, N., Son, D., Jang, I., Kang, S. M., Choi, M., & Park, N. (2015). Highly Reproducible Perovskite Solar Cells with Average Efficiency of 18.3% and Best Efficiency of 19.7% Fabricated via Lewis Base Adduct of Lead(II) Iodide. *Journal of the American Chemical Society*, *137*(27), 8696–8699. https://doi.org/10.1021/jacs.5b04930

[63] Deng, Y., Zheng, X., Bai, Y., Wang, Q., Zhao, J., & Huang, J. (2018). Surfactant-controlled ink drying enables high-speed deposition of perovskite films for efficient photovoltaic modules. *Nature Energy*, *3*(7), 560–566. https://doi.org/10.1038/s41560-018-0153-9

[64] Razza, S., Di Giacomo, F., Matteocci, F., Cinà, L., Palma, A. L., Casaluci, S., ... & Di Carlo, A. (2015). Perovskite solar cells and large area modules (100 cm2) based on an air flow-assisted PbI2 blade coating deposition process. *Journal of Power Sources*, *277*, 286-291. https://doi.org/10.1016/j.jpowsour.2014.12.008

[65] Chen, K., Schünemann, S., Song, S., & Tüysüz, H. (2018). Structural effects on optoelectronic properties of halide perovskites. *Chemical Society Reviews*, *47*(18), 7045-7077. https://doi.org/10.1039/C8CS00212F

[66] Islam, M. R., Wu, Y., Liu, K., Wang, Z., Wang, Z., Qu, S., Wang, Z., & Wang, Z. (2022). Recent progress and future prospects for light management of All-Perovskite tandem solar cells. *Advanced Materials Interfaces*, *9*(4). https://doi.org/10.1002/admi.202101144

[67] Xiao, H., Li, R., Cai, W., & Zang, Z. (2024). Development of Quasi-Two-Dimensional perovskites and their application in Light-Emitting diodes. *Inorganic Chemistry*, *63*(6), 2853–2876. https://doi.org/10.1021/acs.inorgchem.3c03375

[68] Shockley, W., & Read, W. T. (1952). Statistics of the recombinations of holes and electrons. *Physical Review*, *87*(5), 835–842. https://doi.org/10.1103/physrev.87.835

[69] De Quilettes, D. W., Vorpahl, S. M., Stranks, S. D., Nagaoka, H., Eperon, G. E., Ziffer, M. E., Snaith, H. J., & Ginger, D. S. (2015). Impact of microstructure on local carrier lifetime in perovskite solar cells. *Science*, *348*(6235), 683–686. https://doi.org/10.1126/science.aaa5333

[70] Herz, L. M. (2016). Charge-Carrier dynamics in Organic-Inorganic Metal halide Perovskites. *Annual Review of Physical Chemistry*, *67*(1), 65–89. https://doi.org/10.1146/annurev-physchem-040215-112222

[71] Smith, M. D., & Karunadasa, H. I. (2018). White-light emission from layered halide perovskites. *Accounts of chemical research*, *51*(3), 619-627. https://doi.org/10.1021/acs.accounts.7b00433

[72] Tsai, H., Nie, W., Blancon, J., Stoumpos, C. C., Asadpour, R., Harutyunyan, B., Neukirch, A. J., Verduzco, R., Crochet, J. J., Tretiak, S., Pedesseau, L., Even, J., Alam, M. A., Gupta, G., Lou, J., Ajayan, P. M., Bedzyk, M. J., Kanatzidis, M. G., & Mohite, A. D. (2016). High-efficiency two-dimensional Ruddlesden–Popper perovskite solar cells. *Nature*, *536*(7616), 312–316. https://doi.org/10.1038/nature18306

[73] Spanopoulos, I., Hadar, I., Ke, W., Tu, Q., Chen, M., Tsai, H., ... & Kanatzidis, M. G. (2019). Uniaxial expansion of the 2D Ruddlesden–Popper perovskite family for improved environmental stability. *Journal of the American Chemical Society*, *141*(13), 5518-5534.

[74] Wang, Z., Lin, Q., Chmiel, F. P., Sakai, N., Herz, L. M., & Snaith, H. J. (2017). Efficient ambient-air-stable solar cells with 2D–3D heterostructured butylammonium-caesium-formamidinium lead halide perovskites. *Nature Energy*, *2*(9). https://doi.org/10.1038/nenergy.2017.135

[75] Li, D., Xing, Z., Huang, L., Meng, X., Hu, X., Hu, T., & Chen, Y. (2021). Spontaneous formation of upper gradient 2D structure for efficient and stable quasi-2D perovskites. *Advanced Materials*, *33*(34), 2101823. https://doi.org/10.1002/adma.202101823

[76] Xiao, Z., Zhao, L., Tran, N. L., Lin, Y. L., Silver, S. H., Kerner, R. A., Yao, N., Kahn, A., Scholes, G. D., & Rand, B. P. (2017). Mixed-Halide Perovskites with Stabilized Bandgaps. *Nano Letters*, *17*(11), 6863–6869. https://doi.org/10.1021/acs.nanolett.7b03179

[77] Udalova, N. N., Fateev, S. A., Nemygina, E. M., Zanetta, A., Grancini, G., Goodilin, E. A., & Tarasov, A. B. (2021). Nonmonotonic photostability of BA2MAN–1PBNI3N+1 homologous layered perovskites. *ACS Applied Materials & Interfaces*, *14*(1), 961–970. https://doi.org/10.1021/acsami.1c20043

[78] Kubicki, D. J., Prochowicz, D., Hofstetter, A., Péchy, P., Zakeeruddin, S. M., Grätzel, M., & Emsley, L. (2017). Cation Dynamics in Mixed-Cation (MA)x(FA)1–xPbI3 Hybrid Perovskites from Solid-State NMR. *Journal of the American Chemical Society*, *139*(29), 10055–10061. https://doi.org/10.1021/jacs.7b04930

[79] Philippe, B., Saliba, M., Correa-Baena, J., Cappel, U. B., Turren-Cruz, S., Grätzel, M., Hagfeldt, A., & Rensmo, H. (2017). Chemical distribution of multiple cation (RB+, CS+, MA+, and FA+) perovskite materials by photoelectron spectroscopy. *Chemistry of Materials*, *29*(8), 3589–3596. https://doi.org/10.1021/acs.chemmater.7b00126

[80] Gao, L., Spanopoulos, I., Ke, W., Huang, S., Hadar, I., Chen, L., Li, X., Yang, G., & Kanatzidis, M. G. (2019). Improved environmental stability and solar cell efficiency of (MA,FA)PBI3 perovskite using a Wide-Band-Gap 1D thiazolium Lead Iodide capping Layer strategy. *ACS Energy Letters*, *4*(7), 1763–1769. https://doi.org/10.1021/acsenergylett.9b00930

[81] Jiang, Y., Qin, C., Cui, M., He, T., Liu, K., Huang, Y., Luo, M., Zhang, L., Xu, H., Li, S., Wei, J., Liu, Z., Wang, H., Kim, G., Yuan, M., & Chen, J. (2019). Spectra stable blue perovskite light-emitting diodes. *Nature Communications*, *10*(1), 1868. https://doi.org/10.1038/s41467-019-09794-7

[82] Chu, Z., Zhao, Y., Ma, F., Zhang, C., Deng, H., Gao, F., Ye, Q., Meng, J., Yin, Z., Zhang, X., & You, J. (2020). Large cation ethylammonium incorporated perovskite for efficient and spectra stable blue light-emitting diodes. *Nature Communications*, *11*(1), 4165. https://doi.org/10.1038/s41467-020-17943-6

[83] Yu, X., Liu, T., Wei, Q., Liang, C., Wang, K., Guo, J., Zhao, D., Wang, B., Chen, R., & Xing, G. (2020). Tailoring the surface morphology and phase distribution for efficient perovskite electroluminescence. *The Journal of Physical Chemistry Letters*, *11*(15), 5877–5882. https://doi.org/10.1021/acs.jpclett.0c01252

[84] Wang, K., Peng, Y., Ge, J., Jiang, S., Zhu, B., Yao, J., Yin, Y., Yang, J., Zhang, Q., & Yao, H. (2018). Efficient and Color-Tunable QuASI-2D CSPBBRXCL3–X Perovskite Blue Light-Emitting diodes. *ACS Photonics*, *6*(3), 667–676. https://doi.org/10.1021/acsphotonics.8b01490

[85] Ma, D., Lin, K., Dong, Y., Choubisa, H., Proppe, A. H., Wu, D., Wang, Y., Chen, B., Li, P., Fan, J. Z., Yuan, F., Johnston, A., Liu, Y., Kang, Y., Lu, Z., Wei, Z., & Sargent, E. H. (2021). Distribution control enables efficient reduced-dimensional perovskite LEDs. Nature, 599(7886), 594–598. https://doi.org/10.1038/s41586-021-03997-z

[86] Kong, L., Zhang, X., Li, Y., Wang, H., Jiang, Y., Wang, S., You, M., Zhang, C., Zhang, T., Kershaw, S. V., Zheng, W., Yang, Y., Lin, Q., Yuan, M., Rogach, A. L., & Yang, X. (2021). Smoothing the energy transfer pathway in quasi-2D perovskite films using methanesulfonate leads to highly efficient light-emitting devices. *Nature Communications*, *12*(1), 1246. https://doi.org/10.1038/s41467-021-21522-8

[87] Smith, M. D., Connor, B. A., & Karunadasa, H. I. (2019). Tuning the luminescence of layered halide perovskites. *Chemical Reviews*, *119*(5), 3104-3139. https://doi.org/10.1021/acs.chemrev.8b00477

[88] Dou, L., Wong, A. B., Yu, Y., Lai, M., Kornienko, N., Eaton, S. W., ... & Yang, P. (2015). Atomically thin two-dimensional organic-inorganic hybrid perovskites. *Science*, *349*(6255), 1518-1521. DOI: 10.1126/science.aac7660

[89] Straus, D. B., & Kagan, C. R. (2018). Electrons, excitons, and phonons in two-dimensional hybrid perovskites: connecting structural, optical, and electronic properties. The journal of physical chemistry letters, 9(6), 1434-1447. https://doi.org/10.1021/acs.jpclett.8b00201

[90] Ishihara, T. (1994). Optical properties of PbI-based perovskite structures. *Journal of luminescence*, *60*, 269-274. https://doi.org/10.1016/0022-2313(94)90145-7

[91] Liao, Y., Liu, H., Zhou, W., Yang, D., Shang, Y., Shi, Z., ... & Ning, Z. (2017). Highly oriented low-dimensional tin halide perovskites with enhanced stability and photovoltaic performance. *Journal of the American Chemical Society*, *139*(19), 6693-6699. https://doi.org/10.1021/jacs.7b01815

[92] Meng, F., Liu, X., Chen, Y., Cai, X., Li, M., Shi, T., Chen, Z., Chen, D., Yip, H., Ramanan, C., Blom, P. W. M., & Su, S. (2020). Co-Interlayer Engineering toward Efficient Green Quasi-Two-Dimensional Perovskite Light-Emitting Diodes. *Advanced Functional Materials*, *30*(19). https://doi.org/10.1002/adfm.201910167

[93] Ren, Z., Yu, J., Qin, Z., Wang, J., Sun, J., Chan, C. C. S., Ding, S., Wang, K., Chen, R., Wong, K. S., Lu, X., Yin, W., & Choy, W. C. H. (2020). High-Performance Blue Perovskite Light-Emitting Diodes Enabled by Efficient Energy Transfer between Coupled Quasi-2D Perovskite Layers. *Advanced Materials*, *33*(1), e2005570. https://doi.org/10.1002/adma.202005570

[94] Kepenekian, M., & Even, J. (2017). Rashba and Dresselhaus couplings in halide perovskites: Accomplishments and opportunities for spintronics and spin–orbitronics. *The Journal of Physical Chemistry Letters*, *8*(14), 3362-3370. https://doi.org/10.1021/acs.jpclett.7b01015

[95] Ishihara, T., Takahashi, J., & Goto, T. (1989). Exciton state in two-dimensional perovskite semiconductor (C10H21NH3) 2PbI4. *Solid state communications*, *69*(9), 933-936. https://doi.org/10.1016/0038-1098(89)90935-6

[96] Wang, K., Park, J. Y., Akriti, & Dou, L. (2021). Two-dimensional halide perovskite quantum-well emitters: A critical review. *EcoMat*, *3*(3). https://doi.org/10.1002/eom2.12104

[97] Roy, C. R. (2024). *Heterostructures and Hyperspectral Microscopy of Lead Halide Perovskite Semiconductors*. The University of Wisconsin-Madison.

[98] Li, X., Hoffman, J. M., & Kanatzidis, M. G. (2021). The 2D Halide Perovskite Rulebook: How the Spacer Influences Everything from the Structure to Optoelectronic Device Efficiency. *Chemical Reviews*, *121*(4), 2230–2291. https://doi.org/10.1021/acs.chemrev.0c01006

[99] Zhang, F., Lu, H., Tong, J., Berry, J. J., Beard, M. C., & Zhu, K. (2020). Advances in two-dimensional organic–inorganic hybrid perovskites. *Energy & Environmental Science*, *13*(4), 1154–1186. https://doi.org/10.1039/c9ee03757h

[100] Du, K., Tu, Q., Zhang, X., Han, Q., Liu, J., Zauscher, S., & Mitzi, D. B. (2017). Two-Dimensional Lead(II) Halide-Based hybrid perovskites templated by acene alkylamines: crystal structures, optical properties, and piezoelectricity. *Inorganic Chemistry*, *56*(15), 9291–9302. https://doi.org/10.1021/acs.inorgchem.7b01094

[101] Era, M., Maeda, K., & Tsutsui, T. (1998). Enhanced phosphorescence from naphthalene-chromophore incorporated into lead bromide-based layered perovskite having organic–inorganic superlattice structure. *Chemical Physics Letters*, *296*(3–4), 417–420. https://doi.org/10.1016/s0009-2614(98)01028-8

[102] Gao, Y., Shi, E., Deng, S., Shiring, S. B., Snaider, J. M., Liang, C., Yuan, B., Song, R., Janke, S. M., Liebman-Peláez, A., Yoo, P., Zeller, M., Boudouris, B. W., Liao, P., Zhu, C., Blum, V., Yu, Y., Savoie, B. M., Huang, L., & Dou, L. (2019). Molecular engineering of organic–inorganic hybrid perovskites quantum wells. *Nature Chemistry*, *11*(12), 1151–1157. https://doi.org/10.1038/s41557-019-0354-2

[103] Jana, M. K., Liu, C., Lidin, S., Dirkes, D. J., You, W., Blum, V., & Mitzi, D. B. (2019). Resolving rotational stacking disorder and electronic level alignment in a 2D Oligothiophene-Based lead iodide perovskite. *Chemistry of Materials*, *31*(20), 8523–8532. https://doi.org/10.1021/acs.chemmater.9b03208

[104] Hu, H., Zhao, D., Gao, Y., Qiao, X., Salim, T., Chen, B., Chia, E. E. M., Grimsdale, A. C., & Lam, Y. M. (2019). Harvesting triplet excitons in Lead-Halide perovskites for Room-Temperature phosphorescence. *Chemistry of Materials*, *31*(7), 2597–2602. https://doi.org/10.1021/acs.chemmater.9b00315

[105] Zhao, R., Sabatini, R. P., Zhu, T., Wang, S., Najjarian, A. M., Johnston, A., Lough, A. J., Hoogland, S., Sargent, E. H., & Seferos, D. S. (2021). Rigid Conjugated diamine templates for stable Dion–Jacobson-Type Two-Dimensional perovskites. *Journal of the American Chemical Society*, *143*(47), 19901–19908. https://doi.org/10.1021/jacs.1c09515

[106] Park, I., Chu, L., Leng, K., Choy, Y. F., Liu, W., Abdelwahab, I., Zhu, Z., Ma, Z., Chen, W., Xu, Q., Eda, G., & Loh, K. P. (2019). Highly stable Two-Dimensional TIN(II) iodide hybrid Organic–Inorganic perovskite based on stilbene derivative. *Advanced Functional Materials*, *29*(39). https://doi.org/10.1002/adfm.201904810

[107] Sasai, R., & Shinomura, H. (2012). Preparation and optical characteristics of layered perovskite-type lead-bromide-incorporated azobenzene chromophores. *Journal of Solid State Chemistry*, *198*, 452–458. https://doi.org/10.1016/j.jssc.2012.11.009

[108] Fillafer, N., Seewald, T., Schmidt-Mende, L., & Polarz, S. (2020). Interfacial charge transfer processes in 2D and 3D semiconducting hybrid perovskites: azobenzene as photoswitchable ligand. *Beilstein Journal of Nanotechnology*, *11*, 466–479. https://doi.org/10.3762/bjnano.11.38

[109] Wang, K., Lin, Z., Zhang, Z., Jin, L., Ma, K., Coffey, A. H., Atapattu, H. R., Gao, Y., Park, J. Y., Wei, Z., Finkenauer, B. P., Zhu, C., Meng, X., Chowdhury, S. N., Chen, Z., Terlier, T., Do, T., Yao, Y., Graham, K. R., . . . Dou, L. (2023). Suppressing phase disproportionation in quasi-2D perovskite light-emitting diodes. *Nature Communications*, *14*(1), 397. https://doi.org/10.1038/s41467-023-36118-7

[110] Jemli, K., Audebert, P., Galmiche, L., Trippé-Allard, G., Garrot, D., Lauret, J., & Deleporte, E. (2015). Two-Dimensional Perovskite Activation with an Organic Luminophore. *ACS Applied Materials & Interfaces*, *7*(39), 21763–21769. https://doi.org/10.1021/acsami.5b05279

[111] Hu, H., Meier, F., Zhao, D., Abe, Y., Gao, Y., Chen, B., Salim, T., Chia, E. E. M., Qiao, X., Deibel, C., & Lam, Y. M. (2018). Efficient Room-Temperature Phosphorescence from Organic–Inorganic Hybrid Perovskites by Molecular Engineering. *Advanced Materials*, *30*(36), e1707621. https://doi.org/10.1002/adma.201707621

[112] Yang, S., Wu, D., Gong, W., Huang, Q., Zhen, H., Ling, Q., & Lin, Z. (2018). Highly efficient room-temperature phosphorescence and afterglow luminescence from common organic fluorophores in 2D hybrid perovskites. *Chemical Science*, *9*(48), 8975–8981. https://doi.org/10.1039/c8sc03563f

[113] Huang, Q., Lin, Z., & Yan, D. (2021). Tuning Organic Room-Temperature Phosphorescence through the Confinement Effect of Inorganic Micro/Nanostructures. *Small Structures*, *2*(9). https://doi.org/10.1002/sstr.202100044

[114] Gao, Y., Wei, Z., Yoo, P., Shi, E., Zeller, M., Zhu, C., Liao, P., & Dou, L. (2019). Highly stable Lead-Free perovskite Field-Effect transistors incorporating linear Π-Conjugated organic ligands. *Journal of the American Chemical Society*, *141*(39), 15577–15585. https://doi.org/10.1021/jacs.9b06276

[115] Hsu, S., Zhao, W., Gao, Y., Akriti, Segovia, M., Xu, X., Boudouris, B. W., & Dou, L. (2021). Thermoelectric performance of Lead-Free Two-Dimensional halide perovskites featuring conjugated ligands. *Nano Letters*, *21*(18), 7839–7844. https://doi.org/10.1021/acs.nanolett.1c02890

[116] Ma, K., Atapattu, H. R., Zhao, Q., Gao, Y., Finkenauer, B. P., Wang, K., Chen, K., Park, S. M., Coffey, A. H., Zhu, C., Huang, L., Graham, K. R., Mei, J., & Dou, L. (2021). Multifunctional conjugated ligand engineering for stable and efficient perovskite solar cells. *Advanced Materials*, *33*(32), e2100791. https://doi.org/10.1002/adma.202100791

[117] Wang, K., Jin, L., Gao, Y., Liang, A., Finkenauer, B. P., Zhao, W., Wei, Z., Zhu, C., Guo, T., Huang, L., & Dou, L. (2021). Lead-Free Organic–Perovskite hybrid quantum wells for highly stable Light-Emitting diodes. *ACS Nano*, *15*(4), 6316–6325. https://doi.org/10.1021/acsnano.1c00872

[118] Liang, A., Gao, Y., Asadpour, R., Wei, Z., Finkenauer, B. P., Jin, L., Yang, J., Wang, K., Chen, K., Liao, P., Zhu, C., Huang, L., Boudouris, B. W., Alam, M. A., & Dou, L. (2021). Ligand-Driven grain engineering of high mobility Two-Dimensional perovskite Thin-Film transistors. *Journal of the American Chemical Society*, *143*(37), 15215–15223. https://doi.org/10.1021/jacs.1c06337

[119] Wei, Z., Wang, K., Zhao, W., Gao, Y., Hu, Q., Chen, K., & Dou, L. (2021). A selenophene-containing conjugated organic ligand for two-dimensional halide perovskites. *Chemical Communications*, *57*(87), 11469–11472. https://doi.org/10.1039/d1cc04679a

[120] Takeoka, Y., Asai, K., Rikukawa, M., & Sanui, K. (2001). Incorporation of conjugated polydiacetylene systems into organic–inorganic quantum-well structures. *Chemical Communications*, *24*, 2592–2593. https://doi.org/10.1039/b108536k

[121] Era, M., Yoneda, S., Sano, T., & Noto, M. (2003). Preparation of amphiphilic poly(thiophene)s and their application for the construction of organic–inorganic superlattices. *Thin Solid Films*, *438–439*, 322–325. https://doi.org/10.1016/s0040-6090(03)00738-7

[122] Isikgor, F. H., Reddy, C. D., Li, M., Coskun, H., Li, B., Zhang, Y., Pennycook, S. J., & Ouyang, J. (2018). Self-assembled atomically thin hybrid conjugated polymer perovskites with

two-dimensional structure. *Journal of Materials Chemistry C*, *6*(31), 8405–8410. https://doi.org/10.1039/c8tc02548g

[123] Ortiz-Cervantes, C., Román-Román, P. I., Vazquez-Chavez, J., Hernández-Rodríguez, M., & Solis-Ibarra, D. (2018). Thousand-fold conductivity increase in 2D perovskites by polydiacetylene incorporation and doping. *Angewandte Chemie*, *130*(42), 14078–14082. https://doi.org/10.1002/ange.201809028

[124] Chen, W., Shi, Y., Chen, J., Ma, P., Fang, Z., Ye, D., Lu, Y., Yuan, Y., Zhao, J., & Xiao, Z. (2021). Polymerized Hybrid Perovskites with Enhanced Stability, Flexibility, and Lattice Rigidity. *Advanced Materials*, *33*(48), e2104842. https://doi.org/10.1002/adma.202104842

[125] Liang, A., Ma, K., Gao, Y., & Dou, L. (2022). Tailoring anchoring groups in Low-Dimensional Organic Semiconductor-Incorporated perovskites. *Small Structures*, *3*(3). https://doi.org/10.1002/sstr.202100173

[126] Deng, S., Shi, E., Yuan, L., Jin, L., Dou, L., & Huang, L. (2020). Long-range exciton transport and slow annihilation in two-dimensional hybrid perovskites. *Nature Communications*, *11*(1), 664. https://doi.org/10.1038/s41467-020-14403-z

[127] Tanaka, K., Sano, F., Takahashi, T., Kondo, T., Ito, R., & Ema, K. (2002). Two-dimensional Wannier excitons in a layered-perovskite-type crystal (C6H13NH3)2PbI4. *Solid State Communications*, *122*(5), 249–252. https://doi.org/10.1016/s0038-1098(02)00126-6

[128] Goyal, A., McKechnie, S., Pashov, D., Tumas, W., Van Schilfgaarde, M., & Stevanović, V. (2018). Origin of pronounced nonlinear band gap behavior in Lead–Tin hybrid perovskite alloys. *Chemistry of Materials*, *30*(11), 3920–3928. https://doi.org/10.1021/acs.chemmater.8b01695

[129] Liu, C., Huhn, W., Du, K., Vazquez-Mayagoitia, A., Dirkes, D., You, W., Kanai, Y., Mitzi, D. B., & Blum, V. (2018). Tunable Semiconductors: Control over Carrier States and Excitations in Layered Hybrid Organic-Inorganic Perovskites. *Physical Review Letters*, *121*(14), 146401. https://doi.org/10.1103/physrevlett.121.146401

[130] Passarelli, J. V., Fairfield, D. J., Sather, N. A., Hendricks, M. P., Sai, H., Stern, C. L., & Stupp, S. I. (2018). Enhanced Out-of-Plane Conductivity and Photovoltaic Performance in n = 1 Layered Perovskites through Organic Cation Design. *Journal of the American Chemical Society*, *140*(23), 7313–7323. https://doi.org/10.1021/jacs.8b03659

[131] Zhang, F., Park, S. Y., Yao, C., Lu, H., Dunfield, S. P., Xiao, C., Uličná, S., Zhao, X., Du Hill, L., Chen, X., Wang, X., Mundt, L. E., Stone, K. H., Schelhas, L. T., Teeter, G., Parkin, S., Ratcliff, E. L., Loo, Y., Berry, J. J., . . . Zhu, K. (2022). Metastable Dion-Jacobson 2D structure enables efficient and stable perovskite solar cells. *Science*, *375*(6576), 71–76. https://doi.org/10.1126/science.abj2637

[132] Zhang, F., Kim, D. H., Lu, H., Park, J., Larson, B. W., Hu, J., Gao, L., Xiao, C., Reid, O. G., Chen, X., Zhao, Q., Ndione, P. F., Berry, J. J., You, W., Walsh, A., Beard, M. C., & Zhu, K.

(2019). Enhanced charge transport in 2D perovskites via fluorination of organic cation. *Journal of the American Chemical Society*, *141*(14), 5972–5979. https://doi.org/10.1021/jacs.9b00972

[133] Jiang, Q., Tong, J., Xian, Y., Kerner, R. A., Dunfield, S. P., Xiao, C., Scheidt, R. A., Kuciauskas, D., Wang, X., Hautzinger, M. P., Tirawat, R., Beard, M. C., Fenning, D. P., Berry, J. J., Larson, B. W., Yan, Y., & Zhu, K. (2022). Surface reaction for efficient and stable inverted perovskite solar cells. *Nature*, *611*(7935), 278–283. https://doi.org/10.1038/s41586-022-05268-x

[134] Gélvez-Rueda, M. C., Fridriksson, M. B., Dubey, R. K., Jager, W. F., Van Der Stam, W., & Grozema, F. C. (2020). Overcoming the exciton binding energy in two-dimensional perovskite nanoplatelets by attachment of conjugated organic chromophores. *Nature Communications*, *11*(1), 1901. https://doi.org/10.1038/s41467-020-15869-7

[135] Förster, T., & Kasper, K. (1954). Z. Phys. Chem.(Munich). *Z. Phys. Chem.(Munich)*, *1*, 275.
[136] Birks, J. B. (1970). Photophysics of aromatic molecules. *(No Title)*.
[137] Luo, J., Xie, Z., Lam, J. W., Cheng, L., Chen, H., Qiu, C., ... & Tang, B. Z. (2001). Aggregation-induced emission of 1-methyl-1, 2, 3, 4, 5-pentaphenylsilole. *Chemical communications*, (18), 1740-1741.

[138] Guo, J., Fan, J., Lin, L., Zeng, J., Liu, H., Wang, C., Zhao, Z., & Tang, B. Z. (2018). Mechanical Insights into Aggregation-Induced Delayed Fluorescence Materials with Anti-Kasha Behavior. *Advanced Science*, *6*(3), 1801629. https://doi.org/10.1002/advs.201801629

[139] Zeng, Q., Li, Z., Li, Z., Dong, Y., Di, C., Qin, A., Hong, Y., Ji, L., Zhu, Z., Jim, C. K. W., Yu, G., Li, Q., Li, Z., Li, Z., Liu, Y., Qin, J., & Tang, B. Z. (2006). Fluorescence enhancements of benzene-cored luminophors by restricted intramolecular rotations: AIE and AIEE effects. *Chemical Communications*, *1*, 70–72. https://doi.org/10.1039/b613522f

[140] Mei, J., Leung, N. L. C., Kwok, R. T. K., Lam, J. W. Y., & Tang, B. Z. (2015). Aggregation-Induced emission: Together we shine, united we soar! *Chemical Reviews*, *115*(21), 11718–11940. https://doi.org/10.1021/acs.chemrev.5b00263

[141] Kim, J. H., An, B., Yoon, S., Park, S. K., Park, S. K., Kwon, J. E., Lim, C., Park, S. Y., & Park, S. Y. (2014). Highly Fluorescent and Color-Tunable Exciplex Emission from Poly(N-vinylcarbazole) Film Containing Nanostructured Supramolecular Acceptors. *Advanced Functional Materials*, *24*(19), 2746–2753. https://doi.org/10.1002/adfm.201302924

[142] Zhang, M., Guo, X., Zhang, S., & Hou, J. (2013). Synergistic effect of fluorination on molecular energy level modulation in highly efficient photovoltaic polymers. Advanced Materials, 26(7), 1118–1123. https://doi.org/10.1002/adma.201304427
[143] Hong, Y., Lam, J. W. Y., & Tang, B. Z. (2011). Aggregation-induced emission. *Chemical Society Reviews*, *40*(11), 5361. https://doi.org/10.1039/c1cs15113d

[144] Spano, F. C. (2009). The spectral signatures of Frenkel polarons in H- and J-Aggregates. *Accounts of Chemical Research*, *43*(3), 429–439. https://doi.org/10.1021/ar900233v

[145] Zhang, H., Nie, Y., Miao, J., Zhang, D., Li, Y., Liu, G., Sun, G., & Jiang, X. (2019). Fluorination of the tetraphenylethene core: synthesis, aggregation-induced emission, reversible mechanofluorochromism and thermofluorochromism of fluorinated tetraphenylethene derivatives. *Journal of Materials Chemistry C*, *7*(11), 3306–3314. https://doi.org/10.1039/c9tc00511k

[146] Zhao, W., He, Z., & Tang, B. Z. (2020). Room-temperature phosphorescence from organic aggregates. *Nature Reviews Materials*, *5*(12), 869–885. https://doi.org/10.1038/s41578-020-0223-z

[147] Blancon, J., Tsai, H., Nie, W., Stoumpos, C. C., Pedesseau, L., Katan, C., Kepenekian, M., Soe, C. M. M., Appavoo, K., Sfeir, M. Y., Tretiak, S., Ajayan, P. M., Kanatzidis, M. G., Even, J., Crochet, J. J., & Mohite, A. D. (2017). Extremely efficient internal exciton dissociation through edge states in layered 2D perovskites. *Science*, *355*(6331), 1288–1292. https://doi.org/10.1126/science.aal4211

[148] Connor, B. A., Su, A. C., Slavney, A. H., Leppert, L., & Karunadasa, H. I. (2023). Understanding the evolution of double perovskite band structure upon dimensional reduction. *Chemical Science*, *14*(42), 11858–11871. https://doi.org/10.1039/d3sc03105e

[149] Silver, S., Yin, J., Li, H., Brédas, J., & Kahn, A. (2018). Characterization of the Valence and Conduction Band Levels of n = 1 2D Perovskites: A Combined Experimental and Theoretical Investigation. *Advanced Energy Materials*, *8*(16). https://doi.org/10.1002/aenm.201703468

[150] Pan, F., Li, J., Ma, X., Nie, Y., Liu, B., & Ye, H. (2022). Free and self-trapped exciton emission in perovskite CsPbBr3 microcrystals. *RSC Advances*, *12*(2), 1035–1042. https://doi.org/10.1039/d1ra08629d

[151] Gan, Z., Wen, X., Zhou, C., Chen, W., Zheng, F., Yang, S., Davis, J. A., Tapping, P. C., Kee, T. W., Zhang, H., & Jia, B. (2019). Transient energy reservoir in 2D perovskites. *Advanced Optical Materials*, *7*(22). https://doi.org/10.1002/adom.201900971

[152] Lin, Y. L., Blackburn, J. L., Beard, M. C., & Johnson, J. C. (2021). Interlayer Triplet-Sensitized luminescence in layered Two-Dimensional hybrid Metal-Halide perovskites. *ACS Energy Letters*, *6*(11), 4079–4096. https://doi.org/10.1021/acsenergylett.1c02011

[153] Sun, J., Wang, K., Ma, K., Park, J. Y., Lin, Z., Savoie, B. M., & Dou, L. (2023). Emerging Two-Dimensional Organic Semiconductor-Incorporated Perovskites─A fascinating family of hybrid electronic materials. *Journal of the American Chemical Society*, *145*(38), 20694–20715. https://doi.org/10.1021/jacs.3c02143

[154] Beisenbayev, A. R., Ivanov-Prianichnikov, I., Peshkov, A., Adil, T., Hayrapetyan, D., & Lim, C.-K. (2025). Triple-Band Warm White-Light Emission from Type II Band-Aligned Aggregation-Induced Enhanced Emission Organic Cation-Incorporated Two-Dimensional Lead Iodide Perovskite. *International Journal of Molecular Sciences*, *26*(11), 5054. https://doi.org/10.3390/ijms26115054